TWO PROBLEMS IN COMPUTATIONAL WAVE DYNAMICS: KLEMP-WILHELMSON SPLITTING AT LARGE SCALES AND WAVE-WAVE INSTABILITIES IN ROTATING MOUNTAIN WAVES

A Dissertation

by

KEVIN CARL VINER

Submitted to the Office of Graduate Studies of
Texas A&M University
in partial fulfillment of the requirements for the degree of

DOCTOR OF PHILOSOPHY

December 2009

Major Subject: Atmospheric Sciences

TWO PROBLEMS IN COMPUTATIONAL WAVE DYNAMICS: KLEMP-WILHELMSON SPLITTING AT LARGE SCALES AND WAVE-WAVE INSTABILITIES IN ROTATING MOUNTAIN WAVES

A Dissertation

by

KEVIN CARL VINER

Submitted to the Office of Graduate Studies of
Texas A&M University
in partial fulfillment of the requirements for the degree of

DOCTOR OF PHILOSOPHY

Approved by:

Chair of Committee,	Craig C. Epifanio
Committee Members,	Ping Chang
	John Nielsen-Gammon
	R. Lee Panetta
	Fuqing Zhang
Head of Department,	Kenneth Bowman

December 2009

Major Subject: Atmospheric Sciences

ABSTRACT

Two Problems in Computational Wave Dynamics: Klemp-Wilhelmson Splitting at Large Scales and Wave-Wave Instabilities in Rotating Mountain Waves. (December 2009)

Kevin Carl Viner, B.S., Purdue University;

M.S., Purdue University

Chair of Advisory Committee: Dr. Craig C. Epifanio

Two problems in computational wave dynamics are considered: (i) the use of Klemp-Wilhelmson time splitting at large scales and (ii) analysis of wave-wave instabilities in nonhydrostatic and rotating mountain waves.

The use of Klemp-Wilhelmson (KW) time splitting for large-scale and global modeling is assessed through a series of von Neumann accuracy and stability analyses. Two variations of the KW splitting are evaluated in particular: the original acoustic-mode splitting of Klemp and Wilhelmson (KW78) and a modified splitting due to Skamarock and Klemp (SK92) in which the buoyancy and vertical stratification terms are treated as fast-mode terms. The large-scale cases of interest are the problem of Rossby wave propagation on a resting background state and the classic baroclinic Eady problem. The results show that the original KW78 splitting is surprisingly inaccurate when applied to large-scale wave modes. The source of this inaccuracy is traced to the splitting of the hydrostatic balance terms between the small and large time steps. The errors in the KW78 splitting are shown to be largely absent from the SK92 scheme.

Resonant wave-wave instability in rotating mountain waves is examined using a linear stability analysis based on steady-state solutions for flow over an isolated ridge. The analysis is performed over a parameter space spanned by the mountain

height (Nh/U) and the Rossby number (U/fL). Steady solutions are found using a newly developed solver based on a nonlinear Newton iteration. Results from the steady solver show that the critical heights for wave overturning are smallest for the hydrostatic case and generally increase in the rotating wave regime. Results of the stability analyses show that the wave-wave instability exists at mountain heights even below the critical overturning values. The most unstable cases are found in the nonrotating regime while the range of unstable mountain heights between initial onset and critical overturning is largest for intermediate Rossby number.

TABLE OF CONTENTS

CHAPTER Page

CHAPTER Page

LIST OF TABLES

LIST OF FIGURES

FIGURE Page

FIGURE Page

FIGURE Page

FIGURE Page

FIGURE Page

CHAPTER I

INTRODUCTION

A. Introduction

Significant improvements have been made in numerical weather prediction (NWP) due to technological and computing advances over the past few decades. In fact, 72-h forecasts today are as accurate as 36-h forecasts were 10-20 years ago [1, sec. 1.1]. However, while significant progress has been made in the prediction of synoptic-scale flows, the predictions of many other types of weather phenomena remains quite challenging. This is particularly true for problems at the mesoscale, and for problems in which mesoscale and synoptic-scale phenomena interact.

The present study addresses two problems related to challenges in mesoscale and meso-synoptic scale modeling and prediction. The first is a numerics study exploring the accuracy of time-split mesoscale NWP models when applied to problems at larger spatial scales. The second explores the presence of wave-wave instabilities in flows past terrain, which potentially has implications for the prediction of mountain-wave breaking.

B. Overview of time-splitting study

A common challenge in numerical modeling is accounting for the wide range of frequencies present in the atmosphere. For day-to-day weather prediction, the slow baroclinic and Rossby modes are generally the most important. However, model efficiency is often severely limited by the faster acoustic and gravity modes, which require

---

The journal model is *IEEE Transactions on Automatic Control*.

much smaller time steps to maintain stability. A common approach to this problem is to use time-splitting methods, in which the terms associated with the faster modes are integrated on a separate small time step for stability, while the terms associated with the slower modes use a larger step for efficiency (see, e.g., [2, 3, 4, 5]).

The time-splitting methods used in most mesoscale NWP models were originally developed in the context of small-scale cloud modeling. However, in recent years these methods (and models) have been applied to an ever increasing range of scales, including continental- and global-scale applications (see [6, 7, 8]). This broadening of scales has led to applications well beyond the original intent of the schemes.

One of the objectives of the present study is to formally analyze the performance of two common mesoscale time-split schemes as applied in the large-scale modeling context. The analysis is carried out using a von Neumann accuracy and stability approach as applied to two classical large-scale wave problems: the Rossby and Eady mode problems. The sources of any errors or numerical instabilities are examined, and some common numerical remedies are tested.

C. Overview of resonant-instability study

Flow over topography in a stably stratified atmosphere can lead to the formation of internal gravity waves. Under certain circumstances these waves can amplify and break, leading to phenomena such as downslope windstorms and clear air turbulence. The amplification and breaking of mountain waves is often explained using steady-state theory, particularly the nonlinear analysis of Long [9]. In steady-state analysis, the progression to wave breaking is governed by the nondimensional mountain height Nh/U, where N is the static stability, U is the cross mountain flow speed, and h is the mountain height. Larger Nh/U leads to larger amplitude waves and steeper

isentropes, and a sufficiently large Nh/U causes the isentropes to overturn so that convective instability occurs, leading to breaking of the wave.

Recent work has suggested a new pathway to topographic wave breaking not captured by the traditional steady-state model described above. In this new pathway the breaking is caused not by the standard nonlinear steepening, but rather by instability associated with resonant wave-wave interactions. The idea of resonant wave-wave instability has been introduced in a number of fields (see, [10, 11, 12]), but was first introduced in terms of mountain waves by Lee et. al. [13]. It was found that nonlinear interactions between disturbance gravity wave modes and a steady background mountain-wave could lead to a resonantly unstable wave mode. The growth of this instability was found at much smaller Nh/U than the traditional wave steepening, thus potentially leading to wave breaking at smaller mountain heights than previously considered.

The analysis of [13] was limited to a narrow range of parameters: specifically, nonrotating flow over a double-peak terrain profile. The objective of the work presented here is to extend the analysis to the rotating wave regime, using flow over a single peak as a test case. A Newton solver is developed to extend Long's steady-state solution to the rotating wave regime, and the steady critical overturning heights and surface drag values are mapped throughout the parameter space. A linear stability analysis is then performed about the steady solutions, with the instability threshold and growth rate values mapped throughout the parameter space.

D. Dissertation outline

The following chapter presents the analysis of the performance of time-split schemes with regards to large-scale prediction. The results presented therein are taken from

an article published in *Mon. Wea. Rev.* [14, hereinafter VE08]. Chapter III provides background material for the resonant instability study. Chapter IV details the development and testing of the steady-state Newton solver necessary for computing the steady-state background flows. The methods and results presented therein are expected to be submitted to *Quart. J. Roy. Meteor. Soc.* in the coming weeks. The instability of the steady solutions is considered in Chapter V. The final chapter provides a summary and discussion.

CHAPTER II

AN ANALYSIS OF KLEMP-WILHELMSON SCHEMES AS APPLIED TO LARGE-SCALE WAVE MODES

A. Introduction

Atmospheric motions feature a broad range of frequencies, with the lowest frequency modes often being the most important for prediction. Unfortunately, the largest time step allowed by an explicit integration scheme is ultimately limited by the highest frequencies, thereby making the explicit integration of the system very computationally expensive. A common method for relaxing this computational burden is to use split-explicit (or time-split) schemes. The basic idea behind these schemes is to use two time steps: the terms associated with fast motions are integrated on a small time step, while the remaining terms are integrated on a longer time step to increase efficiency.

The most common time-splitting approach used in mesoscale modeling is the partial-splitting method, first introduced by [2, hereinafter KW78] and later updated by [3, hereinafter SK92]. This Klemp-Wilhelmson (KW) method differs from a conventional additive-splitting approach [4, 5, e.g.] in that the fast and slow mode operators are never completely split [15, see sec. 7.3.2 for discussion]. Instead the fast and slow mode terms are integrated simultaneously, with the slow terms updated less frequently than the fast terms. This KW method and its extensions are used in a wide range of mesoscale research and forecasting models, including the widely used Weather Research and Forecasting Model (WRF) and the Pennsylvania State University / National Center for Atmospheric Research Mesoscale Model (MM5) (among many others).

The KW approach was originally developed in the context of mesoscale cloud modeling—specifically, for horizontal grid spacings on the order of 1 km or so and with typical time steps on the order of 10 s or less. However, in recent years the method has increasingly been used for the simulation of large-scale flows as well. Global and planetary atmosphere (particularly Mars-based) versions of the KW models now exist [see, e.g., [6] for the global MM5; a global WRF model is under development] and the method is now routinely also used for regional climate simulation (e.g., [7]; [8]). The grid spacings and time steps for these simulations are often much larger than those used at the mesoscale, with typical grid spacings on the order of 100 km and with time steps on the order of 100 s or more.

1. Historical context: the KW78 and SK92 splittings

The first consideration in any splitting algorithm is to define an operator splitting—that is, to identify terms associated with the fast modes and to split the full equations into the resulting small-step and large-step parts. In cloud modeling the fast motions are typically acoustic waves and the slower modes of interest are primarily gravity-driven. The operator splitting proposed by KW78 thus treated only the acoustic modes—specifically the pressure gradient and divergence terms—as part of the small step cycle. This original KW78 splitting was adopted by a number of mesoscale community models, some of which are still widely used. Examples of widely used KW78 models include the MM5 [16] and global MM5 [6] and the Colorado State University RAMS model [17].

A potential disadvantage of the KW78 splitting is that the scheme becomes unstable to fast gravity wave motions once the large time step becomes sufficiently large (at least in principle—but see comments below). To avoid this problem, SK92 proposed an alternative operator splitting in which the buoyancy and vertical strati-

fication terms are treated as fast-mode terms in addition to the pressure gradient and divergence. This modified splitting integrates gravity waves on the small time step, thus stabilizing the scheme for larger Δt. The computational cost of this enhanced stability turns out to be modest, and most recently developed KW models have thus used the SK92 splitting in place of the KW78 scheme. Some examples of SK92 models include the WRF model [18], the University of Oklahoma ARPS model [19], and the Navy COAMPS model (J. D. Doyle, 2007, personal communication) (among several others).

As already mentioned, the original motivation for the SK92 splitting was the nominal instability of the KW78 scheme at large scales—specifically, for time steps exceeding $N\Delta t = 1$ (where N is the Brunt-Väisälä frequency and Δt is the large time step). However, in practical applications this KW78 stability cutoff has rarely proved to be a limitation. The reason is that the $N\Delta t > 1$ cutoff occurs only in the most nonhydrostatic modes, and at large horizontal grid spacings—specifically, for grid spacings on the order of the domain depth or larger—these modes are generally not present. Indeed, a brief survey of the literature shows that the KW78 community models are routinely run on synoptic-scale grids, and that the large time steps on these grids routinely exceed the nonhydrostatic stability cutoff (often by factors of three or more).

2. Study overview

The purpose of the present study is to provide a formal analysis of the KW78 and SK92 splitting methods as applied in the large-scale modeling context. Three different versions of the splittings are addressed in particular: the original KW78 leapfrog splitting proposed by [2], the SK92 version of the leapfrog splitting (SK92-LF) suggested by [3], and the newer SK92 third-order Runge-Kutta scheme (SK92-RK) presented by

[20]. For each scheme a set of von Neumann accuracy and stability analyses is carried out for the problem of large-scale Rossby-wave propagation on a resting background state.

A brief outline of the study is as follows. The following section introduces a simplified, constant-coefficient form of the Rossby-wave problem and describes the von Neumann methodology as applied for the two leapfrog schemes (i.e., KW78 and SK92-LF). The results for the two leapfrog schemes are given in section C. The original KW78 method is shown to produce significant Rossby-mode phase-speed errors, whereas the SK92-LF splitting is essentially error-free. The source of the KW78 errors is explored further in section D. Ultimately the errors are traced to the compressible vertical adjustment—or more precisely, to the failure of the scheme to maintain the hydrostatic balance. Section E presents the SK92-RK analysis and compares the RK and LF schemes at varying small and large time steps. The final section gives a summary of results.

A similar (but somewhat more involved) analysis has also been developed for the Eady baroclinic wave problem. However, the Eady results largely echo those of the Rossby problem, and thus only the Rossby case will be discussed in detail.

B. The Rossby problem: Basic formulation

The present section develops the Rossby problem formulation and discusses the discretizations used for the two leapfrog splittings (KW78 and SK92-LF). Results for the leapfrog splittings are given in the following section.

1. Theoretical problem setup

As a starting point, consider a two-dimensional (2D) compressible-Boussinesq system on an f-plane (the β-effect is added below) as linearized about a resting background state; specifically

$$u_t + P_x = f_0 v \tag{2.1}$$

$$v_t = -f_0 u \tag{2.2}$$

$$w_t + P_z = b \tag{2.3}$$

$$b_t = -N^2 w \tag{2.4}$$

$$P_t + c_s^2 \left(u_x + w_z\right) = 0 \tag{2.5}$$

where (2.1)-(2.5) are the horizontal and vertical momentum equations, the thermodynamic equation, and the pressure equation, respectively; u, v, and w are the horizontal and vertical velocity components in Cartesian coordinates, P is the Boussinesq disturbance pressure, b is the buoyancy, f_0 is the Coriolis parameter, c_s is the speed of sound, and N is the Brunt-Väisälä frequency. Subscripts denote partial derivatives with respect to the given coordinate. The parameters $f_0,\ c_s$, and N are all taken to be constants.

As is well known, the propagation of Rossby waves on a resting background state depends on the meridional variation of the Coriolis parameter. This meridional dependence renders the Rossby wave a non-constant-coefficient problem, which in turn complicates the analysis. Fortunately, however, an equivalent constant-coefficient system can be formulated by simply adding the appropriate driving term to the 2D problem (2.1)-(2.5). The details are given in appendix H, but the end result is that

(2.2) is replaced by the modified form

$$v_t = -\int_{-\infty}^{x} \beta v \, dx' - f_0 u \tag{2.6}$$

where β is the meridional gradient of f and where it is implicitly assumed that $v \to 0$ as $x \to -\infty$.

The system consisting of (2.1), (2.6), and (2.3)-(2.5) supports three wave types: high-frequency acoustic modes, intermediate-frequency gravity modes, and low-frequency Rossby modes. In the appropriate limits, the dispersion relation for the system reduces to the standard dispersion relation for each of the three wave types (see appendix A). This existence of realistic fast and slow modes makes the modified system useful for testing multi-timescale numerics.

Substituting a Fourier mode of the form

$$\boldsymbol{\psi} = \hat{\boldsymbol{\psi}}(t) \exp\left[i(kx + mz)\right] \tag{2.7}$$

where $\hat{\boldsymbol{\psi}} = \left(\hat{u}, \hat{v}, \hat{w}, \hat{b}, \hat{P}\right)^T$ is the Fourier amplitude leaves

$$\hat{u}_t + ik\hat{P} = f_0\hat{v} \tag{2.8}$$

$$\hat{v}_t = i\frac{\beta}{k}\hat{v} - f_0\hat{u} \tag{2.9}$$

$$\hat{w}_t + im\hat{P} = \hat{b} \tag{2.10}$$

$$\hat{b}_t = -N^2\hat{w} \tag{2.11}$$

$$\hat{P}_t + c_s^2\left(ik\hat{u} + im\hat{w}\right) = 0 \tag{2.12}$$

In order to simplify the notation, the carat ($\hat{}$) over the Fourier variables will be dropped for the remainder of the chapter.

2. Analytic solution

Leaving only the time derivatives on the left hand side, (2.8)-(2.12) can be written in matrix form as

$$\frac{d\boldsymbol{\psi}(t)}{dt} = \mathbf{M}\boldsymbol{\psi}(t) \tag{2.13}$$

where $\mathbf{M}$ is a 5×5 matrix of constant coefficients. Standard methods then show that the frequencies of all modes supported by the system are determined completely by the eigenvalues of $\mathbf{M}$. In the present study these eigenvalues are computed numerically. The Rossby mode is then identified by finding the solution with frequency most closely matching the corresponding quasi-geostrophic (QG) frequency, (2.60). In all cases this Rossby solution is also the slowest of the five modes supported by (2.13).

3. Discretized solution: KW78 splitting

In the original KW78 splitting the terms integrated on the small time step are those included on the left-hand side (LHS) of (2.8)-(2.12), while those integrated on the large step are included on the right-hand side (RHS). Here the slow mode terms include the Coriolis, buoyancy, vertical stratification, and Rossby driving terms. In the following it is assumed that the large time step Δt is a factor of ns larger than the small step $\Delta\tau$; that is, $\Delta\tau = \Delta t/ns$, where ns is an integer.

The KW78 scheme uses leapfrog (LF) time differencing for the large-time-step forcings and forward-backward (FB) differencing for the small step. In practice this means that the large-time-step forcings are held fixed at time level t while the remaining terms are integrated from $t - \Delta t$ to $t + \Delta t$ using $2ns$ FB small steps. The vertical pressure gradient and vertical divergence terms are computed trapezoidally so as to improve the stability of the scheme at small grid aspect ratios. Letting the

time on the large and small time steps be denoted by t and τ, respectively, the fully discretized versions of (2.8)-(2.12) are given by

$$u^{\tau+\Delta\tau} = u^{\tau} + \Delta\tau(-ikP^{\tau+\Delta\tau} + F_u^t) \tag{2.14}$$

$$v^{\tau+\Delta\tau} = v^{\tau} + \Delta\tau F_v^t \tag{2.15}$$

$$w^{\tau+\Delta\tau} = w^{\tau} + \Delta\tau(-im\overline{P}^{\tau} + F_w^t) \tag{2.16}$$

$$b^{\tau+\Delta\tau} = b^{\tau} + \Delta\tau F_b^t \tag{2.17}$$

$$P^{\tau+\Delta\tau} = P^{\tau} + \Delta\tau(-ic_s^2 k u^{\tau} - ic_s^2 m\overline{w}^{\tau} + F_P^t) \tag{2.18}$$

where the time averaging operator is defined by

$$\overline{q}^{\tau} = \frac{q^{\tau} + q^{\tau+\Delta\tau}}{2} \tag{2.19}$$

and where the F_q^t terms represent the fixed large-step forcings. The solution is advanced from $t - \Delta t$ to $t + \Delta t$ by applying (2.14)-(2.18) $2ns$ times.

Note that (2.14)–(2.18) are not yet prognostic as they include terms that involve implicit time differencing. However, these implicit terms are easily resolved through straightforward algebraic manipulation. The details are given in appendix I, but the end result is that (2.14)–(2.18) corresponds to the equivalent explicit system

$$\boldsymbol{\xi}^{\tau+\Delta\tau} = \mathbf{S}\,\boldsymbol{\xi}^{\tau} + \mathbf{L}\,\boldsymbol{\xi}^{t} \tag{2.20}$$

where $\boldsymbol{\xi}^t = (u^t, v^t, w^t, b^t, P^t)^T$ is the discretized approximation to $\boldsymbol{\psi}$ at time t and where $\mathbf{S}$ and $\mathbf{L}$ include the terms on the small and large time steps, respectively.

The solutions to (2.20) are obtained by first defining a two-level solution vector

$$\boldsymbol{\phi}^t = \begin{pmatrix} \boldsymbol{\xi}^{t-\Delta t} \\ \boldsymbol{\xi}^{t} \end{pmatrix} \tag{2.21}$$

with the understanding that the upper half of $\boldsymbol{\phi}$ will be advanced forward on the small time step while the lower half remains fixed at the middle time level. Following [15, sec. 7.3.2,see also SK92], the full small-time-step cycle—advancing from time $t - \Delta t$ to $t + \Delta t$—can then be written in matrix form as

$$\boldsymbol{\phi}^{t+\Delta t} = \mathbf{R}\mathbf{A}^{2ns}\boldsymbol{\phi}^{t} \tag{2.22}$$

where

$$\mathbf{A} = \begin{pmatrix} \mathbf{S} & \mathbf{L} \\ \mathbf{0} & \mathbf{I} \end{pmatrix} \tag{2.23}$$

is a 10×10 matrix that advances the solution forward a single small step, while

$$\mathbf{R} = \begin{pmatrix} \mathbf{0} & \mathbf{I} \\ \mathbf{I} & \mathbf{0} \end{pmatrix} \tag{2.24}$$

is a reordering matrix. The matrix $\mathbf{I}$ in (2.23) and (2.24) is the 5×5 identity operator. According to (2.20), a single application of $\mathbf{A}$ in (2.22) advances the upper half of $\boldsymbol{\phi}$ forward a single small time step while leaving the lower half unchanged. The $\mathbf{R}$ operator then reorders the variables at the end of the small-step cycle in preparation for the next series of small steps.

As with the continuous problem, the frequencies of the wave modes in (2.22) are determined completely by the eigenvalues of $\mathbf{R}\mathbf{A}^{2ns}$. Specifically, given a discretized eigenvalue of the form $\lambda = \exp(-i\omega\Delta t)$, the associated complex frequency is then $\omega = \omega_r + i\omega_i = i\ln(\lambda)/\Delta t$ (using the standard branch for ln). The discretized Rossby mode is then selected as the mode with the complex frequency that most closely matches the analytic frequency described in section B2. As shown in section C2, this discretized frequency approaches the analytic frequency in the small Δt limit, thus confirming that the mode selected is in fact the Rossby mode.

4. Discretized solution: SK92-LF splitting

The SK92-LF splitting differs from the KW78 splitting in that the buoyancy and vertical stratification terms are updated on the small step. To be specific, the vertical velocity and buoyancy equations (2.16) and (2.17) are replaced by

$$w^{\tau+\Delta\tau} = w^{\tau} + \Delta\tau(-im\overline{P}^{\tau} + \overline{b}^{\tau} + F_w^t) \tag{2.25}$$

$$b^{\tau+\Delta\tau} = b^{\tau} + \Delta\tau(-N^2\overline{w}^{\tau} + F_b^t) \tag{2.26}$$

where in the present case $F_w^t = F_b^t = 0$. As before, the implicit dependence is resolved through straightforward algebraic manipulation. Given the modified **S** and **L** operators, the solution then follows as in section B3.

5. An unsplit scheme

The following sections also make reference to an unsplit scheme. The specific scheme considered is

$$u^{t+\Delta t} = u^{t-\Delta t} + 2\Delta t(-ikP^{t+\Delta t} + F_u^t) \tag{2.27}$$

$$v^{t+\Delta t} = v^{t-\Delta t} + 2\Delta t F_v^t \tag{2.28}$$

$$w^{t+\Delta t} = w^{t-\Delta t} + 2\Delta t(-im\overline{P}^{t} + \overline{b}^{t}) \tag{2.29}$$

$$b^{t+\Delta t} = b^{t-\Delta t} + 2\Delta t(-N^2\overline{w}^{t}) \tag{2.30}$$

$$P^{t+\Delta t} = P^{t-\Delta t} + 2\Delta t(-ic_s^2 k u^{t-\Delta t} - ic_s^2 m\overline{w}^{t}) \tag{2.31}$$

where

$$\overline{q}^{t} = \frac{q^{t-\Delta t} + q^{t+\Delta t}}{2}$$

and where F_u^t and F_v^t are as described previously. Note that (2.27)–(2.31) is exactly the SK92-LF method with $ns = 1/2$ (so that $\Delta\tau = 2\Delta t$). Comparing the split

and unsplit schemes for the same Δt then measures the error introduced by simply splitting off a small-step cycle.

C. The Rossby problem: Results

For the Rossby problem, the discretization error is measured in terms of the fractional error in ω_r—that is

$$\varepsilon_p = \frac{\omega_{rd} - \omega_{ra}}{\omega_{ra}} \tag{2.32}$$

where the subscripts d and a refer to *discretized* and *analytic*, respectively. Since the phase speed of the mode is given by $c = \omega_r/k$, (2.32) is equivalent to the fractional phase-speed error.

1. Parameter ranges

Table I. Parameter values for the Rossby problem.

parameter	$c_s(ms^{-1})$	$f_0(s^{-1})$	$\beta(ms)^{-1}$	$N(s^{-1})$	$\lambda_x(km)$	$\lambda_z(km)$
reference value	330	10^{-4}	1.65×10^{-11}	.01	4800	20
range	–	–	–	.001-.02	2000-12500	12-150

The eigenvalues of the analytic coefficient matrix $\mathbf{M}$ in (2.13) are determined completely by five parameters, all with units of frequency [1]: N, f_0, β/k, $c_s k$ and $c_s m$. The full parameter space for ε_p then consists of these five physical parameters plus $\Delta\tau$ and ns. In the following, this parameter space will be explored in two ways. First, 2D cross sections are mapped by varying two of the five physical parameters while keeping the other three physical parameters and the two time steps held fixed.

[1] To see this, substitute the modified buoyancy $\theta = b/N$ and modified pressure $p = P/c_s$ into (2.8)–(2.12) (as done, for example, by SK92). The resulting system then depends only on the five parameters listed.

(There is one exception to this, in that β is actually held fixed rather than β/k.) The second set of computations involves keeping all five physical parameters and ns held fixed while varying only $\Delta\tau$. Three values of ns are considered: $ns = 1$, 2, and 3.

The phase-speed error (2.32) was found to be most sensitive to changes in N, $c_s k$ and $c_s m$. The 2D cross-section results are thus shown only for these three parameters. The ranges shown in the cross sections are as given in the final row of Table I, with $\lambda_x = 2\pi/k$ and $\lambda_z = 2\pi/m$ being the horizontal and vertical wavelengths, respectively (with c_s held fixed). Parameters not varied in a given cross section are fixed at reference values, as shown in the middle row of Table I.

The time step for the cross-sections using the KW78 scheme is set at $\Delta\tau =$ 100 s, which is characteristic of the outer-grid time steps used in most regional-scale modeling. This is also similar to the time step used by [6] in their global MM5 calculations. By contrast, the cross sections computed with the SK92 splitting are all set at $\Delta\tau = 500$ s, which for typical ns (say ns between 2 and 6) implies a large time step similar to those used in general circulation models. But as will be seen, the $\Delta\tau$ dependence for the SK92 scheme is effectively quadratic. The results for $\Delta\tau = 100$ s can thus be inferred easily from the $\Delta\tau = 500$ s results (so as to allow comparison with the KW78 case). Note that even for $\Delta\tau = 500$ s the Rossby mode is very well resolved in time ($|\omega_{ra}\Delta\tau| \simeq 1 \times 10^{-3}$).

2. KW78 results

Figure 1 shows the phase-speed error (2.32) for the Rossby mode as computed using the KW78 splitting with $\Delta\tau = 100$ s. Column 1 of the figure shows the error as a function of $c_s k\Delta\tau$ and $c_s m\Delta\tau$, with column 2 showing the $N\Delta\tau$ and $c_s m\Delta\tau$ dependence. Column 3 shows the spectral radius of the discretized amplification matrix $\mathbf{RA}^{2ns}$ defined by (2.22). The first row of the figure shows the $ns = 2$ case, with row

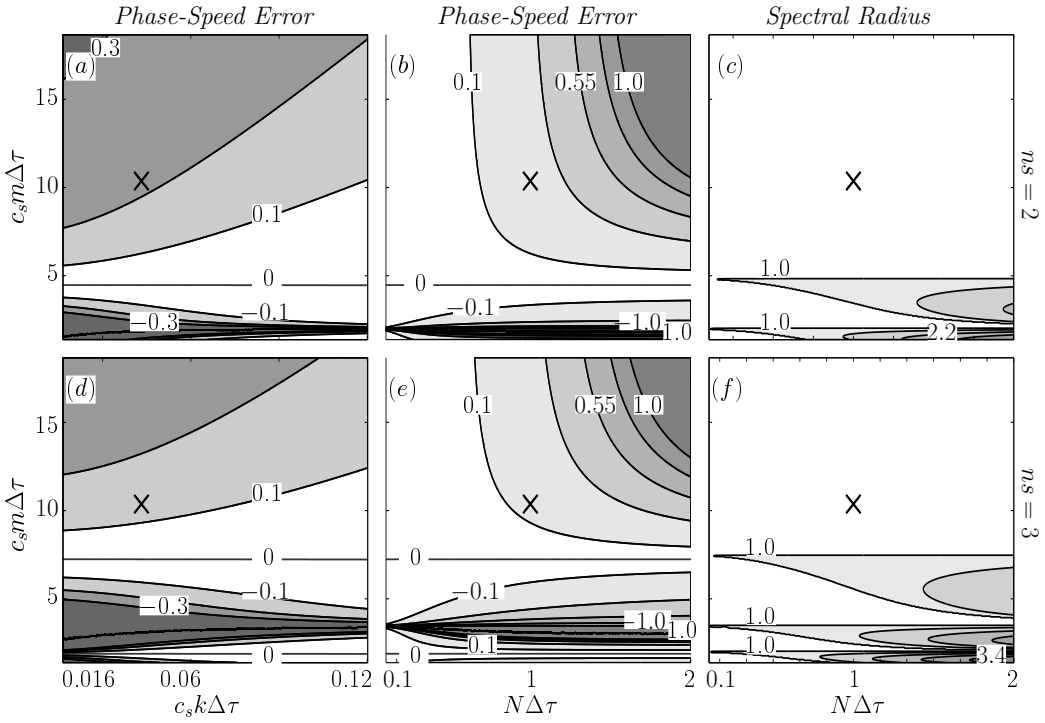

Fig. 1. Fractional phase-speed error and spectral radius for KW78 time differencing as applied to the Rossby problem with $\Delta\tau = 100$ s. (a), (d) phase-speed error as a function of $c_s k\Delta\tau$ and $c_s m\Delta\tau$ [contour interval ($c.i.$)= 0.1] for ns = (a) 2 and (d) 3. (b), (e) phase-speed error as a function of $N\Delta\tau$ and $c_s m\Delta\tau$ [$c.i.$ = 0.225; values greater than 1 suppressed] for ns = (b) 2 and (e) 3. (c), (f) spectral radius [$c.i.$ = 0.6; values greater than 1 shown] for ns = (c) 2 and (f) 3. All parameter ranges and fixed reference values are as shown in Table I. The reference values for N, λ_x, and λ_z are marked by a cross in each panel.

2 showing the $ns = 3$ case. A cross in each panel shows the characteristic reference parameter values listed in Table I. Shading indicates phase-speed errors greater than 10% in columns 1 and 2 and spectral radii greater than 1 in column 3. Since the analytic solution is non-amplifying, a spectral radius exceeding 1 indicates numerical instability.

Figures 1a,b show that for $ns = 2$ the error throughout much of the relevant parameter space is greater than 10%. Figure 1a shows that the error is greatest for

small k and large m—that is, for small aspect ratios k/m. At fixed k and m the error increases as N increases (Fig. 1b), with the error exceeding 100% for large values of N and m. As ns is increased the error distribution at large m remains roughly unchanged, suggesting that the error in this case is determined primarily by $\Delta\tau$ and not Δt. However, at smaller m a set of complicated error bands appears. These latter error bands coincide with the numerical instability bands seen in column 3.

It should be noted that the instability bands in column 3 are due to the acoustic modes and not the Rossby mode. As shown in section F, this acoustic instability is similar to that found by SK92 for the acoustic-advection problem, except that here the instability reflects a coupling with buoyancy rather than with advection. As in SK92, the instability occurs only where the acoustic-mode frequency as sampled onto the large time step is either $\omega_{rd} = \pm\pi/2\Delta t$, $\pm\pi/\Delta t$ or zero—hence the banded structure. Further details can be found in the section F. The correspondence between this instability and the Rossby mode phase-speed error apparently reflects the acoustic nature of the Rossby mode small-step adjustment.

Figure 2 shows both ε_p and the spectral radius for the KW78 scheme considered as functions of $\Delta\tau$. The physical parameters for these calculations are fixed at the reference values shown in Table I. The error curve for $ns = 1$ (Fig. 2a) shows that the error vanishes at small $\Delta\tau$ but quickly becomes large as $\Delta\tau$ is increased, reaching 27% at $\Delta\tau = 100$ s. The steady increase in the error shifts to larger $\Delta\tau$ for $ns = 2$ and 3, but instability bands and associated error peaks appear at smaller $\Delta\tau$ (as in Fig. 1—see section F). In all three cases the error at $\Delta\tau = 100$ s is clearly unacceptable.

3. Filtering the KW78 scheme

The KW78 scheme is typically used with numerical filters to damp the acoustic modes. Some commonly used filters include the Robert-Asselin time filter [15, sec. 2.3.5], the

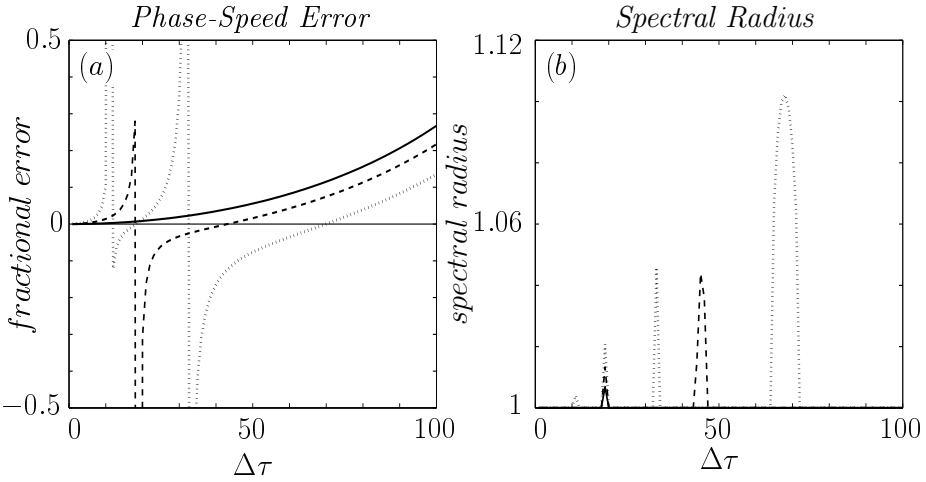

Fig. 2. (a) Fractional phase-speed error and (b) spectral radius as functions of $\Delta\tau$ for KW78 time differencing as applied to the Rossby problem. Lines show $ns = 1$ (solid), $ns = 2$ (dashed), and $ns = 3$ (dotted). Physical parameters are held fixed at the reference values indicated in Table I.

3D divergence damping of SK92, and the implicit biasing of [21]. Of the three, only implicit biasing was found to have a non-negligible impact on the KW78 Rossby results. Results for time filtering and divergence damping can be found in appendicies J and K, respectively.

With implicit biasing, the time-averaging operator (2.19) is replaced by the weighted time average

$$\overline{q}^{\tau} = \frac{(1-\epsilon)\, q^{\tau} + (1+\epsilon)\, q^{\tau+\Delta\tau}}{2} \tag{2.33}$$

where ϵ is the implicit biasing coefficient. Setting $\epsilon > 0$ acts to bias the vertical pressure gradient and divergence terms towards backward time differencing, thus damping and slowing the vertically propagating acoustic modes. As suggested by [21], setting $\epsilon = 0.2$ is effective at filtering the acoustic modes without noticeably affecting the gravity modes.

Figure 3 shows the KW78 Rossby phase-speed errors and spectral radius for the

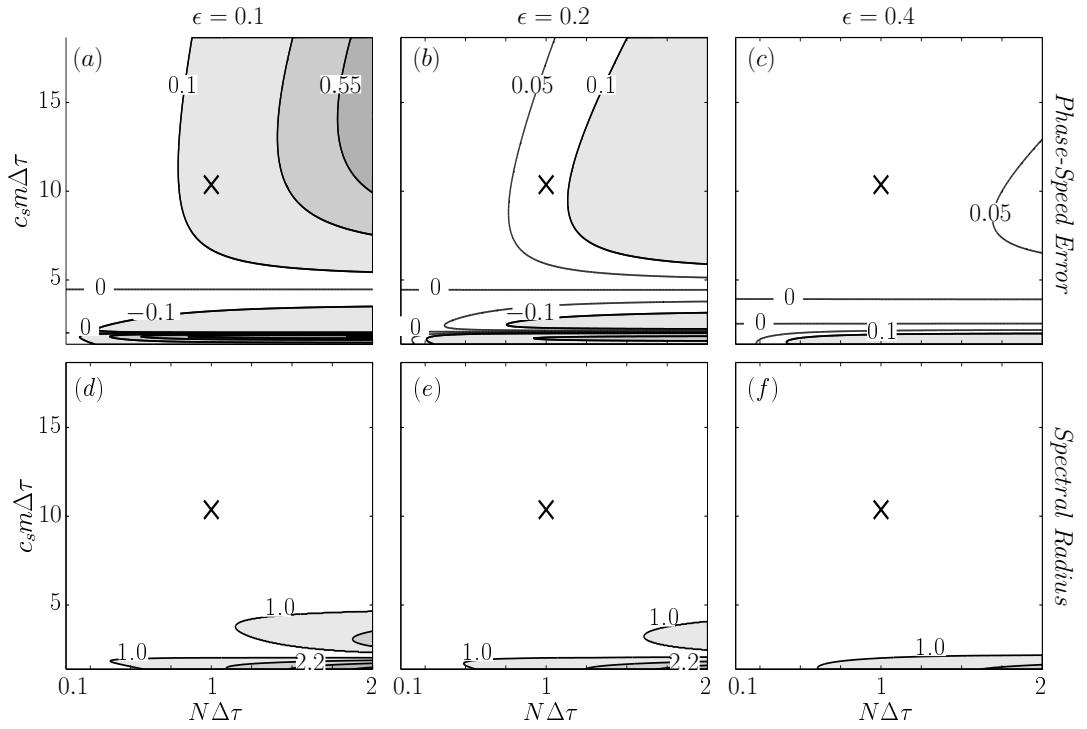

Fig. 3. Effect of implicit biasing on the KW78 Rossby results. Shown are the fractional phase-speed error and spectral radius for $ns = 2$ with $\Delta\tau = 100$ s. (a)-(c) phase-speed error [shaded $c.i. = 0.225$] for $\epsilon =$ (a) 0.1, (b) 0.2 and (c) 0.4. (d)-(f) show the corresponding spectral radii [$c.i. = 0.6$, values larger than 1 shown]. Parameter ranges and fixed reference values are as indicated in Table I.

case $ns = 2$ (cf. Figs 1b,c) with implicit biasing coefficients of $\epsilon = 0.1$, 0.2 and 0.4. Adding the implicit biasing significantly improves the accuracy and stability of the scheme. However, the errors are still significant—for $\epsilon = 0.1$ and 0.2 the errors still exceed 10% over much of the parameter space.

4. SK92-LF results

The phase-speed errors for the SK92 version of the leapfrog scheme are as shown in Figure 4. Figures 4a,b show the SK92-LF cross-section results for $\Delta\tau = 500$ s with $ns = 3$. Comparison to Figs. 1d,e shows that switching to the SK92 scheme has dramatically reduced the error, even for $\Delta\tau$ five times as large. (The contours in

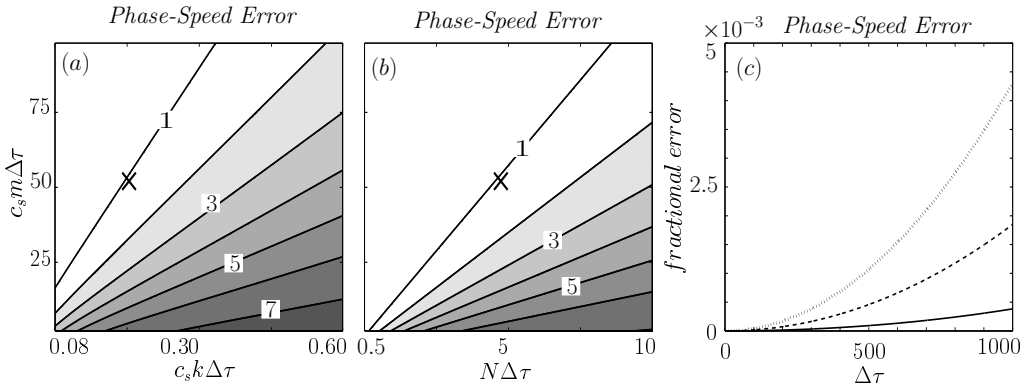

Fig. 4. Fractional phase-speed error for SK92-LF time differencing as applied to the Rossby problem. (a) phase-speed error as a function of $c_s k\Delta\tau$ and $c_s m\Delta\tau$ and (b) phase-speed error as a function of $N\Delta\tau$ and $c_s m\Delta\tau$, both for $ns = 3$ and $\Delta\tau = 500$ s [*c.i.* $= 1 \times 10^{-3}$; contour labels in units of 10^{-3}]. (c) error as a function of $\Delta\tau$ for $ns = 1$ (solid), 2 (dashed), and 3 (dotted) [vertical axis labels in units of 10^{-3}]. Parameter ranges and fixed reference values are as indicated in Table I.

Fig. 4 are in units of 10^{-3}, so that the largest error shown is just less than 1%. To get the errors for $\Delta\tau = 100$ s, divide by 25.)

The $\Delta\tau$ dependence for the SK92-LF splitting is shown in Fig. 4c (cf. Fig. 2a). Note that the upper limit for $\Delta\tau$ has been increased to $\Delta\tau = 1000$ s, so as to better show the error at large time steps. But even with this increased $\Delta\tau$ the largest error shown is still less than 0.5%. Consideration of the spectral radius shows that the instability bands have completely disappeared as well (not shown).

Inspection of the errors in Fig. 4c shows that the SK92-LF error behaves roughly quadratically, both in terms of increasing $\Delta\tau$ (at fixed ns) and increasing ns (at fixed $\Delta\tau$). However, comparing these errors to those of an equivalent unsplit scheme shows that to a large extent the errors stem from the splitting rather than from the individual small-step and large-step operators. As an example, the unsplit method (2.27)-(2.31) with $\Delta t = 3000$ s (analogous to the $ns = 3$ case with $\Delta\tau = 1000$ s)

produces an error of 0.0005%, which is almost 10^3 times smaller than the equivalent error in Fig. 4c. So while the errors in the SK92-LF method are generally small, the split scheme does in a relative sense produce more error than an analogous unsplit scheme.

D. Analysis of the KW78 errors

The size of the KW78 Rossby errors is somewhat surprising, given the widespread use of this method on synoptic-scale grids. The present section explores the source of these errors in greater detail.

1. A vertical adjustment problem

The KW78 error distributions in Fig. 1—specifically, the increasing errors at small k/m and large N—suggest that the source of the errors is most likely the compressible vertical adjustment—or stated differently, the adjustment to hydrostatic balance. To demonstrate this, consider a 1D vertical adjustment model with a slow oscillatory driving force added to the thermodynamic equation. Specifically

$$w_t + imP = b \tag{2.34}$$

$$b_t = -N^2 w - i\omega_b b \tag{2.35}$$

$$P_t + c_s^2 (imw) = 0 \tag{2.36}$$

where the ω_b term in (2.35) forces an oscillation with natural frequency ω_b [cf. (2.10)-(2.12)]. The dispersion relation for this system implies three modes: two fast acoustic modes and a driven mode produced by the ω_b term. It can be shown that for $\omega_b \ll c_s m$, the driven mode is effectively in hydrostatic balance.

The KW78 method as applied to the vertical adjustment problem is evaluated

below. The discretized and analytic solutions are again obtained as in section B, with the specific time discretization following (2.16)-(2.18) (with $k = 0$), except that the driving term in (2.35) is added to the large-time-step forcing in (2.17). The error is again measured using (2.32) but with the frequency of the slow driven mode used in place of the Rossby frequency. The natural frequency of the driven mode is held fixed at $\omega_b = 1$ day^{-1}. All other necessary parameter values are as in the Rossby problem, section C1.

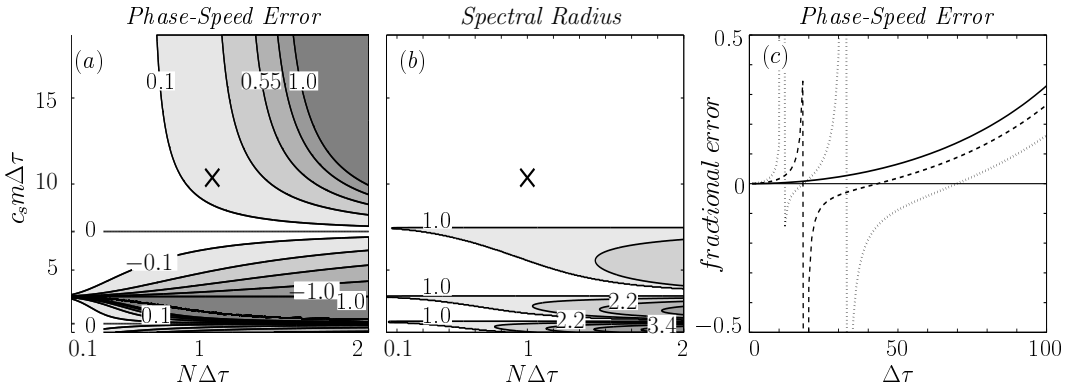

Fig. 5. Fractional phase-speed error and spectral radius for KW78 time discretization as applied to the vertical adjustment problem. (a) phase-speed error [$c.i. = 0.225$; values greater than 1 suppressed] and (b) spectral radius [$c.i. = 0.6$; values greater than 1 shown] as functions of $N\Delta\tau$ and $c_s m\Delta\tau$ for $ns = 3$ and $\Delta\tau = 100$ s. Ranges for N and λ_z are as listed in Table I, with $\omega_b = 1$ day^{-1}. The reference values in each panel are marked by a cross. (c) fractional phase-speed error as a function of $\Delta\tau$ for $ns = 1$ (solid), 2 (dashed), and 3 (dotted) with N and λ_z fixed at the reference values.

2. Results

Figures 5a,b show the slow-mode phase-speed error and the spectral radius of the KW78 amplification matrix as functions of $N\Delta\tau$ and $c_s m\Delta\tau$ for $ns = 3$ (recall that $k = 0$). The contours and shading in the figure are the same as in Figure 1.

Figure 5c shows the error as a function of $\Delta\tau$ for $ns = 1, 2$ and 3. Comparison to Figs. 1e,f and 2a shows that the current adjustment results are similar to those of the previous Rossby model. This similarity suggests that the errors and instability in the two problems stem from the same source—namely, from the vertical adjustment dynamics described by (2.34)–(2.36) and (2.10)–(2.12).

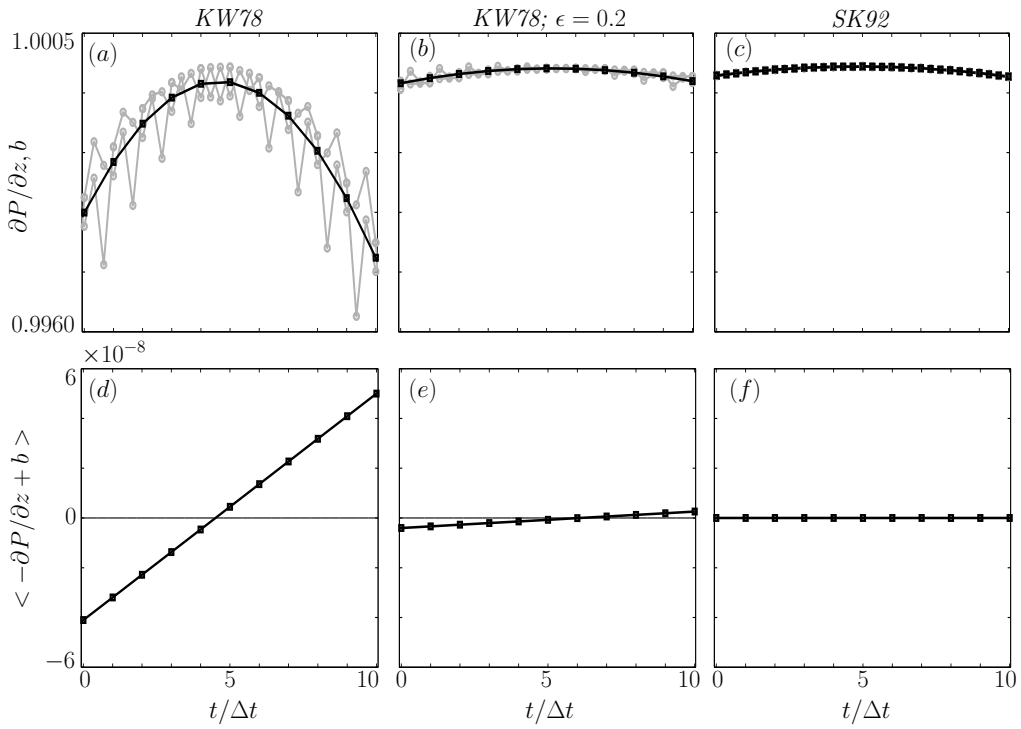

Fig. 6. Evolution of the hydrostatic balance in the vertical adjustment model. (a)–(c) vertical pressure gradient on the small step (gray) and buoyancy on either the large or small time step (black) as functions of time at fixed z [values normalized by the largest $\partial P/\partial z$ in each panel]. Shown are the (a) KW78, (b) KW78 with implicit biasing ($\epsilon = 0.2$), and (c) SK92-LF schemes. (d)-(f) $\langle -\partial P/\partial z + b \rangle$ [units of 10^{-8} m/s^2], where brackets indicate an average over the small-step cycle. Cases shown are as in (a)–(c). All results are for $N = 0.02$ s^{-1}, $\lambda_z = 15$ km, and $ns = 3$ with $\Delta\tau = 100$ s.

The evolution of the hydrostatic balance under the KW78 splitting is considered in Fig. 6. The results shown in the figure are for the $N = 0.02\ s^{-1}$ and $\lambda_z = 15\ km$

case with $ns = 3$, which has a phase-speed error of roughly 300% (cf. Fig. 5a). Figure 6a shows the vertical pressure gradient as computed on the small-step cycle, as well as the corresponding buoyancy term as computed on the large time step. (Note that the pressure gradient is shown with two curves, since the leapfrog small-step cycles overlap.) The sum of the pressure gradient and buoyancy as averaged over a small-step cycle is shown in Fig. 6d.

As seen in the figure, the splitting of the pressure gradient and buoyancy terms between the small and large time steps leads to significant acoustic noise[2] and a failure to maintain hydrostatic balance (Figs. 6a,d). The relative imbalance then in turn leads to an acceleration of the oscillation—first downward (increasing the buoyancy) and then upward (decreasing buoyancy). The balance can be restored to some extent through implicit biasing (as described in section C3), which damps the acoustic modes so that the buoyancy and pressure gradient remain more closely coupled (Figs. 6b,e). However, a much better representation of the balance comes from the SK92-LF scheme, in which the buoyancy and pressure gradient are no longer split (Figs. 6c,f). For reference, the error in the SK92-LF case is less than 0.0001%.

E. Third-order Runge-Kutta differencing

As shown by [22, 20], the KW splitting can also be stably applied to several forward-in-time schemes, particularly to some Runge-Kutta variants. Here the third-order Runge-Kutta (RK3) method of [20, hereinafter WS02] is evaluated as implemented using the SK92 operator splitting (SK92-RK). This SK92-RK method is the scheme currently used in the Advanced Research WRF model (WRF-ARW) [18].

---

[2]Note that the adjustment problem does not support gravity modes, since $k = 0$.

1. Discretized solution: SK92-RK splitting

The particular RK3 method used by WS02 can be defined (in unsplit scalar form) as

$$q^* = q^t + \frac{\Delta t}{3} F(q^t) \tag{2.37}$$

$$q^{**} = q^t + \frac{\Delta t}{2} F(q^*) \tag{2.38}$$

$$q^{t+\Delta t} = q^t + \Delta t\, F(q^{**}) \tag{2.39}$$

where F represents the righhand-side forcing terms. As compared to the LF method, the RK3 scheme allows a larger stable Courant number (roughly 1.73 times larger) but also requires more function evaluations per time step [15, see, e.g.,sec 2.3]. The end result is that in time-split form the two methods have similar overall effficiencies (see discussion in [22] and WS02).

In the split RK3 scheme, each of the three stages in (2.37)–(2.39) is replaced by an equivalent FB small-step cycle. In a given cycle the large-time-step terms are held fixed at the times indicated in (2.37)–(2.39) while the FB small-step system is advanced over the appropriate time range. For instance, in the first stage the large-step forcings are evaluated at time t while the small-step system is advanced through $ns/3$ small steps to arrive at time t^*. The t^* values of the fields are then used as the large-step forcings for the second stage, which is advanced through $ns/2$ small steps to arrive at time t^{**}. The t^{**} fields then provide the large-step forcings for the final stage. For consistency, ns must be a multiple of 6 (so as to be divisible by both 2 and 3). Alternatively, WS02 suggest using a single small step of length $\Delta t/3$ in the first stage regardless of ns, in which case ns just needs to be even.

To express the split RK3 scheme in matrix form, first define the three-stage

solution vector

$$\boldsymbol{\phi}^t = \begin{pmatrix} \boldsymbol{\xi}^t \\ \boldsymbol{\xi}^t \\ \boldsymbol{\xi}^t \end{pmatrix} \tag{2.40}$$

where $\boldsymbol{\xi}^t$ is the discretized approximation to $\boldsymbol{\psi}(t)$ as described previously. The analog to (2.23) is then

$$\mathbf{A} = \begin{pmatrix} \mathbf{S} & \mathbf{L} & \mathbf{0} \\ \mathbf{0} & \mathbf{I} & \mathbf{0} \\ \mathbf{0} & \mathbf{0} & \mathbf{I} \end{pmatrix} \tag{2.41}$$

where $\mathbf{S}$ and $\mathbf{L}$ are the SK92 small- and large-time-step operators as described in sections B3,4. To be clear, let $\mathbf{A}$ be the operator (2.41) with $\Delta\tau = \Delta t/ns$ (cf. appendix I) and let $\mathbf{A}'$ refer to the same operator with $\Delta\tau = \Delta t/3$. The full multi-stage SK92-RK time step suggested by WS02 can then be written in matrix form as

$$\boldsymbol{\phi}^{t+\Delta t} = \mathbf{B}\,\boldsymbol{\phi}^t$$

where

$$\mathbf{B} = \mathbf{R_3}\mathbf{A}^{ns}\,\mathbf{R_2}\mathbf{A}^{ns/2}\,\mathbf{R_1}\mathbf{A}' \tag{2.42}$$

is the net amplification matrix with

$$\mathbf{R_1} = \begin{pmatrix} \mathbf{0} & \mathbf{I} & \mathbf{0} \\ \mathbf{I} & \mathbf{0} & \mathbf{0} \\ \mathbf{0} & \mathbf{0} & \mathbf{I} \end{pmatrix}, \quad \mathbf{R_2} = \begin{pmatrix} \mathbf{0} & \mathbf{0} & \mathbf{I} \\ \mathbf{I} & \mathbf{0} & \mathbf{0} \\ \mathbf{0} & \mathbf{0} & \mathbf{I} \end{pmatrix} \quad \text{and} \quad \mathbf{R_3} = \begin{pmatrix} \mathbf{I} & \mathbf{0} & \mathbf{0} \\ \mathbf{I} & \mathbf{0} & \mathbf{0} \\ \mathbf{I} & \mathbf{0} & \mathbf{0} \end{pmatrix}$$

being the appropriate reordering/copying matrices. The eigenvalues of the amplification matrix $\mathbf{B}$ in (2.42) are then used to find the error in the scheme, as described previously in section B.

2. Parameter ranges

The RK3 scheme in unsplit form allows a larger maximum stable time step than the unsplit LF scheme (by roughly a factor of 2). But when combined with time splitting, the constraint on the smaller time step in the two schemes is roughly identical (since both use FB small-step differencing). The net implication then is that the larger stability region for the unsplit RK3 scheme translates into larger stable ns values for a given $\Delta\tau$. Consistent with this interpretation, the analysis below uses $ns = 2$, 4 and 6 rather than the $ns = 1$, 2 and 3 cases considered previously.

Apart from ns, the parameter ranges and parameter values considered below are identical to those considered for the SK92-LF case.

3. Results

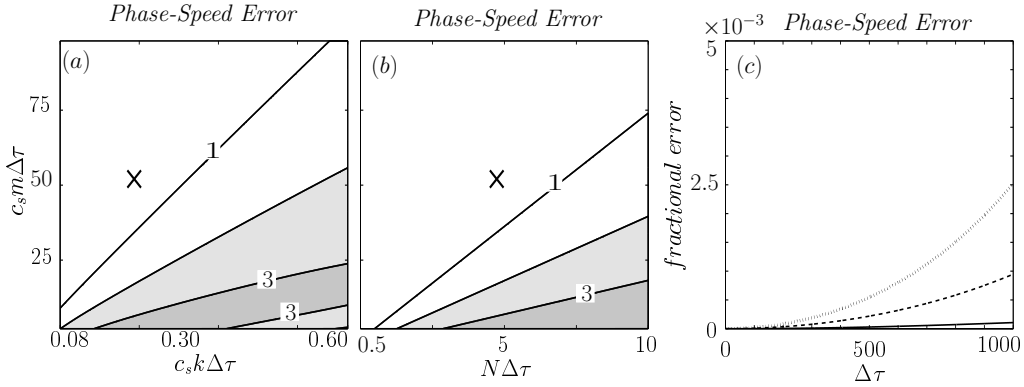

Fig. 7. Fractional phase-speed error for SK92-RK time differencing as applied to the Rossby problem. (a) phase-speed error as a function of $c_s k\Delta\tau$ and $c_s m\Delta\tau$ and (b) phase-speed error as a function of $N\Delta\tau$ and $c_s m\Delta\tau$, both for $ns = 6$ and $\Delta\tau = 500$ s [$c.i. = 1 \times 10^{-3}$; contour labels in units of 10^{-3}]. (c) error as a function of $\Delta\tau$ for $ns = 2$ (solid), 4 (dashed), and 6 (dotted) [vertical axis labels in units of 10^{-3}]. Parameter ranges and fixed reference values are as indicated in Table I.

The errors for the SK92-RK scheme are as shown in Figure 7. Figures 7a,b show

the two parameter-space cross-section plots for the case $ns = 6$ with $\Delta\tau = 500$ s. Comparison to Figs. 4a,b shows that the RK errors in this case are generally similar to but somewhat less than those of the LF scheme, despite ns being twice as large. The $\Delta\tau$ dependence for the SK92-RK errors is shown in Fig. 7c. Comparing to Fig. 4c for the case $ns = 2$ shows that for given ns the RK scheme is considerably more accurate. When the RK ns is doubled (relative to the LF case) the errors are then similar to the LF errors but still somewhat less. And as found for the LF scheme, the RK method is stable over the full range of parameters considered (not shown).

Inspection of Fig. 7c shows that the RK error depends roughly quadratically on $\Delta\tau$ and roughly cubically on ns (at least for the smaller ns values). The practical consequence is that for given $\Delta\tau$, the RK scheme can be used with larger ns (and hence larger Δt) than the LF scheme without significantly compromising accuracy. On the other hand, with increasing $\Delta\tau$ at fixed ns the errors in both schemes increase quadratically.

As found by WS02, replacing the first stage of the method with two small steps (as opposed to a single step of length $\Delta t/3$) for the case $ns = 6$ produced only small changes to the error.

F. Instability of the acoustic modes: Further details

The instability described in section C2 is evidently the same instability found by SK92 in their analysis of the acoustic-gravity wave system (see their sec. 4d and Fig. 6). The instability is also similar to that found for the acoustic-advection problem (see sec. 4a of SK92), except that here the coupling of acoustic modes with buoyancy drives the instability rather than the coupling with advection.

As with the acoustic-advection coupling, the instability seen in Figs. 1 and 2 is

closely tied to the use of leapfrog time differencing on the large time step. Recall that for the unsplit case, the instabilities of the leapfrog scheme always take the form of $4\Delta t$ (or $\omega_{rd}\Delta t = \pm\pi/2$) discrete oscillations [15, see, e.g.,sec. 2.3.4]. As a result, the time-split scheme is particularly susceptible to instability whenever the fast acoustic modes from the small time step alias onto $\omega_{rd}\Delta t = \pm\pi/2$ oscillations as seen on the large step (see discussion in SK92). Instability is also favored whenever the small-step modes alias onto $\omega_{rd}\Delta t = 0$ or $\pm\pi$ oscillations, as demonstrated below.

To address the instability more concretely, first consider the vertical acoustic mode problem

$$w^{\tau+\Delta\tau} = w^{\tau} - im\Delta\tau\,\overline{P}^{\tau} \tag{2.43}$$

$$P^{\tau+\Delta\tau} = P^{\tau} - ic_s^2 m\Delta\tau\,\overline{w}^{\tau} \tag{2.44}$$

where it should be understood that the system is to be integrated using overlapping leapfrog small-step cycles of length $2\Delta t$. However, in the absence of large-step terms, these two overlapping small-step cycles are completely independent (see the schematic in Fig. 8). That is, given the starting values $\boldsymbol{\xi}^0 = (w^0, P^0)^T$ and $\boldsymbol{\xi}^{\Delta t} = (w^{\Delta t}, P^{\Delta t})^T$ and the small-step operator $\mathbf{S}$, the solutions on the odd and even cycles as observed on the large time step are

$$\boldsymbol{\xi}^{2j\Delta t} = \mathbf{S}^{2jns}\boldsymbol{\xi}^0 \quad \text{and} \quad \boldsymbol{\xi}^{(2j+1)\Delta t} = \mathbf{S}^{2jns}\boldsymbol{\xi}^{\Delta t}$$

where j is an integer.

The use of overlapping leapfrog cycles for (2.43) and (2.44) demands four solutions: two physical modes and two computational modes. To help distinguish these modes, assume as in previous sections that ns is an integer. Then for the physical-mode solutions, the separate odd and even small-step cycles are completely

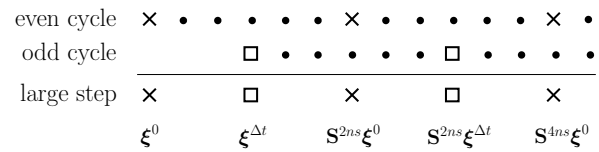

Fig. 8. Schematic illustration showing leapfrog time-splitting with $ns = 3$ as applied to the acoustic system (2.43) and (2.44). Filled dots represent small time steps with crosses and squares showing values sampled onto the large step. In the absence of large-step terms, the even and odd small-step cycles are completely decoupled.

identical—that is, $\boldsymbol{\xi}^{\Delta t} = \mathbf{S}^{ns}\,\boldsymbol{\xi}^0$ in the notation given above. The solution as seen on the large time step is then the same as integrating (2.43) and (2.44) straight through to time $nsj\Delta\tau$ (i.e., with no splitting) and then subsampling at intervals of $ns\Delta\tau$. By contrast, for the computational modes the separate odd and even small-step cycles are not identical—indeed, in the limit of good time resolution the two cycles alternate in sign, thus producing an $\omega_{rd}\Delta t = \pm\pi$ oscillation as seen on the large step [compare to the unsplit scheme as described in [15, sec 2.3.4]].

Figure 9 shows the discretized acoustic frequency ω_{rd} for (2.43) and (2.44) as integrated with leapfrog time splitting for the case $ns = 3$. The results are given in terms of the discretized phase change $|\,\omega_{rd}\,|\Delta t$ as seen on the large time step—that is, in terms of the eigenvalues of $\mathbf{RA}^{2ns}$ as described previously in section B3 [see discussion below (2.24)]. Note that the eigenvalues and associated phase changes in this case are functions of $c_s m\Delta\tau$ and ns only (and not of $c_s m$ and $\Delta\tau$ independently).

As expected, for small $c_s m\Delta\tau$ the physical-mode phase change is roughly $c_s m\Delta\tau \times ns$, while the phase change on the computational modes is roughly $\pi - c_s m\Delta\tau \times ns$. As in the unsplit case, the crossing point for the two modes occurs at $\omega_{rd}\Delta t = \pm\pi/2$. The physical mode reaches its maximum frequency of $\omega_{rd}\Delta t = \pm\pi$ at roughly $c_s m\Delta\tau = 1.1$, with larger $c_s m\Delta\tau$ then leading to aliased slower modes when sampled to the large time step. For this same range of $c_s m\Delta\tau$ the computational-mode frequency

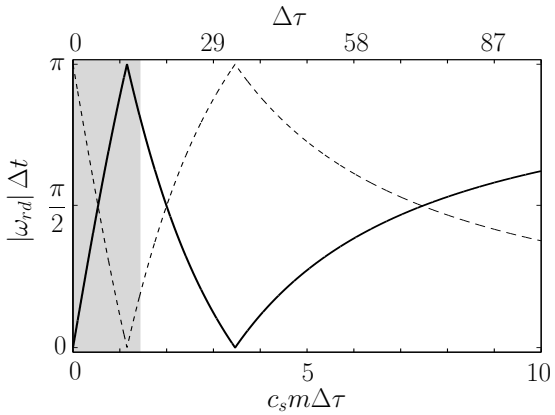

Fig. 9. Discretized acoustic frequency as seen on the large time step for leapfrog time-splitting with $ns = 3$ as applied to (2.43) and (2.44). Shown is the large–time-step phase change $|\,\omega_{rd}\,|\Delta t$ as a function of the analytic small-step change $c_s m \Delta\tau$ (bottom axis). Lines show the phase changes for the physical (solid) and computational (dashed) modes. Shading indicates values of $c_s m \Delta\tau$ smaller than those shown in Fig. 1. On the top axis is the equivalent small time step $\Delta\tau$ corresponding to the particular values of c_s and m assumed in Fig. 2.

decreases to zero and then begins to increase.[3] Further increases in $c_s m \Delta\tau$ lead to oscillations in the two frequencies, with the crossing points at $\omega_{rd}\Delta t = \pm\pi/2$. Inspection of growth rates shows that for all $c_s m \Delta\tau$ the solutions are absolutely stable (not shown).

Now suppose that buoyancy is included so that the system to be integrated becomes

$$w^{\tau+\Delta\tau} = w^{\tau} - im\Delta\tau\,\overline{P}^{\tau} + \Delta\tau\, b^{t} \tag{2.45}$$

$$b^{\tau+\Delta\tau} = b^{\tau} - \Delta\tau N^2 w^{t} \tag{2.46}$$

$$P^{\tau+\Delta\tau} = P^{\tau} - ic_s^2 m\Delta\tau\,\overline{w}^{\tau} \tag{2.47}$$

[3]Note that the interpretation given here differs slightly from that given by SK92. Specifically, SK92 only consider solutions with $\omega_{rd}\Delta t \leq \pm\pi/2$ (effectively through their choice of branch on $\sin^{-1}$) and apparently assume that all solutions in this range belong to physical modes. (See their Figs. 2 and 4 and associated discussion.)

where the buoyancy and vertical stratification terms are differenced on the large step. Analysis of (2.45)–(2.47) shows that introducing these buoyancy terms causes instability in the acoustic modes, with the instability closely matching that shown in Figs. 1f and 2b. And cross-referencing with Fig. 9 shows that the instability is present only when the acoustic frequency aliases onto the large time step with particular values—specifically, with $\omega_{rd}\Delta t = \pm\pi/2$, $\pm\pi$ or 0. (Note that the minimum $c_s m\Delta\tau$ in Fig. 1f is roughly 1.4 rather than zero. Also, an instability is in fact present at $\Delta\tau \approx 5.1$ s in Fig. 2b, although the instability in this case is weak and thus not easily visible in the figure.)

It is thus apparent that the instability shown in Figs. 1 and 2 results from the coupling of buoyancy and vertical stratification terms on the large time step with the acoustic modes as subsampled every $ns\Delta\tau$. And the instability is present only when the aliased acoustic frequency has particular values. Fortunately, integrating the buoyancy on the small step completely removes this coupling and thereby stabilizes the scheme, as indicated in section C4.

G. Summary

A series of von Neumann accuracy and stability analyses have been presented for the problems of KW78 and SK92 time splitting as applied at large scales. The particular problem of interest has been the case of large-scale Rossby-wave propagation on a resting background state.

The original KW78 splitting was shown to be surprisingly inaccurate over much of the relevant Rossby-wave parameter space. As an example, at small time step of $\Delta\tau = 100$ s the Rossby phase-speed errors exceed 10% over much of the parameter space and are in some cases as large as 100%. The source of the errors was traced to

the compressible vertical adjustment—and more precisely, to a failure of the method to maintain hydrostatic balance due to the splitting of the balance terms between the small and large time steps. The errors can be reduced somewhat through implicit biasing, but large biasing coefficients are needed—and even then the time steps are limited to moderate values.

The errors in the KW78 scheme are in large part absent from the SK92 methods, as these latter methods treat the entire vertical adjustment process on the small step. Indeed, with the SK92 splitting the time steps can be an order of magnitude larger than the time steps used for the KW78 analysis without significantly compromising large-scale accuracy. The third-order Runge-Kutta version of the SK92 scheme was shown to have a mixed quadratic (with increasing $\Delta\tau$) and cubic (with increasing ns) error dependence, whereas the leapfrog method is strictly quadratic. The practical consequence is that for given fixed $\Delta\tau$, the SK92-RK method can be used with larger ns than the LF scheme while maintaining similar overall accuracy.

It is worth noting that the Rossby problem introduced here is strictly heuristic, since the mode of interest results from a heuristic forcing term added to the equations of motion. However, a similar analysis was also developed for the Eady baroclinic wave problem (see appendicies L,M)—which lacks the added forcing term—and for the most part the Eady results echo those of the Rossby problem described above. For instance, at $\Delta\tau = 100$ s the KW78 Eady growth-rate errors are as large as 25% in some cases, and the overall error patterns are generally similar to those seen in Fig. 1. And as in the Rossby problem, the Eady errors in the KW78 scheme are largely absent from the SK92 methods.

Finally, it should be reinforced that most of the newer KW community models have already adopted the SK92 splitting out of stability concerns. However, a few of the older models—most notably the MM5 and RAMS models—still use the original

KW78 splitting. Fortunately, the standard configurations for MM5 and RAMS both use relatively large implicit biasing coefficients ($\epsilon = 0.4$ for MM5 and $\epsilon = 1.0$ for RAMS), which likely moderates the associated errors somewhat (at least for $\Delta\tau \leq$ 100 s or so—see Fig. 3). Even so, careful consideration of the large-scale accuracy of these older models is still probably in order.

H. Appendix: The Rossby-restoring model: Derivation

Analyzing difference approximations in the large-scale context raises one particular challenge: virtually all the large-scale modes of interest (the Rossby modes, the baroclinic instability modes, etc.) stem from non-constant-coefficient problems. In principle these problems are tractable numerically, but in practice the analysis tends to be cumbersome and the relevant computations are often involved. To simplify matters, this appendix is devoted to finding an appropriate test problem with constant coefficients. The particular mode of interest will be the Rossby (or planetary) wave on a resting background state.

As a starting point consider the linearized compressible-Boussinesq system on a β-plane, as described by

$$u_t = -P_x + (f_0 + \beta y)v \tag{2.48}$$

$$v_t = -P_y - (f_0 + \beta y)u \tag{2.49}$$

$$w_t = -P_z + b \tag{2.50}$$

$$b_t + N^2 w = 0 \tag{2.51}$$

$$P_t + c_s^2 \nabla \cdot \mathbf{u} = 0 \tag{2.52}$$

where f_0 and β are constants and where the remaining variables are as described in section B1. Recall that to within the quasi-geostrophic (QG) approximation the ap-

proximate governing equation for Rossby waves allows strictly 2D modes (i.e., modes with no y dependence) [23, see, e.g.,sec. 12.3.1]. The strategy here will thus be to find a 2D version of (2.48)–(2.52) that maintains the basic mechanism for Rossby wave propagation. This 2D model will then also be constant-coefficient, since the y-variation of the parameters will then be immaterial.

To begin, recall that in the QG theory the zonal wind u becomes ageostrophic in the 2D limit. The βyu term is then small in this limit (it is in fact neglected in the QG model) and (2.49) can therefore be approximated by

$$v_t = -P_y - f_0 u \ .$$

Next the heuristic assumption is made (to be justified a posteriori) that all variables other than P are strictly 2D. From (2.48) it then follows that

$$\frac{\partial}{\partial y}\left(-P_x + f_0 v + \beta y v\right) = -P_{xy} + \beta v = 0$$

which can be satisfied by letting

$$P = y \int_{-\infty}^{x} \beta v \, dx' + P'(x, z, t) \tag{2.53}$$

where it is implicitly assumed that $v \to 0$ as $x \to -\infty$.

The y-dependent term in (2.53) is recognized as the y-varying part of the total geostrophic pressure—that is, the part associated with the βy dependence of f. This term is smaller than the $P'(x, z, t)$ term—the y-varying term is in fact zero at the reference latitude—but it nonetheless introduces a small meridional pressure gradient that would otherwise be absent. In the present context this meridional pressure gradient serves as the driving force for the Rossby wave. As shown in Fig. 10, north of $y = 0$ the y-dependent pressure is positive to the east of positive v and negative to the west. South of $y = 0$ this phase relationship switches. The resulting north-

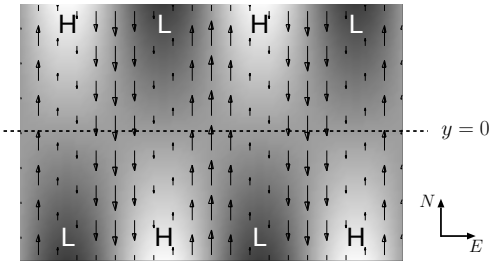

Fig. 10. Schematic illustration showing the driving mechanism for a plane monochromatic Rossby wave. Shading shows the y-varying part of the pressure disturbance [the first term on the right in (2.53)] as a function of x and y, with light shading indicating positive values and dark shading negative. Vectors show the meridional wind component. The dashed line indicates the $y = 0$ axis.

south pressure gradient then in turn drives the velocity pattern—and by extension the pressure distribution—westward and results in the westward propagation of the wave. Note for reference that this driving mechanism is not new—essentially the same driving force was identified by [24].

Finally, it is noted that for small Rossby number (R_0) the gradients of P in the x, z and t directions are all dominated by the P' term in (2.53). That is, assuming a QG scaling such that $P' \sim Lf_0|\,v\,|$, it holds that

$$\frac{y\int_{-\infty}^{x}\beta v_z\,dx'}{P'_z} \sim \frac{|\,\beta y\,|}{f_0} \ll 1$$

and similarly for the gradients in x and t. Neglecting the relevant terms in (2.50) and

(2.52) (the term in (2.48) cancels exactly) then leaves the 2D system

$$u_t = -P'_x + f_0 v \tag{2.54}$$

$$v_t = -\int_{-\infty}^{x} \beta v \, dx' - f_0 u \tag{2.55}$$

$$w_t = -P'_z + b \tag{2.56}$$

$$b_t + N^2 w = 0 \tag{2.57}$$

$$P'_t + c_s^2 \, (u_x + w_z) = 0 \tag{2.58}$$

which is indeed seen to be a constant-coefficient problem. A spatial Fourier decomposition then leads to (2.8)–(2.12) in the text.

The model system (2.54)–(2.58) supports all three standard wave types—namely, the acoustic modes, the internal gravity modes and the Rossby modes. To see this, note that the dispersion relation for the system is given by

$$\begin{aligned} \frac{\omega^5}{\nu_a^2} + \frac{\omega^4}{\nu_a^2}\frac{\beta}{k} - \omega^3 \left(\frac{N^2 + f_0^2}{\nu_a^2} + 1 \right) - \omega^2 \, \frac{\beta}{k} \left(\frac{N^2}{\nu_a^2} + 1 \right) \\ + \omega \left(\frac{f_0^2 N^2}{\nu_a^2} + \frac{N^2 k^2 + f_0^2 m^2}{k^2 + m^2} \right) + \frac{\beta}{k} \, \frac{N^2 k^2}{k^2 + m^2} = 0 \end{aligned} \tag{2.59}$$

where $\nu_a = \sqrt{c_s^2 \, (k^2 + m^2)}$ is the acoustic frequency and where the remaining parameters are as defined in section B1. For the sake of discussion it will be assumed that $\beta / | \, k \, | \ll f_0 \ll N \ll \nu_a$.

Two of the modes described by (2.59) are fast in the sense that $| \, \omega \, | \gg N$. For these modes (2.59) reduces to

$$\omega^2 \approx \nu_a^2 = c_s^2 (k^2 + m^2)$$

which is of course the standard dispersion relation for acoustic waves. If intermediate

waves are considered in the sense that $\nu_a \gg |\,\omega\,| \gg \beta/|\,k\,|$, then (2.59) becomes

$$\omega^2 \approx \frac{N^2k^2}{k^2+m^2} + \frac{f_0^2m^2}{k^2+m^2}$$

which describes the incompressible inertia-gravity modes. Finally, assuming slow modes with $|\,\omega\,| \ll f_0$ leads to

$$\omega \approx \frac{-\beta k}{k^2 + \frac{f_0^2}{N^2}m^2} \tag{2.60}$$

which is the dispersion relation for 2D QG Rossby waves.

The system (2.54)–(2.58) should in a strict sense be understood as heuristic, since one of the key assumptions of the model—namely, that P is the only field with y dependence—cannot be formally justified. Even so, the end result supports a realistic Rossby-wave mode in addition to the standard acoustic and inertia-gravity modes. (For the range of parameters considered in section C1 the Rossby frequency given by (2.54)–(2.58) never differs from the corresponding QG frequency by more than 5%. This is of course well within the error due to finite-R_0 and nonhydrostatic effects.) In this sense the system provides a realistic and convenient test case for multi-scale numerics.

I. Appendix: The Rossby **L** and **S** operators

The implicit dependence in (2.14)–(2.18) is resolved by simply solving the system for the time level $\tau + \Delta\tau$ variables algebraically. Writing out the F_q^t forcings in terms of the time level t variables then leads to an explicit system of the form (2.20).

To specify the KW78 **L** and **S** operators, first define

$$\lambda_{cx} = c_s k\Delta\tau\,, \quad \lambda_{cz} = \frac{1}{2}c_s m\Delta\tau\,, \quad \lambda_f = f_0\Delta\tau\,, \quad \lambda_N = N\Delta\tau \quad \text{and} \quad \lambda_\beta = \frac{\beta}{k}\Delta\tau\,.$$

Then

$$\mathbf{S} = \begin{pmatrix} 1-\lambda_{cx}s_3 & 0 & -\lambda_{cx}s_2 & 0 & -i\lambda_{cx}s_1/c_s \\ 0 & 1 & 0 & 0 & 0 \\ -\lambda_{cz}s_3 & 0 & s_1 & 0 & -is_2/c_s \\ 0 & 0 & 0 & 1 & 0 \\ -ic_s s_3 & 0 & -ic_s s_2 & 0 & s_1 \end{pmatrix}$$

and

$$\mathbf{L} = \begin{pmatrix} 0 & \lambda_f & 0 & -\lambda_{cx}\lambda_{cz}l_1/N & 0 \\ -\lambda_f & i\lambda_\beta & 0 & 0 & 0 \\ 0 & 0 & 0 & l_1/N & 0 \\ 0 & 0 & -N\lambda_N & 0 & 0 \\ 0 & 0 & 0 & -ic_s\lambda_{cz}l_1/N & 0 \end{pmatrix}$$

where

$$s_1 = \frac{1-\lambda_{cz}^2}{1+\lambda_{cz}^2}\,, \quad s_2 = \frac{2\lambda_{cz}}{1+\lambda_{cz}^2}\,, \quad s_3 = \frac{\lambda_{cx}}{1+\lambda_{cz}^2}\,, \quad \text{and} \quad l_1 = \frac{\lambda_N}{1+\lambda_{cz}^2}\,.$$

The **L** and **S** operators for the SK92 splitting are derived similarly.

J. Appendix: Time filtering

To control the leapfrog computational mode, the KW scheme is usually integrated with a Robert-Asselin time filter [15, sec. 2.3.5]. The filter is applied after each leapfrog time step and has the form

$$\overline{\boldsymbol{\xi}^t} = \boldsymbol{\xi}^t + \gamma\left(\overline{\boldsymbol{\xi}^{t-\Delta t}} - 2\boldsymbol{\xi}^t + \boldsymbol{\xi}^{t+\Delta t}\right) \tag{2.61}$$

where γ is a filter coefficient and where $\overline{(\ )}$ indicates a filtered variable.

According to (2.61) the eigenvalue problem for this case must account for three

time levels. The solution vector $\boldsymbol{\phi}^t$ and small-step operator $\mathbf{A}$ are thus modified to be

$$\boldsymbol{\phi}^t = \begin{pmatrix} \overline{\boldsymbol{\xi}^{t-\Delta t}} \\ \boldsymbol{\xi}^t \\ \overline{\boldsymbol{\xi}^{t-\Delta t}} \end{pmatrix} \quad \text{and} \quad \mathbf{A} = \begin{pmatrix} \mathbf{S} & \mathbf{L} & \mathbf{0} \\ \mathbf{0} & \mathbf{I} & \mathbf{0} \\ \mathbf{0} & \mathbf{0} & \mathbf{I} \end{pmatrix}$$

and the time filter is then added to the matrix $\mathbf{R}$ by defining

$$\mathbf{R} = \begin{pmatrix} \gamma\mathbf{I} & (1-2\gamma)\mathbf{I} & \gamma\mathbf{I} \\ \mathbf{I} & \mathbf{0} & \mathbf{0} \\ \gamma\mathbf{I} & (1-2\gamma)\mathbf{I} & \gamma\mathbf{I} \end{pmatrix}$$

These modifications allow for the continued use of (2.22).

Figures 11c,d show the Rossby phase-speed error and spectral radius for $ns = 2$ and for a time filtering coefficient of $\gamma = 0.1$. Comparison to the unfiltered case shows that the time filter has only a small impact on both the accuracy and stability of the scheme. As with the divergence damping, the filter actually degrades the stability at large values of N and m. Similar results are seen for the Eady problem.

K. Appendix: Divergence damping

To more selectively damp the sound waves, SK92 proposed an alternative filter that explicitly targets the divergent modes. The method works by effectively adding a second-order dissipation term to the associated equation for divergence. As an example, adding the filter to the Rossby problem (2.14)-(2.18) changes (2.14) and (2.16) to

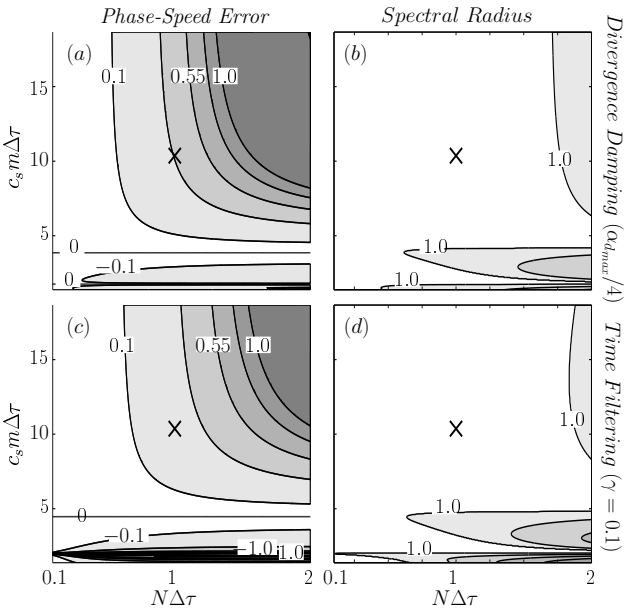

Fig. 11. Fractional phase-speed error and spectral radius for KW time differencing as applied to the Rossby problem with $ns = 2$ using divergence damping and time filtering. (a) phase-speed error [$c.i. = 0.225$] and (b) spectral radius [$c.i. = 0.6$, values larger than 1 shown] for the case with divergence damping with $\alpha_d m^2 \Delta\tau = 1/2$. (c), (d) show the analogous figures for the case with time filtering with $\gamma = 0.1$. Physical parameters and $\Delta\tau$ are as indicated in Figure 1.

$$u^{\tau+\Delta\tau} = u^{\tau} + \Delta\tau(-ikP^{\tau+\Delta\tau} - \alpha_d(k^2 u^{\tau} + mkw^{\tau}) \tag{2.62}$$

$$w^{\tau+\Delta\tau} = w^{\tau} + \Delta\tau(-im\overline{P}^{\tau} - \alpha_d(mku^{\tau} + m^2 w^{\tau}) + F_w^t) \tag{2.63}$$

where α_d is a damping coefficient. To maintain stability, the damping coefficient must satisfy $\alpha_d m^2 \Delta\tau \leq 2$ for the spectral case or $\alpha_d \Delta\tau/\Delta z^2 \leq 1/2$ for the vertically discretized case.

Figures 11a,b show the Rossby phase-speed error and spectral radius, respectively, for $ns = 2$ and for a damping coefficient satisfying $\alpha_d m^2 \Delta\tau = 1/2$. Comparison to the unfiltered case (Fig. 1f) shows that the divergence damping weakens the

instability bands somewhat but also introduces a new instability at large N and m. The filter also noticeably degrades the accuracy of the mode (cf. Fig. 1e). Further increases in α_d simply augment these changes (not shown).

In the Eady problem the combination of relatively small grid spacing and large time steps limits the size of the damping coefficient. The result is that the effect of the divergence damping in the Eady case is small (not shown).

L. Appendix: The Eady instability problem

In the previous sections, the KW78 splitting was shown to be poorly suited for modeling large-scale flows, whereas the SK92 splitting was shown to be much more accurate. However, the simplified models in these previous sections should in a strict sense be seen as heuristic, since both rely on an added forcing term to produce the slowly varying modes of interest. Here a similar analysis is carried out but as applied in a much more realistic context—specifically, the well-known Eady problem from baroclinic instability theory (e.g., [25], sec. 13.3; [23], sec. 8.4).

1. Theoretical problem setup

The basic state for the Eady problem consists of a hydrostatically and geostrophically balanced shear flow on an f-plane (i.e., $\beta = 0$) placed between two rigid boundaries; that is

$$u_0 = U(z) = \Lambda z + \overline{U}, \quad P_0 = -f_0 U y, \quad b_0 = -f_0 \Lambda y$$

where Λ is the vertical shear in the zonal wind and $\overline{U}$ is a constant. The rigid boundary heights are $z = -H/2$ and $z = H/2$ and the mean background wind is set by $\overline{U}$. The total fields are composed of the basic state and a disturbance component

as

$$u_{total} = U + u, \quad P_{total} = P_0 + P, \quad b_{total} = b_0 + b$$

where u, P and b are the disturbance quantities.

For simplicity the disturbance fields are all assumed to be 2D. This is consistent with the QG theory in that the fastest growing QG Eady mode is in fact 2D. Linearizing the compressible-Boussinesq system about the basic state and assuming a Fourier mode of the form

$$\boldsymbol{\psi} = \hat{\boldsymbol{\psi}}(z,t)\exp[ikx]$$

(cf. (2.7)) then gives

$$u_t + ikP = f_0 v - ikUu - \Lambda w \tag{2.64}$$

$$v_t = -f_0 u - ikUv \tag{2.65}$$

$$w_t + P_z = b - ikUw \tag{2.66}$$

$$b_t = -ikUb + f_0 \Lambda v - N^2 w \tag{2.67}$$

$$P_t + c_s^2\,(iku + w_z) = -ikUP + f_0 U v \tag{2.68}$$

where the carat is once again removed from the Fourier variables and where the vertical pressure advection in (2.68) has been neglected as small[4].

Consistent with previous studies (e.g., KW78; SK92; [26]; [27]) the horizontal pressure advections in (2.68) are found to have little impact on the solutions. In the analysis that follows the meridional advection term is neglected but the zonal advection is retained. The motivation for this choice is that the full system (2.64)-

[4]To see this, let $L = 2\pi/k$ and assume that the disturbance depth scale is H. The vertical velocity scales as $w \sim uH/L$ such that $w\,\partial P_0/\partial z \sim uH f_0\Lambda y/L \sim u\,\partial P_0/\partial y$ where it is assumed that $y/L \sim O(1)$. In the 2D limit $u \sim R_o v$ (where R_o is the Rossby number), implying that the vertical advection is $O(R_o)$ smaller than the meridional advection. It should be noted that the $w\,\partial P_0/\partial z$ term is the only term with explicit y-dependence. Dropping this term then allows the problem to be cast as 2D.

(2.68) is then Galilean invariant.

2. Analytic solution

The z dependence of U in (2.64)–(2.68) requires the introduction of vertical finite differencing. The domain depth H is divided into $nz-1$ vertical layers on a one-dimensional C-grid, with w defined at the layer endpoints and u, v, P, and b defined at the layer midpoints. The vertical derivatives in (2.66) and (2.68) are computed with staggered centered differences over a distance of Δz. The boundary conditions at the top and bottom are $w_1 = w_{nz} = 0$.

The number of grid points on the w grid is given by $nz = 26$, which is large enough that the vertical discretization error is small (as verified through convergence testing). Defining a solution vector of length $N = 5nz - 4$ by

$$\boldsymbol{\psi} = (u_{1\cdots nz-1}, v_{1\cdots nz-1}, w_{1\cdots nz}, b_{1\cdots nz-1}, P_{1\cdots nz-1})^T$$

(where subscripts indicate the vertical level) then allows the discretized form of (2.64)–(2.68) to be cast in the form (2.13), where $\mathbf{M}$ is now an $N \times N$ coefficient matrix. As before, the frequencies and growth rates in the system are completely determined by the eigenvalues of $\mathbf{M}$. The Eady mode is then selected as the mode with the largest growth rate.

3. Discretized solution

To obtain the discretized problem, the continuous time derivatives in (2.13) are replaced by KW time differencing. Details of this differencing are given in appendix M. The associated solutions are then obtained by first defining the discretized solution vector

$$\boldsymbol{\xi}^t = \left(u^t_{1\cdots nz-1}, v^t_{1\cdots nz-1}, w^t_{1\cdots nz}, b^t_{1\cdots nz-1}, P^t_{1\cdots nz-1}\right)^T \tag{2.69}$$

of length N and substituting into (2.21) to obtain $\boldsymbol{\phi}^t$. As before, the full discretized equations are then recast into the form (2.22), where the $\mathbf{A}$ operator (2.23) again advances $\boldsymbol{\phi}^t$ forward a single small step. The derivation of this $\mathbf{A}$ operator is somewhat involved in this case and is given in appendix M. Once obtained, the eigenvalues of the $\mathbf{RA}^{2ns}$ matrix again determine the frequencies and growth rates of the discretized wave modes.

The discretized Eady mode is selected as the mode with complex frequency most closely matching that of the analytic solution. The growth rate or imaginary part of this frequency is used to measure the fractional discretization error in the scheme according to

$$\varepsilon_g = \frac{\omega_{id} - \omega_{ia}}{\omega_{ia}} \tag{2.70}$$

where as before the subscripts d and a represent *discretized* and *analytic*.

4. Parameter ranges

The Eady parameter space differs from the corresponding Rossby case in two ways: (i) the Rossby driving parameter β/k is replaced by the baroclinic shear parameter Λ; and (ii) the vertical wavelength $\lambda_z = 2\pi/m$ is replaced by the domain depth H. To allow comparison with the Rossby results the domain depth will be measured in terms of the wavenumber of the deepest mode; that is, $m = \pi/H$. This choice reflects the spectral characteristics of the mode as well, since the most unstable Eady mode is relatively deep.

As in the Rossby problem, the Eady error is most sensitive to changes in N, $c_s k$ and $c_s m$. The ranges for these three parameters are found in Table II. Parameters not being varied are again held fixed at reference values, as given in the middle row of Table II. Except where indicated, all calculations are for zero mean wind (i.e.,

Table II. Parameter values for the Eady problem.

parameter	$c_s(ms^{-1})$	$f_0(s^{-1})$	$\Lambda(s^{-1})$	$N(s^{-1})$	$\lambda_x(km)$	$H(km)$
reference value	330	10^{-4}	.004	.01	4000	10
range	–	–	–	.001-.02	2000-12500	6-75

$\bar{U} = 0$). The time step for the cross section plots is again $\Delta\tau = 100$ s. As in the Rossby problem, the Eady mode at this time step is extremely well-resolved in time ($|\,\omega\Delta\tau\,| \simeq 1.15 \times 10^{-3}$).

Two additional procedures are followed when mapping the Eady results. First, cases with both analytic and discretized growth rates less than 0.1 day^{-1} are discarded so as to avoid showing marginal cases with large errors. This means that solutions are generally discarded at small m, since for fixed k and N the Eady mode is stable at large H. Second, cases for which the intrinsic frequency ($k(U-c)$) exceeds the inertial frequency (f) at some height are also discarded so as to avoid showing modes of mixed type.

Since the Eady mode is unstable, numerical instability in the scheme is indicated by the spectral radius error rather than the spectral radius itself. Defining an equivalent analytic spectral radius for the Eady mode by $s_a = \exp(\omega_{ia}\Delta t)$, the fractional error is then

$$\varepsilon_s = \frac{s_d - s_a}{s_a} \tag{2.71}$$

where s_d is the spectral radius for the discretized problem (including all modes). Note that since the analytic growth rates are small, the analytic spectral radius is always close to one.

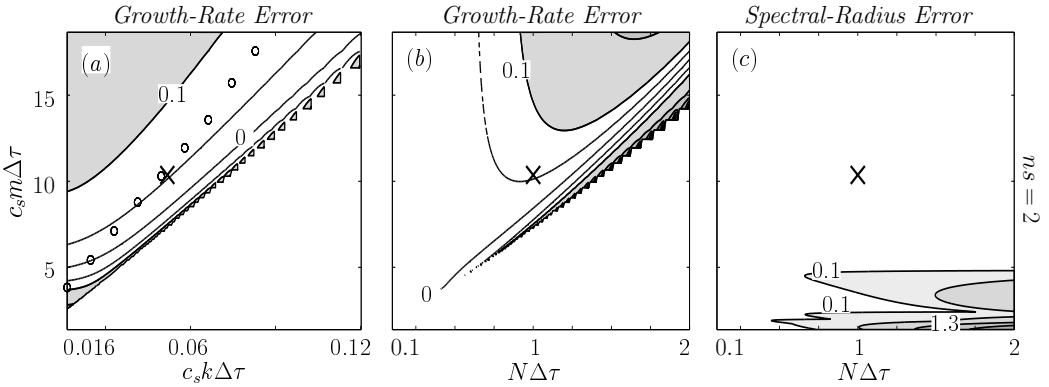

Fig. 12. Fractional growth-rate and spectral-radius errors for the Eady problem under KW78 time differencing with $ns = 2$. (a) growth-rate error as a function of $c_s k\Delta\tau$ and $c_s m\Delta\tau$ [$c.i. = 0.15$ for shaded contours, 0.05 for unshaded], (b) growth-rate error as a function of $N\Delta\tau$ and $c_s m\Delta\tau$ [contours as in (a)], and (c) spectral-radius error [$c.i. = 0.6$; values greater than 0.1 shown]. All parameter ranges and reference values are as shown in Table II. The reference values for N, λ_z, and λ_x are marked by a cross in each panel.

5. Results

Figure 12 shows the growth-rate error (2.70) and spectral-radius error (2.71) for the Eady problem as computed using the KW78 splitting with $ns = 2$. The layout of the figure is similar to that described previously for Fig. 1. Shading indicates growth-rate errors greater than 10% in Figs 12a,b and spectral-radius errors greater than 10% in Fig. 12c. For reference, circles in Fig. 12a show the zonal wavenumber of largest analytic growth rate (that is, the most unstable normal mode) for a given value of m.

Figures 12a,b show that throughout much of the relevant parameter space the KW78 growth-rate error is greater than 5%. As in the Rossby case, the error is greatest for modes with small aspect ratio k/m (Fig. 12a) and increases with increasing N (Fig. 12b). Indeed, apart from the deep-domain cutoff at small m, the overall error patterns and ns dependence (not shown) in the Eady case are very similar to those seen in Fig. 1. The instability bands in Fig. 12c are similar to the Rossby problem as

well.

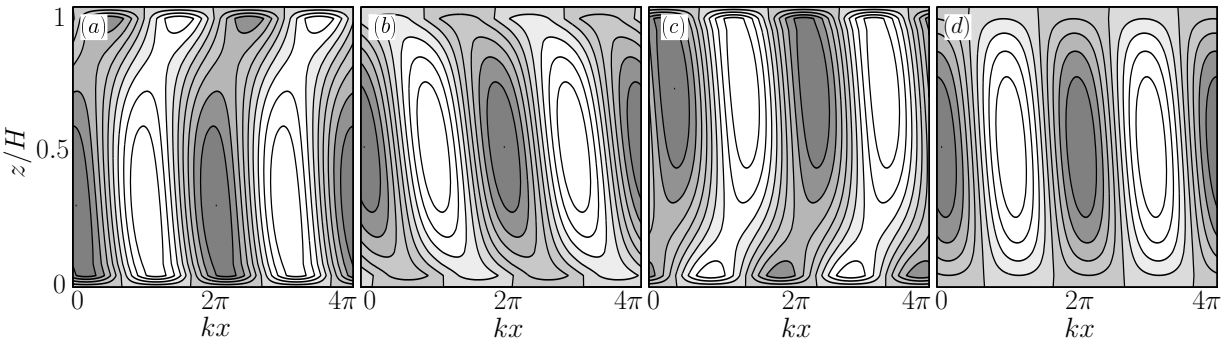

Fig. 13. Effect of background wind speed on the KW78 Eady solution. Shown is the vertical velocity field for $ns = 1$ and $\Delta\tau = 100$ s with (a) $\bar{U} = -\Lambda H/2$, (b) $\bar{U} = 0$ and (c) $\bar{U} = \Lambda H/2$. (d) shows the corresponding theoretical solution. Results are normalized by the maximum value in each panel so that the number of contours is the same. All other parameter values are fixed at the reference values indicated in Table II.

The dependence of the KW78 Eady mode on the background wind speed $\overline{U}$ (at fixed Λ) is shown in Figure 13. As discussed in section L1, the continuous problem is Galilean invariant so that the analytic mode structure has no $\overline{U}$ dependence. The vertical velocity for this analytic mode is shown in Fig. 13d. The discretized modes for the cases with $\overline{U} = -\Lambda H/2$, 0, and $\Lambda H/2$ are shown in Figs. 13a-c. In all three cases the discretized w field is distorted, with larger distortion for the cases with nonzero $\overline{U}$. The growth-rate error increases with $|\,\overline{U}\,|$ as well (not shown).

The effect of implicit biasing on the KW78 Eady solutions (with $\overline{U} = 0$) is shown in Fig. 14. As in the Rossby problem, both the stability and accuracy of the scheme improve as ϵ increases. However, even at $\epsilon = 0.2$ the errors are still significant.

Finally, calculations for the SK92 splitting show results similar to those of the Rossby problem—specifically, fractional growth-rate errors on the order of 10^{-4} and no instability bands at $\Delta\tau = 100$ s. As shown in Fig. 15, the SK92 splitting also corrects the Eady vertical motion field (cf. Fig. 13). And unlike the KW78 case, the

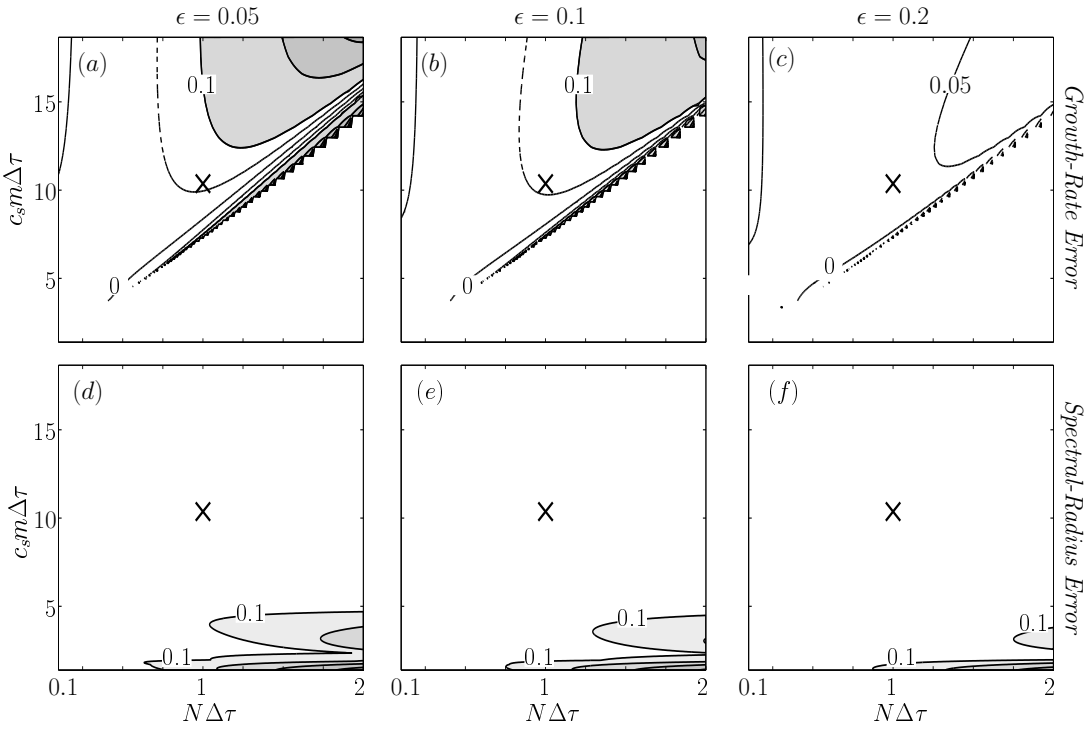

Fig. 14. Effect of implicit biasing on the KW78 Eady solution. Shown are the fractional growth-rate and spectral-radius errors for $ns = 2$. (a)-(c) growth-rate error [*c.i.* as in Fig. 12] for $\epsilon =$ (a) 0.05, (b) 0.1, and (c) 0.2. (d)-(f) show the corresponding spectral-radius errors [$c.i. = 0.6$, values larger than 0.1 shown]. Parameter ranges and fixed reference values are as given in Table II.

SK92 splitting preserves the Galilean invariance of the problem.

It should be noted that the results of this section have been verified through independent time integrations. That is, initializing (2.72)-(2.76) with random noise and integrating does in fact produce the Eady modes described above.

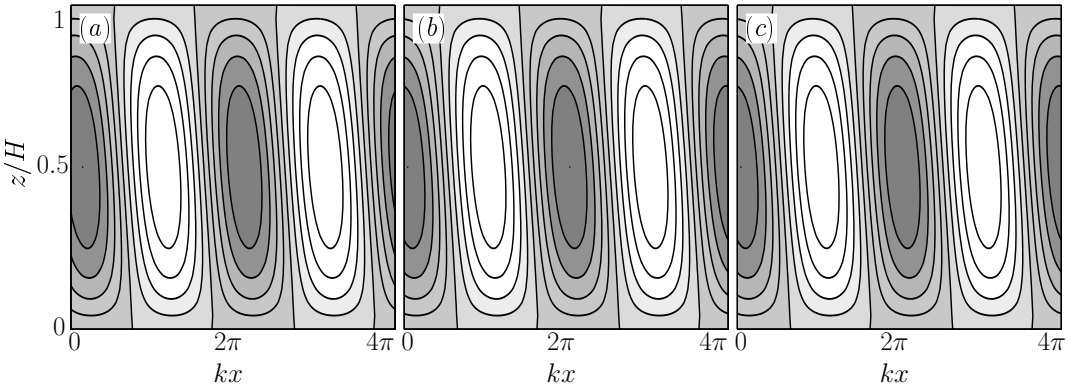

Fig. 15. As in Fig. 13a-c but for the SK92 formulation.

M. Appendix: Deriving the Eady **A** Matrix

The vertically discretized and KW78 time-discretized versions of (2.64)-(2.68) are given by

$$u_k^{\tau+\Delta\tau} = u_k^\tau + \Delta\tau(-ikP_k^{\tau+\Delta\tau} + F_{u,k}^t) \tag{2.72}$$

$$v_k^{\tau+\Delta\tau} = v_k^\tau + \Delta\tau F_{v,k}^t \tag{2.73}$$

$$w_k^{\tau+\Delta\tau} = w_k^\tau + \Delta\tau(-\overline{\delta_z P_{k-1/2}}^\tau + F_{w,k}^t) \tag{2.74}$$

$$b_k^{\tau+\Delta\tau} = b_k^\tau + \Delta\tau F_{b,k}^t \tag{2.75}$$

$$P_k^{\tau+\Delta\tau} = P_k^\tau + \Delta\tau(-ic_s^2 k u^\tau - c_s^2\overline{\delta_z w_{k+1/2}}^\tau + F_{P,k}^t) \tag{2.76}$$

where the subscript k indicates the vertical level and where the terms included on the large time step (F_q^t) are given by the RHS of (2.64)–(2.68). The vertical averaging and differencing operators are defined by

$$\overline{q}_k^z = \frac{q_{k+1/2} + q_{k-1/2}}{2} \text{ and } \delta_z q_k = \frac{q_{k+1/2} - q_{k-1/2}}{\Delta z} .$$

The discretized eigenvalue problem involves first deriving the small-step operator **A** as in section B3. To begin, the discretized solution vector (2.69) is substituted into (2.21) to obtain the two-level solution vector $\boldsymbol{\phi}^t$. In the following, it is assumed that

the upper half of $\boldsymbol{\phi}^t$ is evaluated at time τ, with the understanding that initially $\tau = t - \Delta t$. The goal is then to decompose the upper half of $\mathbf{A}$ into five blocks, each satisfying

$$q_k^{\tau+\Delta\tau} = a_{k,j}^q \phi_j^t \tag{2.77}$$

where $a_{k,j}^q$ represents the portion of $\mathbf{A}$ that advances q forward a single small step. The matrix $a_{k,j}^w$ has dimensions $nz \times 2N$ while the other four blocks have dimensions $(nz-1) \times 2N$.

The first step in deriving these blocks is to reexpress the explicit terms in (2.72)-(2.76) in terms of an explicit matrix $c_{k,j}^q$ multiplied by the solution vector ϕ_j^t. For example, the explicit terms in (2.74) are expressed as

$$w_k^\tau - \frac{\Delta\tau}{2}\delta_z P_{k-1/2}^\tau + \Delta\tau F_{w,k}^t = c_{k,j}^w \phi_j^t \tag{2.78}$$

This notation is used to rewrite (2.72)-(2.76) as

$$u_k^{\tau+\Delta\tau} = -ik\Delta\tau P_k^{\tau+\Delta\tau} + c_{k,j}^u \phi_j^t \tag{2.79}$$

$$v_k^{\tau+\Delta\tau} = c_{k,j}^v \phi_j^t \tag{2.80}$$

$$w_k^{\tau+\Delta\tau} = -\frac{\Delta\tau}{2}\delta_z P_{k-1/2}^{\tau+\Delta\tau} + c_{k,j}^w \phi_j^t \tag{2.81}$$

$$b_k^{\tau+\Delta\tau} = c_{k,j}^b \phi_j^t \tag{2.82}$$

$$P_k^{\tau+\Delta\tau} = -\frac{c_s^2\Delta\tau}{2}\delta_z w_{k+1/2}^{\tau+\Delta\tau} + c_{k,j}^P \phi_j^t \tag{2.83}$$

Equations (2.80) and (2.82) already have the form (2.77), so that the small step blocks $a_{k,j}^v$ and $a_{k,j}^b$ are given by $c_{k,j}^v$ and $c_{k,j}^b$, respectively. The remaining blocks are derived by combining (2.81) and (2.83) to give

$$q_k w_{k+1}^{\tau+\Delta\tau} + r_k w_k^{\tau+\Delta\tau} + s_k w_{k-1}^{\tau+\Delta\tau} = c_{k,j}^e \phi_j^t \tag{2.84}$$

where q_k, r_k, and s_k are scalars and

$$c^e_{k,j} = c^w_{k,j} - \frac{\Delta\tau}{2}\delta_z c^P_{k-1/2,j}$$

and where only the repeated j index implies a sum.

The derivation of the $a^w_{k,j}$ small-step block then follows a standard tridiagonal matrix algorithm, but with the right-hand-side terms recast as matrix row operations rather than scalars. To begin, first rewrite (2.84) for $k = 2$ as

$$q_k w^{\tau+\Delta\tau}_{k+1} + \alpha_k w^{\tau+\Delta\tau}_k = \beta_{k,j}\phi^t_j \tag{2.85}$$

(since $w^{\tau+\Delta\tau}_1 = 0$) where $\alpha_2 = r_2$ and $\beta_{2,j} = c^e_{2,j}$ and where again only the repeated j index is summed. The forward pass of the solver then carries this form up to $k = nz - 1$, with recursion relations

$$\begin{aligned} \alpha_k &= r_k - \tfrac{s_k}{\alpha_{k-1}} q_{k-1} \\ \beta_{k,j} &= c^e_{k,j} - \tfrac{s_k}{\alpha_{k-1}} \beta_{k-1,j} \end{aligned}$$

Using the upper boundary condition $w^{\tau+\Delta\tau}_{nz} = 0$ leads to

$$w^{\tau+\Delta\tau}_{nz-1} = \frac{\beta_{nz-1,j}}{\alpha_{nz-1}}\phi^t_j \quad \text{implying} \quad a^w_{nz-1,j} = \frac{\beta_{nz-1,j}}{\alpha_{nz-1}}$$

and the recursion relation for the backward pass follows from (2.85) as

$$w^{\tau+\Delta\tau}_k = a^w_{k,j}\phi^t_j$$

where

$$a^w_{k,j} = \frac{\beta_{k,j} - q_k a^w_{k+1,j}}{\alpha_k} \tag{2.86}$$

Continuing (2.86) down to $k = 2$ and setting $a^w_{1,j} = a^w_{nz,j} = 0$ then completes the derivation. The rows of $a^w_{k,j}$ can then be used to solve for $a^P_{k,j}$ and $a^u_{k,j}$ by substitution

into (2.83) and (2.79).

Once obtained, the five small-step blocks can be combined to form the complete small-step operator **A** according to

$$a_{i,j} = \begin{cases} a^u_{k,j} \text{ , for } i \leq nz-1, \text{ with } k = i; \\ a^v_{k,j} \text{ , for } nz-1 < i \leq 2nz-2, \text{ with } k = i-(nz-1); \\ a^w_{k,j} \text{ , for } 2nz-2 < i \leq 3nz-2, \text{ with } k = i-(2nz-2); \\ a^b_{k,j} \text{ , for } 3nz-2 < i \leq 4nz-3, \text{ with } k = i-(3nz-2); \\ a^P_{k,j} \text{ , for } 4nz-3 < i \leq N, \text{ with } k = i-(4nz-3); \\ \delta_{i,j} \text{ , for } N < i \leq 2N \end{cases}$$

where $a_{i,j}$ now has the dimensions $2N \times 2N$.

As in the Rossby case, the SK92 splitting entails modifying (2.74) and (2.75) to integrate the buoyancy and vertical stratification terms on the small step. The derivation of the small-step operator then follows as above, except that the modified form of (2.75) is used in the derivation of (2.84).

CHAPTER III

BACKGROUND AND OBJECTIVES FOR RESONANT INSTABILITY STUDY

A. Orographically-forced resonant instability and wave breaking

The breaking of mountain waves has been of interest for some time due to impacts such as clear-air turbulence and downslope windstorms. Breaking occurs when the streamlines in the wave pattern overturn and place denser fluid over lighter fluid, creating a dynamically-unstable environment. Some well-known factors that tend to favor wave breaking include large nondimensional terrain height and strong vertical gradients in the larger-scale flow. However, a new pathway to wave breaking involving a resonant triad instability has recently been identified for hydrostatic flow. This new instability leads to breaking at significantly smaller mountain heights than the more well-known breaking mechanisms. The present section gives an overview of basic mountain-wave theory and wave breaking and briefly summarizes the idea of the resonant triad instability in mountain waves.

1. Basic mountain wave dynamics: linear theory

The linear theory for mountain waves describes the limit of small nondimensional terrain height Nh/U, where N is the buoyancy frequency, h is the maximum height of the terrain, and U is the background wind speed. The remaining parameters are then based on the terrain width L: specifically, the aspect ratio $\delta = U/NL$ and the Rossby number $R_0 = U/fL$, where f is the Coriolis parameter. Physically, these two parameters relate the advective frequency U/L to the background static stability and inertial frequencies, respectively. For small δ the flow is essentially hydrostatic, while for large R_0 the flow is nonrotating.

The dependence of the linear waves on δ and R_0 was explored by the early works of [28, 29], and others [25, see the summary in sec. 8.8]. Assuming $\delta/R_0 = f/N \sim O(0.01)$ for the atmospheric case, the solution allows five flow regimes: (i) potential flow [$\delta \gg 1$]; (ii) nonhydrostatic [$\delta \sim O(1)$]; (iii) hydrostatic nonrotating [$\delta \ll 1$, $R_0 \gg 1$]; (iv) rotating [$R_0 \sim O(1)$]; and (v) quasi-geostrophic [$R_0 \ll 1$]. Since $R_0 \sim 100\delta$, the first two regimes have $R_o \gg 1$ (nonrotating), while the last two have $\delta \ll 1$ (hydrostatic).

The above regimes can be subdivided into those which produce internal waves and those which do not. Those with advective frequencies which are faster than the buoyancy frequency N or slower than the inertial frequency f do not produce waves. This corresponds to the potential flow and quasi-geostrophic regimes, respectively. The remaining regimes produce waves to some degree, with the differences between the regimes determined mainly by differences in dispersion.

In the nonhydrostatic case the wave energy propagates upward and downstream, with the raypaths becoming more vertically oriented as δ decreases. The surface drag and acceleration patterns are relatively weak with the wind maxima located only slightly downstream of the crest. As δ decreases to $\delta \ll 1$ the hydrostatic nonrotating regime becomes valid. In this regime the wave energy is propagated upward above the ridge and the surface wind pattern is anti-symmetric about the ridge crest. The largest winds are roughly halfway down the lee slope, with the wind amplitude and the surface drag both larger than in the nonhydrostatic case.

Further increase in the width of the ridge leads to the rotating regime. In this regime the waves disperse upward and downstream much as in the nonhydrostatic case, but with the addition of a pronounced inertial wave train along the lee-side surface. As R_0 decreases the surface drag and wind acceleration decrease in amplitude, but the lee surface wind pattern becomes much more complex due to the prominent

inertial waves. It should be noted that the linear theory has been developed extensively for the nonrotating regimes while the rotating regime has only been examined in a few studies [28, 30, 31]. This is despite the fact that many prominent mid-latitude mountain ranges have dominant length scales near $R_0 \sim 1$.

2. Nonlinear effects: Long's theory and wave breaking

The study of nonlinear effects in mountain waves began with the theoretical and laboratory studies of [9, 32]. Long showed that for steady-state flow with a particular set of flow conditions – namely, 2D, nonrotating flow with constant background wind U and static stability N – the full nonlinear equations of motion could be reduced to a single linear Helmholtz equation for the streamfunction. This reduction allows for relatively simple solutions, with the nonlinear effects coming entirely from the nonlinear lower boundary condition.

The solutions to Long's equation show that as the nondimensional terrain height Nh/U is made larger, the streamlines in the associated wave pattern become steeper [32, 33, e.g.]. At some critical terrain height the streamlines overturn, causing the steady-state flow pattern to be dynamically unstable. Long compared this theoretical result to laboratory studies and showed that at the critical overturning value the wave indeed breaks down into turbulence. Numerous other laboratory studies have confirmed this result over the years [34, chap. 5].

While Long's solution describes the steepening and overturning of the wave at steady state, the theory does not account for the actual turbulent wave breakdown. Our understanding of the wave breaking process thus comes mainly from numerical calculations and observations. A number of studies [35, 36, e.g.] have shown that one of the most important consequences of wave breaking is the production of a weak stability (or well-mixed) region in the turbulent overturning zone. This weak-stability

layer tends to focus wave energy below it, causing an hydraulic-like acceleration that can ultimately lead to a downslope windstorm. This transition to the windstorm state has the character of a bifurcation [37, e.g.], in that the surface drag and lee-slope winds both increase abruptly as the wave breaks. The turbulent dissipation in the mixed layer also leads to the generation of potential vorticity [38] and an associated divergence in the wave vertical momentum flux. The result is the formation of a wake of reversed or decelerated flow downstream [39, 40].

Roughly speaking, wave breaking occurs wherever the local value of Nh/U becomes sufficiently large (where h is now the local streamline displacement in the vertical). The most studied case of wave breaking is the case of large terrain heights in a constant N and U background, but vertical gradients in the background flow can also play a significant role. An increase in N due to propagation into the stratosphere or a decrease in U due to background shear can both increase the local value of Nh/U, leading to steepening and breaking. Wave breaking can also be due to the decrease in density with height, since the reduced density leads to larger disturbance winds and thus effectively larger wave amplitudes [41, e.g.]. This density effect plays an important role in the stratosphere and mesosphere, but has only a minor influence on tropospheric waves.

A growing number of studies have reported in-situ observations of wave breaking, including those by [42, 43, 44, 45]. These studies show consistency with the numerical studies in terms of the location of the turbulence and the formation of a mixed layer. They have also shown that wave breaking can result in severe clear-air turbulence, which can occasionally be dangerous to aircraft.

3. Nonlinear effects in rotating flows

Compared to the nonrotating problem, relatively few studies have explored nonlinear effects in rotating mountain waves [46, 47, 48, 49, 30, 50]. All of these studies are strictly numerical, since Long's solution is invalid with rotation. The main interest in most of these studies has been upstream blocking and surface barrier winds. Only [47] appears to have systematically explored the wave fields aloft.

[47] used a nonlinear hydrostatic model to simulate flows for varied R_0 and Nh/U. They found that for small and intermediate values of Nh/U, the progression of the waves with R_0 is rather similar to that seen in linear theory, with the exception of wave steepening over the peak. However, for larger Nh/U and intermediate R_0 ($R_0 \approx 0.5$) there is a secondary steepening region downstream. They attributed this secondary steepening to nonlinear modification of near-inertial waves, which effectively acts as a source for new buoyancy waves. It was also shown that while flows with small R_0 and small Nh/U are effectively quasi-geostrophic, increasing Nh/U for these flows leads to prominent inertia-gravity waves in the lee, presumably from nonlinear scale collapse.

4. Resonant wave-wave instability

Current understanding of wave breaking is based mainly on the steady-state theories presented in the previous sections (particularly Long's theory). The basic assumption is that the steady-state wave pattern steepens with increasing Nh/U until a critical overturning height is reached, and at that point and instability causes turbulent wave breakdown. However, instability and breaking could occur at smaller Nh/U as well with the onset of resonant wave-wave interactions [13], a process that is not seen in the standard steady-state analysis. These interactions are expected to be most

prevalent for cases with multiple peaks and complex terrain, but are also present in the single peak case.

The idea of nonlinear resonant instability was first introduced by [10] in the context of surface gravity waves and later examined for internal gravity waves by [11], [12], and [51], among others. Given some set of nonlinear equations and an envelope of normal mode solutions $\phi = \sum_{n=1}^{N} A_n \exp(i\mathbf{k}_n \cdot \mathbf{x} - \omega_n t)$, where $\mathbf{k}_n$ is a wavenumber vector and ω_n is the frequency, it can be shown that interactions between these normal modes may lead to linearly unstable resonant triads. If some subset of solutions in the envelope meets the resonant-interaction criteria

$$\mathbf{k}_1 + \mathbf{k}_2 = \mathbf{k}_3; \quad \omega_1 + \omega_2 = \omega_3 \tag{3.1}$$

where $\omega_n > 0$, it will form a resonant triad in which the amplitude of one or two of the wave modes will grow at the expense of the other(s). Thorough reviews of resonant wave instability can be found in [52], [53], and [54, sec. 7.51].

The study of resonant instability in orographically-forced gravity waves is relatively new. [55] performed hydrostatic simulations for flow over periodic topography and found instances in which the solutions could not reach a steady state. After ruling out numerical instability through resolution tests, they attributed the problem to a resonant physical instability, but did not investigate further. More recently, [13] have explored the stability of Long's steady-state solution for the case of nonrotating flow past a two-peak terrain profile. Their results show that Long's solution is unstable for terrain heights less than half the critical values needed for steady-state wave overturning. A Fourier analysis showed that the resonant instability consists of two oppositely propagating wavepackets that resonantly reinforce each other through an interaction with the background Long's flow. The growth rates of the instability are relatively small but are large enough to be relevant on synoptic timescales.

B. Objectives

The operational prediction of mountain-wave breaking has recently become a topic of interest, particularly for aviation and military applications. The resonant instability described by [13] has potential implications for this problem, since the growth of the instability modes is unlikely to be predictable. The instability also leads to breaking at much smaller terrain heights than would otherwise be expected. However, the formal study of this instability has to date been limited to a single special case: hydrostatic nonrotating flow past a two-peak terrain profile [13].

The following study seeks to extend the study of resonant wave-wave instability in mountain waves to the rotating wave regime. In the process, the nonlinear steady-state solutions of Long must be extended to the rotating problem. To simplify matters, analysis is limited to the case of flow past a single Gaussian peak in 2D. The specific objectives then include:

- To develop a steady solver to extend Long's steady-state solution to the rotating wave regime
- To use the steady solver to find the critical wave overturning heights for rotating flow as a function of $\mathcal{R} = 1/R_0$
- To map the onset and growth rates of the resonantly unstable modes through linear stability analyses about the steady states as a function $\mathcal{R} = 1/R_0$

CHAPTER IV

A NEWTON SOLVER FOR NONLINEAR WAVES WITH ROTATION

A. Introduction

Instabilities in numerical models, be they physical or computational, prevent the use of time integration for reaching steady solutions. The current study seeks to examine a resonant instability in mountain waves which has only been examined for hydrostatic nonrotating flow by Lee et. al. [13], who used the analytic Long's solution for this very reason. As such, a steady solver must be developed in order to avoid time dependent growth of the instability.

B. The Newton solver and computational methods

1. Basic equations

A Newton solver is developed for the problem of steady, 2D flow past finite-amplitude topography on an f-plane. To simplify matters, the flow is assumed both hydrostatic and Boussinesq, although the extension to more general cases is expected to be straightforward.

The solver is formulated in the vorticity-streamfunction framework, with the disturbance velocity components u^* and w^* given by

$$u^* = {\psi^*}_{z^*} \quad \text{and} \quad w^* = -{\psi^*}_{x^*} \tag{4.1}$$

where ψ^* is the disturbance streamfunction, subscripts indicate partial derivatives with respect to the given spatial coordinate and asterisks indicate dimensional variables. To simplify the numerics, a reference state is defined with constant wind U

and uniform static stability N. The total streamfunction variable is then given by

$$\Psi^* = Uz^* + \psi^* \tag{4.2}$$

while the total Boussinesq potential temperature variable is

$$\Theta^* = \theta_r(z^*) + b^* \tag{4.3}$$

where $\theta_r(z^*) = N^2 z^*$ is the reference potential temperature profile and b^* is the disturbance buoyancy. For the moment, this constant reference state is also assumed to be the background (or upstream) state for the flow. The extension to more general background states is presented in section E.

Under the hydrostatic approximation, the y-component of the vorticity reduces to $\eta^* = u^*{}_{z^*} = \psi^*{}_{z^*z^*}$. The steady dimensional equations for 2D hydrostatic rotating flow in Cartesian coordinates can then be written

$$(U + \psi^*{}_{z^*})[\psi^*{}_{z^*z^*}]_{x^*} - \psi^*{}_{x^*}[\psi^*{}_{z^*z^*}]_{z^*} = -b^*{}_{x^*} + fv^*{}_{z^*} \tag{4.4}$$

$$(U + \psi^*{}_{z^*})b^*{}_{x^*} - \psi^*{}_{x^*}b^*{}_{z^*} - N^2\psi^*{}_{x^*} = 0 \tag{4.5}$$

$$(U + \psi^*{}_{z^*})v^*{}_{x^*} - \psi^*{}_{x^*}v^*{}_{z^*} = -f\psi^*{}_{z^*} \tag{4.6}$$

where (4.4) is the Boussinesq vorticity equation, v^* is the y-component of the velocity and f is the Coriolis parameter.

Since the flow is both steady and inviscid, the lower boundary is both a streamline for the flow and an isentropic surface. The conditions for ψ^* and b^* at the boundary are then

$$\psi^*(z^* = h^*) = -Uh^* \quad \text{and} \quad b^*(z^* = h^*) = -N^2 h^* \tag{4.7}$$

where $h^*(x^*)$ is the terrain profile. The topography is assumed localized so that b^*, v^*

and $\boldsymbol{\nabla}\psi^*$ all vanish as $|\, x^* \,| \to \infty$. The domain is in principle taken to be unbounded aloft. Note that v^* does not have an explicit lower boundary condition, suggesting that the appropriate condition for v^* at the boundary is simply (4.6).

2. Scale analysis and computational coordinates

For scaling purposes, the topography profile $h^*(x^*)$ is assumed to have a characteristic length scale L and a maximum height h_0. The basic equations, (4.4)-(4.6) are then nondimensionalized according to

$$x^* = Lx; \qquad z^* = \frac{U}{N}z; \quad h^* = h_0 h; \qquad \psi^* = \frac{U^2}{N}\psi; \quad b^* = NU\phi; \qquad v^* = fLv;$$

where asterisks again indicate dimensional variables. Substituting into (4.4)-(4.6) then yields two nondimensional control parameters: the nondimensional mountain height $\epsilon = Nh_0/U$, which measures nonlinear effects, and the inverse Rossby number $\mathcal{R} = fL/U$, which measures the importance of rotation.

The solver is formulated in the terrain-following nondimensional coordinates

$$X = x; \quad q = q(x, z);$$

where

$$q(x, z) = \frac{z - \epsilon h}{z_T - \epsilon h} z_T \tag{4.8}$$

is the standard terrain-following coordinate of Gal-Chen and Somerville [56], with z_T being the depth of the solver domain. The resulting equations can be put in terms of

ψ, ϕ, and v as

$$\begin{aligned}(1+\psi_q q_z)[\psi_{qqX}(q_z)^2 + 2\psi_{qq}q_z q_{xz}] + (q_x - \psi_X q_z)\psi_{qqq}(q_z)^2 + \phi_X \\ + \phi_q q_x - \mathcal{R}^2 v_q q_z = 0\end{aligned} \tag{4.9}$$

$$(1+\psi_q q_z)\phi_X + (q_x - \psi_X q_z)\phi_q - \psi_X - \psi_q q_x = 0 \tag{4.10}$$

$$(1+\psi_q q_z)v_X + (q_x - \psi_X q_z)v_q + \psi_q q_z = 0 \tag{4.11}$$

where the vorticity is now $\eta = \psi_{qq}(q_z)^2$.

In nondimensional form the lower boundary conditions (4.7) become

$$\psi(q=0) = -\epsilon h \quad \text{and} \quad \phi(q=0) = -\epsilon h \tag{4.12}$$

while the condition for v at the boundary remains (4.11). The upper and lateral boundary conditions for the solver attempt to mimic the unbounded conditions for the original physical system. Sponge layers are used to damp disturbances at the lateral boundaries, with periodicity assumed at the domain edges. The upper boundary uses a radiation condition at the top of the domain coupled with a sponge layer below.

In addition to the sponges, the solver also uses a weak horizontal and vertical fourth-order filter to help control numerical noise. The addition of these sponges and filters to the computational equations requires (4.9)-(4.11) to have two additional terms on the left hand side; namely

$$\alpha\varphi - S\varphi \quad ,$$

where $\alpha(x,z)$ applies the sponge layers, S is the filtering operator and φ is one of ψ_{zz}, ϕ or v.

3. Newton linearization

To simplify notation, suppose the disturbance variables are written in function space as

$$\mathbf{s} = \{\psi, \phi, v\}$$

and let the equations of motion be expressed in functional form as

$$F_\psi(\mathbf{s}) = 0, \quad F_\phi(\mathbf{s}) = 0, \quad \text{and} \quad F_v(\mathbf{s}) = 0, \tag{4.13}$$

where F_ψ, F_ϕ and F_v are the lefthand sides of (4.9)–(4.11), respectively, with the sponge layers and filter included. Defining

$$\mathbf{F}(\mathbf{s}) = \{F_\psi(\mathbf{s}), F_\phi(\mathbf{s}), F_v(\mathbf{s})\}$$

the goal of the steady solver is then to find $\mathbf{s}$ such that $\mathbf{F}(\mathbf{s}) = \mathbf{0}$.

In general, the nonlinear system (4.13) cannot be solved directly, and solutions are instead sought iteratively using Newton's method. Let the approximate solution at any given iteration be defined by $\mathbf{s}^n$, and suppose the goal is to find a displacement vector $\delta\mathbf{s} = \{\delta\psi, \delta\phi, \delta v\}$ so that

$$\mathbf{F}(\mathbf{s}^n + \delta\mathbf{s}) = 0\,. \tag{4.14}$$

In Newton's method, the nonlinear functional $\mathbf{F}(\mathbf{s}^n + \delta\mathbf{s})$ in (4.14) is linearized about $\mathbf{s}^n$ by assuming small $\delta\mathbf{s}$; that is,

$$\mathbf{F}(\mathbf{s}^n + \delta\mathbf{s}) \approx \mathbf{F}(\mathbf{s}^n) + \mathbf{J}_\mathbf{F}(\mathbf{s})[\delta\mathbf{s}] \tag{4.15}$$

where $\mathbf{J_F}(\mathbf{s})$ is a Jacobian-like operator[1] so that $\mathbf{J_F}(\mathbf{s})[\delta\mathbf{s}]$ is the linearized version of $\mathbf{F}(\mathbf{s}+\delta\mathbf{s}) - \mathbf{F}(\mathbf{s})$ (with terms quadratic in the small displacements neglected). Substituting into (4.14) gives the linearized system

$$\mathbf{J_F}(\mathbf{s})[\delta\mathbf{s}] = -\mathbf{F}(\mathbf{s}^n) \tag{4.17}$$

which can then be solved for the approximate displacement $\delta\mathbf{s}$. The solution is updated as

$$\mathbf{s}^{n+1} = \mathbf{s}^n + \delta\mathbf{s} \tag{4.18}$$

and the process is repeated until convergence [that is, until $\mathbf{F}(\mathbf{s}^{n+1})$ is below tolerance]. Note that if $\mathbf{s}^n$ is sufficiently close to the root, then the iteration (4.17) and (4.18) approaches the true solution quadratically.

Assuming $\mathbf{s} = \{\psi, \phi, v\}$ is the current iterate, then performing the Newton linearization on (4.9)-(4.11) gives

$$\begin{aligned}(1+\psi_q q_z)[(q_z)^2\delta\psi_{qqX} + 2q_z q_{xz}\delta\psi_{qq}] + [(q_z)^2\psi_{qqX} + 2q_z q_{xz}\psi_{qq}]q_z\delta\psi_q \\ + (q_x - \psi_X q_z)(q_z)^2\delta\psi_{qqq} - \psi_{qqq}(q_z)^3\delta\psi_X + \delta\phi_X + q_x\delta\phi_q \\ - \mathcal{R}^2 q_z\delta v_q + \alpha(q_z)^2\delta\psi_{qq} - S[(q_z)^2\delta\psi_{qq}] = -F_\psi(\mathbf{s})\end{aligned} \tag{4.19}$$

$$\begin{aligned}(1+\psi_q q_z)\delta\phi_X + \phi_X q_z\delta\psi_q + (q_x - \psi_X q_z)\delta\phi_q - \phi_q q_z\delta\psi_X - \delta\psi_X \\ - q_x\delta\psi_q + \alpha\delta\phi - S[\delta\phi] = -F_\phi(\mathbf{s})\end{aligned} \tag{4.20}$$

$$\begin{aligned}(1+\psi_q q_z)\delta v_X + v_X q_z\delta\psi_q + (q_x - \psi_X q_z)\delta v_q - v_q q_z\delta\psi_X \\ + q_z\delta\psi_q + \alpha\delta v - S[\delta v] = -F_v(\mathbf{s})\end{aligned} \tag{4.21}$$

---

[1]Technically speaking, the operator $\mathbf{J_F}(\mathbf{s})$ is functional derivative defined so that

$$\mathbf{J_F}(\mathbf{s})[\delta\mathbf{s}] = \lim_{h\to 0}\frac{\mathbf{F}(\mathbf{s}+h\,\delta\mathbf{s}) - \mathbf{F}(\mathbf{s})}{h} = \frac{d}{dh}\mathbf{F}(\mathbf{s}+h\,\delta\mathbf{s})\Big|_{h=0}, \tag{4.16}$$

but in practice this amounts to neglecting quadratic terms in $\mathbf{F}(\mathbf{s}+\delta\mathbf{s}) - \mathbf{F}(\mathbf{s})$.

which is a linear system for the displacement variables $\delta\psi$, $\delta\phi$, δv. Ultimately this system must be solved through discretization, as described in the following subsection. The lateral and upper boundary conditions for (4.19)–(4.21) are the same as those for the full system (see section 2). The lower boundaries are taken from (4.12), as described in section 5.

Ideally after each linear solve the variables would be updated by adding the full vector $\delta\mathbf{s}$, i.e., $\mathbf{s}^{n+1} = \mathbf{s}^n + \delta\mathbf{s}$. However, when the current iterate is far from the root of the nonlinear system, taking a full Newton step may overshoot the root and actually cause the magnitude of the residual [i.e., $\mathbf{F}(\mathbf{s}^n)$] to increase. To remedy this problem, the Newton linearization can be used with a line-search algorithm, which reduces the length of the displacement vector according to

$$\mathbf{s}^{n+1} = \mathbf{s}^n + \gamma\delta\mathbf{s} \quad , \tag{4.22}$$

where $\gamma \leq 1$ is the line-search coefficient. The coefficient is reduced iteratively from $\gamma = 1$ until the Armijo sufficient-decrease condition [57] is met, which states that the decrease in the functionals must be at least a fraction μ of the predicted linear decrease; specifically

$$||\mathbf{F}(\mathbf{s}^{n+1})|| \leq ||\mathbf{F}(\mathbf{s}^n) + \mu\gamma\mathbf{J}_\mathbf{F}(\mathbf{s}^n)\delta\mathbf{s}|| = (1 - \mu\gamma)||\mathbf{F}(\mathbf{s}^n)|| \tag{4.23}$$

where $0 \leq \mu \leq 1$ and $||\ ||$ indicates the l_2 vector norm. The fractional decrease parameter for this study is set to $\mu = 10^{-1}$. In the present case if a full Newton step ($\gamma = 1$) fails to meet the Armijo condition, the line search algorithm iterates by bisection according to $\gamma = 2^{-j}$, where j is the iteration number for the search.

The Newton-Armijo steps are repeated until the nonlinear functionals at all points in space have been reduced to a convergence tolerance of $|10^{-6}|$. It should be noted that once the root of the function is approached closely enough, the local

quadratic convergence of Newton's method is realized and the line-search algorithm is no longer necessary.

4. Discretization

The linearized system (4.19)–(4.21) is discretized on a collocated $nx \times nq$ grid, where nx and nq are the number of points in the x and q directions, respectively. The grid spacings Δx and Δq are constant throughout the domain.

For the most part, second-order centered differencing is used in the interior, with second-order one-sided differencing for (4.21) at the ground. However, two important exceptions are the ψ_{qqq} and $\delta\psi_{qqq}$ terms in (4.9) and (4.19), which cannot be evaluated accurately for the first interior grid points in q, that is, at $k = 2$ and $k = nq-1$ (where $k = 1$ is the lower boundary). As explained in appendix G, this problem is overcome for $k = 2$ by adding two extra variables to the lower boundary: the y-component of vorticity $\eta = u_z$ and the x-component of vorticity $\xi = -v_z$. The relevant equations are

$$(1+\psi_q q_z)\eta_X + (q_x - \psi_X q_z)\eta_q + \phi_X + \phi_q q_x + \mathcal{R}^2\xi + \alpha\eta - S[\eta] = 0 \quad \text{and} \tag{4.24}$$

$$(1+\psi_q q_z)\xi_X + (q_x - \psi_X q_z)\xi_q - \eta v_X - (\psi_q q_{xz} + \psi_{qX} q_z)\xi - \eta + \alpha\xi - S[\xi] = 0 \tag{4.25}$$

or in Newton update form

$$\begin{aligned}(1+\psi_q q_z)\delta\eta_X + \eta_X q_z\delta\psi_q + (q_x - \psi_X q_z)\delta\eta_q - \eta_q q_z\delta\psi_X + \delta\phi_X + q_x\delta\phi_q \\ + \mathcal{R}^2\delta\xi + \alpha\delta\eta - S[\delta\eta] = -F_\eta(\mathbf{s}) \quad \text{and}\end{aligned} \tag{4.26}$$

$$\begin{aligned}(1+\psi_q q_z)\delta\xi_X + \xi_X q_z\delta\psi_q + (q_x - \psi_X q_z)\delta\xi_q - \xi_q q_z\delta\psi_X - \eta\delta v_X - v_X\delta\eta \\ - (\psi_q q_{xz} + \psi_{qX} q_z)\delta\xi - \xi q_{xz}\delta\psi_q - \xi q_z\delta\psi_{qX} - \delta\eta + \alpha\delta\xi - S[\delta\xi] = -F_\xi(\mathbf{s})\end{aligned} \tag{4.27}$$

where F_η and F_ξ refer to (4.24) and (4.25), respectively. As illustrated by Fig. 23, the η and ξ equations are solved only for $k = 1$ and thus add negligible overhead to the

overall method. Further details of the $k = 2$ differencing are found in appendix G. At $k = nq - 1$ the method relies on η and $\delta\eta$ at the upper boundary, but these are easily obtained through the radiation condition, as explained in appendix H.

Once discretized, the linearized Newton system (4.19)–(4.21) with (4.26) and (4.27) becomes a large linear algebra problem for $\delta\mathbf{s} = (\delta\psi, \delta\phi, \delta v, \delta\eta, \delta\xi)$ as evaluated on the grid. Including $\delta\eta$ and $\delta\xi$ at the lower boundary and $\delta\eta$ at the upper boundary, the system can be written as

$$\mathbf{A}\,\delta\mathbf{s} = \mathbf{b} \tag{4.28}$$

where $\mathbf{A}$ is an $N \times N$ sparse matrix with $N = 3\,(nx)(nq) + 3\,nx$, and $\mathbf{b}$ includes both the righthand sides for the Newton problem as well as the lower boundary conditions (see section 5). The system is inverted using a direct method as implemented in matlab.

Finally, one further complication is the use of the radiation condition at upper boundary. The radiation condition is applied spectrally, implying that the relevant forward and inverse Fourier transforms must be embedded directly into the matrix $\mathbf{A}$ in (4.28). A brief outline of the method is given appendix H.

5. Initialization and boundary inflation

The initial guess for the Newton iteration is taken to be the linear solution about the constant N and U background state, but with the boundary conditions specified along the nonlinear terrain. The solution follows from (4.19)–(4.21) and (4.28), but with $F_\psi = F_\phi = F_v = 0$ and with the prior disturbance state set to $\psi = \phi = v = 0$. The only right hand side terms in (4.28) are then the lower boundary conditions (4.12), which are applied so as to produce no flow through the boundary at the end

of the linear solution; that is,

$$\delta\psi = -\epsilon h \quad \text{and} \quad \delta\phi = -\epsilon h$$

Subsequent Newton updates then set $\delta\psi = \delta\phi = 0$ at the boundary, so as to maintain (4.12). In the event that ϵ is small, the linear guess will be quite close to the nonlinear solution, and few Newton iterations will be necessary for convergence.

In the event that ϵ is large, nonlinear effects become signficant and the linear solution may be a poor guess for the fully nonlinear state, leading to slow convergence. This problem can be improved somewhat by modifying the lower boundary conditions (4.12) to slowly increase ϵ during the early iterations, thus gradually introducing nonlinear effects. The method involves replacing (4.12) with

$$\psi(q=0) = -\sigma^j \epsilon h \quad \text{and} \quad \phi(q=0) = -\sigma^j \epsilon h \tag{4.29}$$

where j is the iteration number and $\sigma^j \leq 1$ is a scaling factor that increases with j. The boundary conditions for the Newton updates are then modified to

$$\delta\psi(q=0) = -\Delta\sigma\epsilon h \quad \text{and} \quad \delta\phi(q=0) = -\Delta\sigma\epsilon h \tag{4.30}$$

where $\Delta\sigma$ is the change in σ from the previous iteration. In the present study

$$\sigma^j = \begin{cases} 0.5(1-\cos(\pi\frac{j}{n})), & \text{for } j \leq n \\ 1, & \text{for } j > n \end{cases} \tag{4.31}$$

where n is the total number of inflation steps. The value for n depends on the problem, with larger ϵ and $\mathcal{R}$ both requiring larger n.

During the inflation startup (i.e., for $j \leq n$) the line-search method described in section 3 is not applied. Once $j > n$ the Newton-Armijo steps begin as described in section 3.

6. Two-variable formulation

For the reference state with constant N and U both the total streamfunction $\Psi = z + \psi$ and total potential temperature $\Theta = z + \phi$ are constant along streamlines (cf., (4.2),(4.3)). Assuming both ψ and ϕ are zero upstream then implies that $\psi = \phi$ everywhere. This allows for the system developed in section B to be reduced to two variables, ψ and v, by replacing ϕ by ψ in (4.9) and $\delta\phi$ by $\delta\psi$ in (4.19). The result is a smaller system which is both faster and has a smaller memory footprint. All solutions in the following sections are taken from this two-variable solver.

C. Solver parameters and verifications

1. Computational parameters

All cases described here were performed for flow over a single nondimensional Gaussian ridge

$$h(x) = e^{-x^2} \tag{4.32}$$

with the peak centered in the domain. The domain size is varied in order to avoid reflections and account for the downstream dispersion and vertical decay of the wave field with increasing $\mathcal{R}$. For $0 \leq \mathcal{R} \leq 1$ the domain aspect ratio varies according to $nx = (275 + 100\mathcal{R})$ and $nq = (625 - 250\mathcal{R})$, while for $\mathcal{R} > 1$ the aspect ratio is held fixed with $nx = nq = 375$. All cases use grid spacing $\Delta x = \Delta q = \pi/25$. The horizontal sponge depth is held fixed at 2π on both edges of the grid, while the vertical sponge depth is varied so as to maintain an undamped domain of 8π (or four nonrotating wavelengths) in all cases.

The parameter space is mapped from $\mathcal{R} = 0$ to 2 in increments 0.1 and from $\mathcal{R} = 2$ to 4 in increments 0.2, while ϵ is increased from zero in increments of 0.02

until the critical overturning height ϵ_{cr} is approached. The critical overturning height is the value of ϵ at which the isentropes become vertical at some point in the domain, i.e.,

$$\min_{x,z}\{\Theta_z\}\Big|_{cr} = 0 \tag{4.33}$$

and above which the isentropes overturn and signal a dynamically unstable environment. Once a negative value is found for Θ_z, a bisection algorithm begins which performs seven bisections in ϵ, thus solving for ϵ_{cr} to within a tolerance of $0.02/2^7$.

2. Verifications

Figures 16b,d,f show the vertical velocity fields and isentropes from the Newton solver for cases with $\mathcal{R} = 0,\ 1$, and 2.4, respectively. The corresponding mountain height values are $\epsilon = 0.8,\ 0.8$ and 1.2. Figures 16a,c,e show analogous results using Long's solution for the nonrotating case and the time-dependent Boussinesq model of [58] for the rotating cases. The solutions compare quite well in each case and validate the formulation of the steady-state solver.

It should be noted that the steady solution can be obtained by time integration only if the wave fields are dynamically stable. The stability of the steady results is explored in chapter V.

D. Parameter maps, nonlinear behavior and example wave fields

The present section gives a number of examples to illustrate the dependence of the wave fields on ϵ and $\mathcal{R}$. Some important nonlinear effects are highlighted and the behavior of the waves in physical space is discussed.

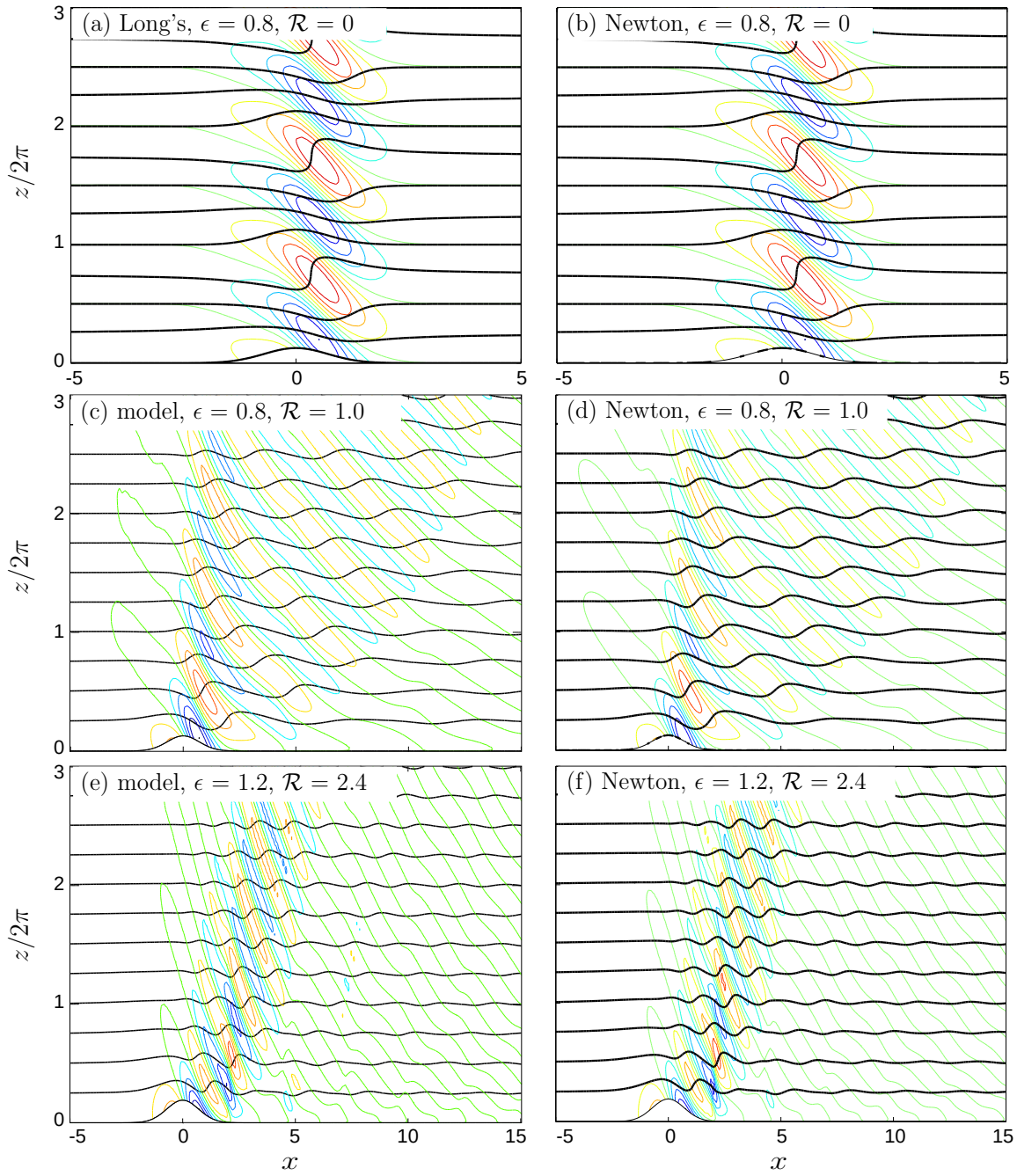

Fig. 16. Comparison of vertical velocity and isentropes from the steady-state solver (a,c,e) to those from Long's solution (b) and an equivalent time-dependent model (d,f),respectively, for three test cases. Row 1 compares the case for $\mathcal{R} = 0$ and $\epsilon = 0.80$. Row 2 shows comparisons for $\mathcal{R} = 1$ and $\epsilon = 0.8$. Row 3 shows comparisons for $\mathcal{R} = 2.4$ and $\epsilon = 1.2$.

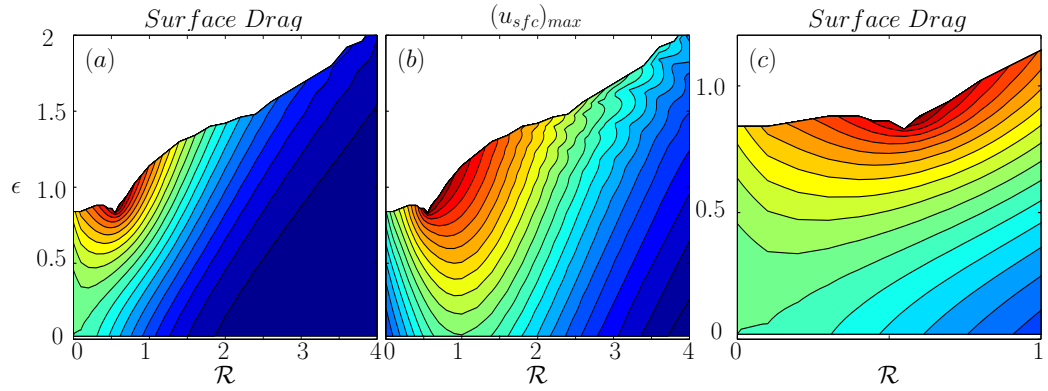

Fig. 17. Normalized surface drag and maximum surface winds as a function of ϵ and $\mathcal{R}$. The surface drag across the entire parameter space is shown in (a) while the maximum cross-ridge surface winds u are shown in (b). Surface drag across a small $\mathcal{R}$ portion of the parameter space are shown in (c). The contour inverval for all panels is 0.1, with the value at the origin being 1. The upper bound of the shading marks the critical overturning curve ϵ_{cr} as a function of $\mathcal{R}$.

1. Surface drag and critical mountain heights

Figure 17 shows the normalized surface drag and maximum cross-ridge surface wind as functions of ϵ and $\mathcal{R}$. The drags are normalized by the linear nonrotating prediction for the given value of ϵ, thus showing only the nonlinear trends as ϵ increases. Details fo the drag calculation are given in appendix I. The boundary of the shaded region in Figure 17 shows the critical mountain heights ϵ_{cr} at which wave overturning occurs.

In general, the critical overturning values ϵ_{cr} tend to increase with increasing $\mathcal{R}$, as the waves become increasingly dispersive and the disturbance vertical velocity decreases. The surface drag shown in Figure 17a tends to decrease with increasing $\mathcal{R}$ and increase with ϵ. As expected, minimum values are found for small ϵ and large $\mathcal{R}$ where the solution is approximately quasi-geostrophic and waves are removed from the system. Figure 17b shows that the maximum surface u increases rapidly with both $\mathcal{R}$ and ϵ before decreasing with increasing $\mathcal{R}$ for $\mathcal{R} \geq 1.0$.

The exceptions to the general trends seen in both the surface drag and overturn-

ing curve are highlighted in Figure 17c in which the small $\mathcal{R}$ portion of the parameter space is shown. As shown, the drag values actually increase with $\mathcal{R}$ for $\mathcal{R} \leq 0.55$ at large values of ϵ. The maximum values of the surface drag coincide with an area of decreased ϵ_{cr}. These features also coincide with the largest values of maximum surface velocity.

2. Steepening behavior

Figure 18 shows isentropes of the wave fields at overturning for increasing values of $\mathcal{R}$. The nonrotating case in Figure 18a shows the classic steepening aloft and just over the peak as seen in Long's solution. As $\mathcal{R}$ is increased the phase lines of the waves are tilted increasingly toward the horizontal and the region of greatest steepening is shifted lower and slightly downstream, as seen in Figures 18b–d for $\mathcal{R} = 0.2, 0.5$ and 1.0, respectively. Notice that as the region of greatest steepening descends the vertical gradient in the isentropes below increases, indicating a stronger surface u velocity as seen at intermediate $\mathcal{R}$ in Figure 17.

The descent and downstream shift of the steepening region continues for further increases in $\mathcal{R}$, but a new near surface feature also begins to have an effect on the wave pattern. Fig. 18d shows that for $\mathcal{R} = 1$ the region of steepened isentropes in the wave extends to the ground. This new surface feature was referred to as *lee cusping* by Trüb and Davies [47] and is completely absent at $\mathcal{R} = 0$. As $\mathcal{R}$ is increased the horizontal and vertical scales of the waves contract, resulting in surface steepening much closer to the peak and the appearance of wave overturning downstream along the surface (Figs. 18e,f). By $R = 4$ the scales contract to the point of marginal resolution, resulting in a jagged appearance for the wave pattern.

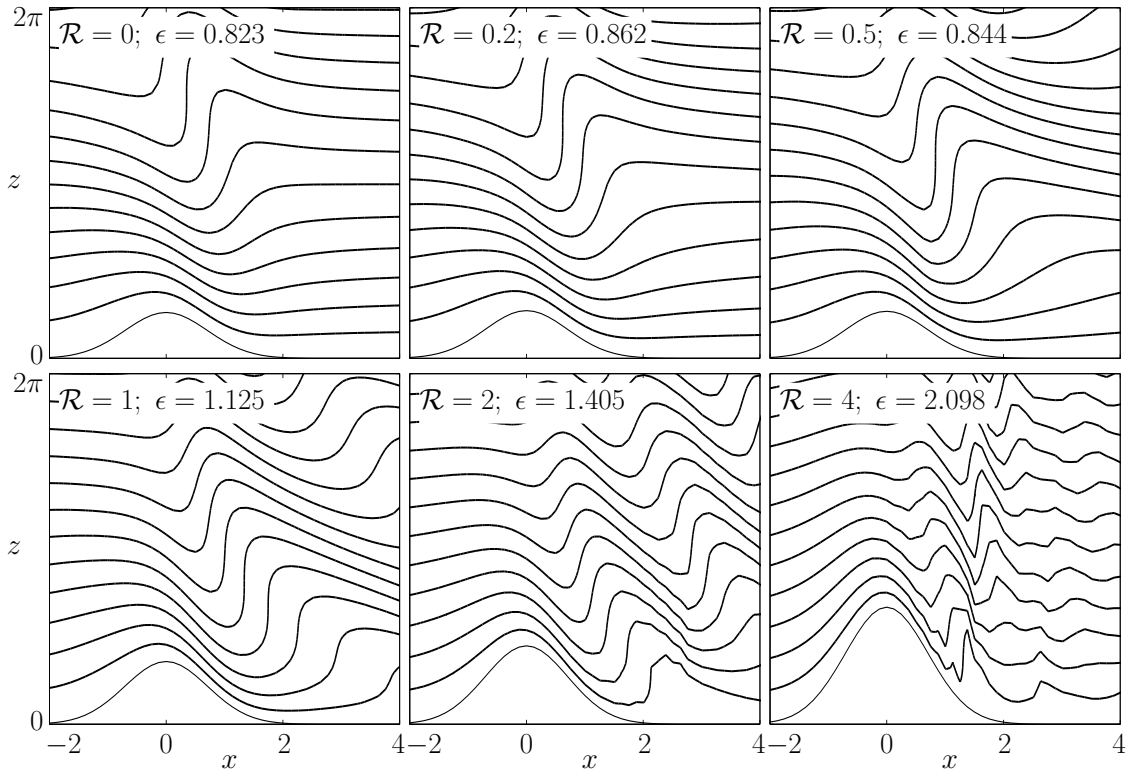

Fig. 18. Isentropes at ϵ_{cr} for various values of $\mathcal{R}$. Isentropes are shown at ϵ_{cr} for $\mathcal{R} = 0, 0.2, 0.5, 1.0, 2.0, 4.0$ in (a)–(f), respectively.

3. Lee cusping

The phenomenon of lee cusping was identified by Trüb and Davies [47] as a nonlinear feature of the scale collapse of the waves. Visual inspection showed that the cusping occured in response to asymmetries in the surface wave field, but further analysis was left to future work.

Figures 19a-c show the vorticity field and isentropes for the case $\mathcal{R} = 1.4$ at $\epsilon = 0.02, 0.64$ and 1.28, respectively. It is clear that as nonlinear effects increase, so too does the asymmetry between positive and negative vorticity anomalies in the surface vorticity field. The negative anamolies increase in amplitude and become elongated while the positive vorticity anamolies are contracted and significantly weakened. Asymmetries also exist in the corresponding u and v fields as seen in Figures 19d,e, respectively. Coincident with these growing asymmetries is the appearance of steepened isentropes in the near-surface wave pattern.

Some insight into the surface fields follows from (4.4) and (4.6) as considered along the nearly flat terrain downstream of the peak. Noting from (4.12) that for flat ground $\psi = \phi = 0$, the nondimensional versions of (4.4) and (4.6) at the boundary become

$$\eta_x \simeq \frac{\mathcal{R}^2\, v_z}{1+u} \quad \text{and} \quad v_x \simeq \frac{-u}{1+u} \tag{4.34}$$

First consider the small ϵ case, for which the u term in the denominators in (4.34) can be neglected. Over flat terrain the vorticity and u at the ground are closely correlated, with positive vorticity implying negative u and vice versa. Similarly, v_z is inversely correlated with v. Consideration of (4.34) then shows that for small ϵ the η and v fields at the ground oscillate roughly in quadrature with respect to distance. As shown in Fig. 19a, the result is a nearly symmetric pattern of positive and negative vorticity anomalies (with a weak decay downstream).

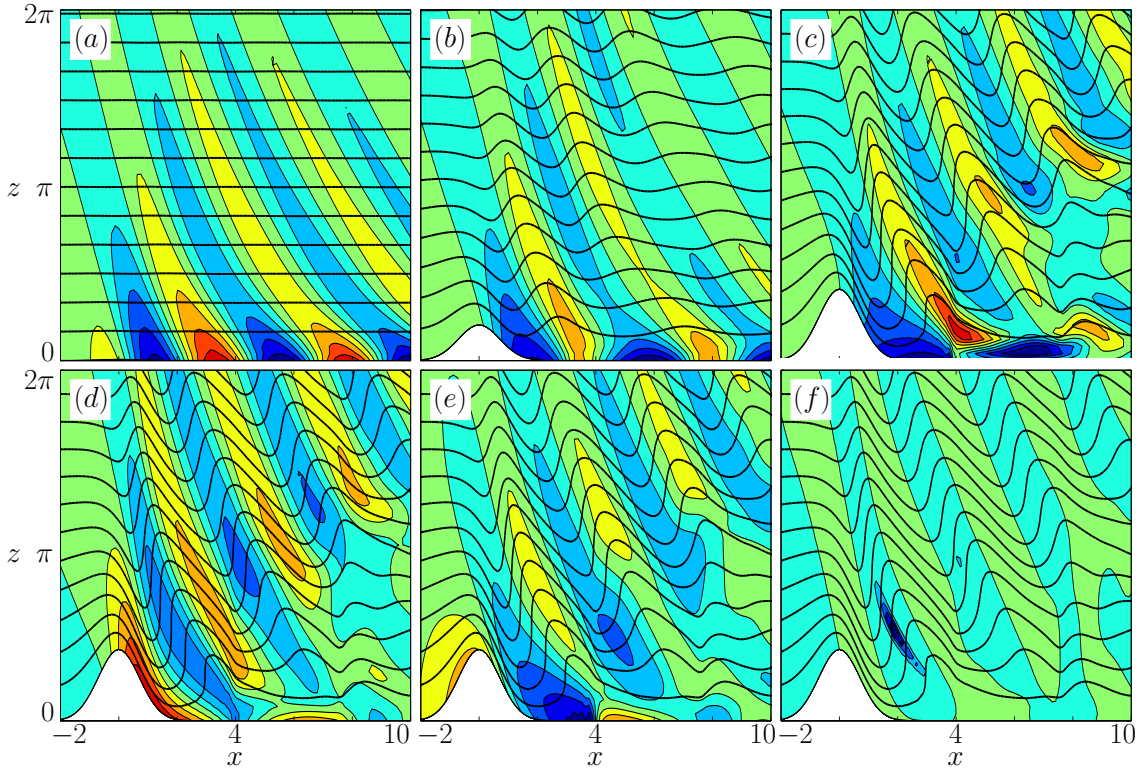

Fig. 19. Explanation of lee cusping as seen through ϵ and variable dependence. Vorticity and isentropes for $\mathcal{R} = 1.4$ and $\epsilon = 0.02, 0.64, 1.28$ are shown in (a)–(c), respectively. Velocity fields u and v and the slope of the isentropes are shown with isentropes in (d)–(f), respectively, for $\mathcal{R} = 1.4$ and $\epsilon = 1.28$.

As ϵ is increased the u term in the denominators of (4.34) becomes increasingly important. Positive values of u imply that the forcing terms in the numerators have less effect, i.e., the horizontal gradients in the η and v fields weaken, while negative values of u imply enhanced forcing terms and stronger horizontal gradients in η and v. This is easily understood from a Lagrangian perspective, since for $u < 0$ the fluid particles spend more time in the zone of the forcing. Since η is inversely correlated with u at the ground, (4.34) implies that negative vorticity anomalies are associated with weaker gradients and thus elongated while positive anomalies are associated with stronger gradients and thus contracted. Similar elongation and contraction occurs at the nodal points in v, as seen in Figure 19e.

The sharp gradients in the vorticity field imply enhanced convergence and divergence along the surface, leading to greater vertical motions and the cusping of the isentropes. However, note that while the lee cusping gives the appearance of wave overturning at the surface, the steepest isentropes are still found aloft and downstream of the peak. Figure 19f shows the slope of the isentropes Θ_x/Θ_z. The corridor of steepest isentropes lies along the phase lines and extends from just downstream and aloft of the peak down towards the surface. The relationship between the steepening aloft and the lee cusping at the ground is currently unknown, but it is suspected that the region of decreased ϵ_{cr} and maximum surface drag near $\mathcal{R} = 0.5$ in Figure 17b may occur in a transition zone in which the steepening effects of nonlinearity and lee cusping combine.

4. Wave fields as a function of ϵ and $\mathcal{R}$

Figure 20a shows various values of ϵ and $\mathcal{R}$ for which vertical velocity fields and isentropes are shown in Figure 21. The fields shown in Figure 21 are arranged similarly to Figure 20a in that the value of ϵ increases from bottom to top while $\mathcal{R}$ increases

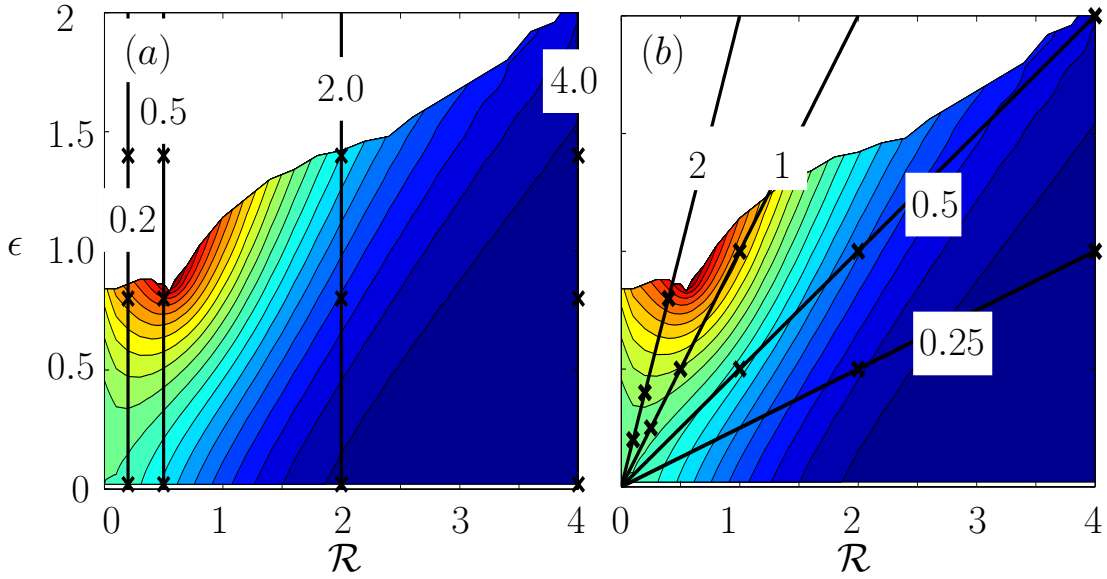

Fig. 20. Key for example cases shown in Figures 21 and 22. The points in used in Figure 21 are shown by crosses along lines of constant $\mathcal{R}$ in (a). The points used in Figure 22 are shown by crosses along lines of constant $\epsilon/\mathcal{R}$ in (b). The values of $\mathcal{R}$ and $\epsilon/\mathcal{R}$ are indicated along each line.

from left to right. The contour interval is set by the leftmost panel in each row and scales with ϵ. Row 3 highlights the nearly linear wave regime with $\epsilon = 0.02$. The largest amplitudes are found in the nonrotating case and decrease with increasing $\mathcal{R}$ as the waves become increasingly dispersive. Figures 21j–l show the scale contraction and associated decreased vertical velocity of the waves. By $\mathcal{R} = 4$ the solution is nearly quasi-geostrophic with only minimal waves downstream.

Row 2 shows the case with $\epsilon = 0.80$, quite close to the critical overturning value for both the nonrotating and $\mathcal{R} = 0.5$ cases shown in Figures 21e,f, respectively. In fact the amplitude of the downward motion along the lee slope is greater for the rotating case as it is enhanced by the lower steepening region. The same scale contraction and decreased vertical velocity as seen in the linear case are seen for $\mathcal{R} = 2, 4$ in Figures 21g,h, respectively. However, the larger value of ϵ maintains the nonlinear wave generation even at large $\mathcal{R}$. This becomes especially true in Row 1

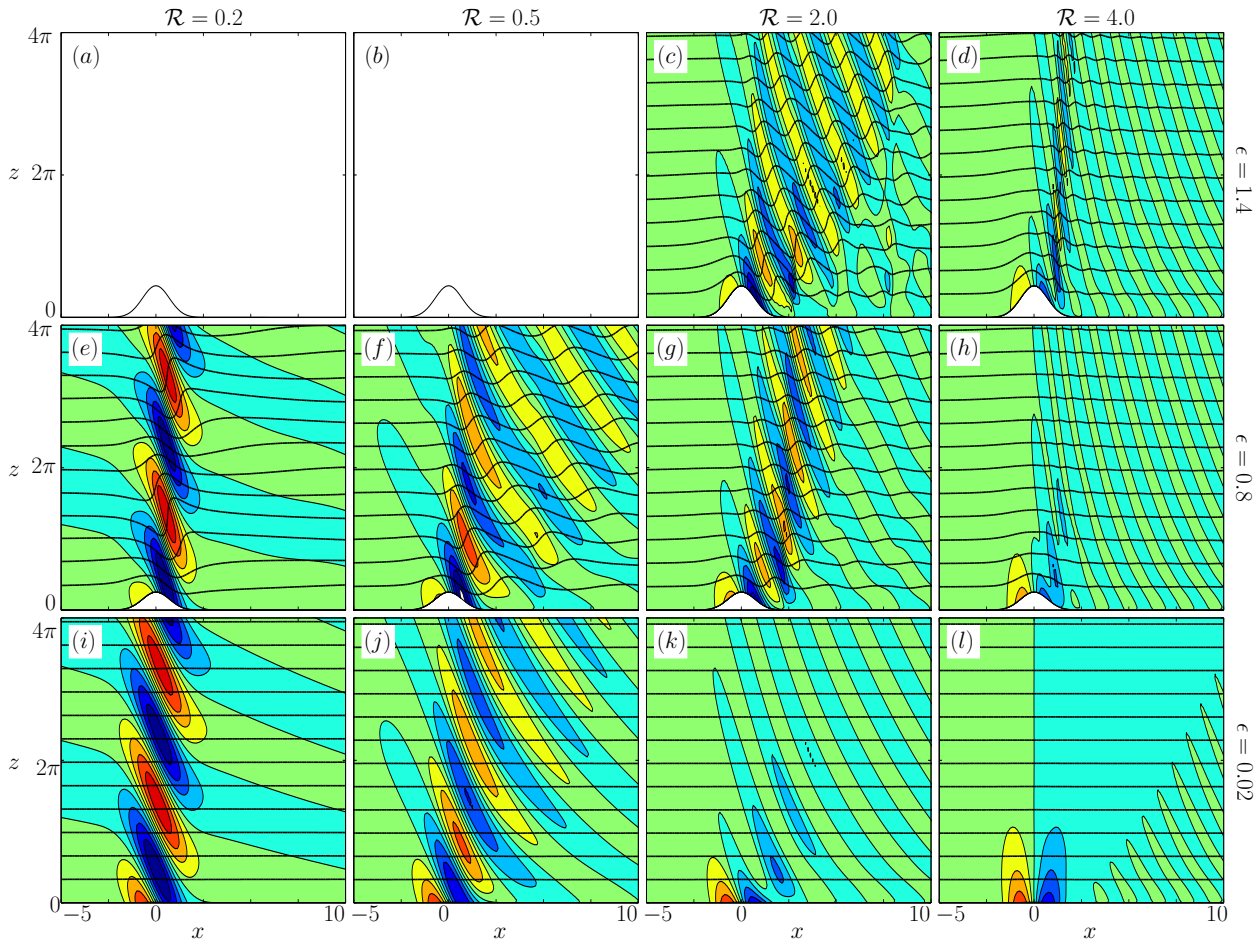

Fig. 21. Vertical velocity and isentropes at various locations in nondimensional parameter space. The rotational parameter varies as $\mathcal{R} = 0, 0.5, 2.0, 4.0$ for Columns 1–4, respectively, while the mountain height varies as $\epsilon = 0.02, 0.80, 1.40$ for Rows 1–3, repsectively. The contour interval is set by the leftmost panel in each row and scales with ϵ. The zero contour is marked by a transition from green to blue.

for $\epsilon = 1.4$ which is close to the critical overturning value for $\mathcal{R} = 2$ seen in Figure 21c. The nonlinear waves are still prominent for $\mathcal{R} = 4$ seen in Figure 21d.

It should be noted that since the waves are becoming increasingly inertial with increasing $\mathcal{R}$ the amplitude of the u velocity field does not dissipate as quickly as the vertical velocity field shown here.

Table III. Dimensional terrain parameters and corresponding nondimensional parameters for Figure 22. The Coriolis parameter and static stability are held fixed at $f = 10^{-4}s^{-1}$ and $N = 0.01s^{-1}$, respectively, while U varies as specified in the figure.

$\epsilon/\mathcal{R}$	$h(m)$	$L(km)$	ϵ	$\mathcal{R}$
2	400	20	0.2–0.8	0.1–0.4
1	500	50	0.25–1	0.25–1
0.5	1000	200	0.5–2	1–4
0.25	1000	400	0.5–2	2–8

5. Examples in physical space

Nondimensional analysis is relatively simple given two control parameters ϵ and $\mathcal{R}$, but it gives little intuition into the physical parameter dependence. As such, slices of the parameter space of slope $\epsilon/\mathcal{R}$ are taken as shown in Figure 20b and dimensionalized as described in Table III for background velocity values $U = 5, 10$, and $20ms^{-1}$. Figure 22 shows the vertical velocity and isentropes as a function of the background velocity U at points along the $\epsilon/\mathcal{R}$ curves. Once again the contour interval is set by the leftmost panel in each row, but here the amplitude scales with $1/L$ where L is given in Table III. Also note that since the dimensional vertical scale is dimensionalized according to $z^* = \frac{U}{N}z$ that the vertical scale of the waves decreases with the

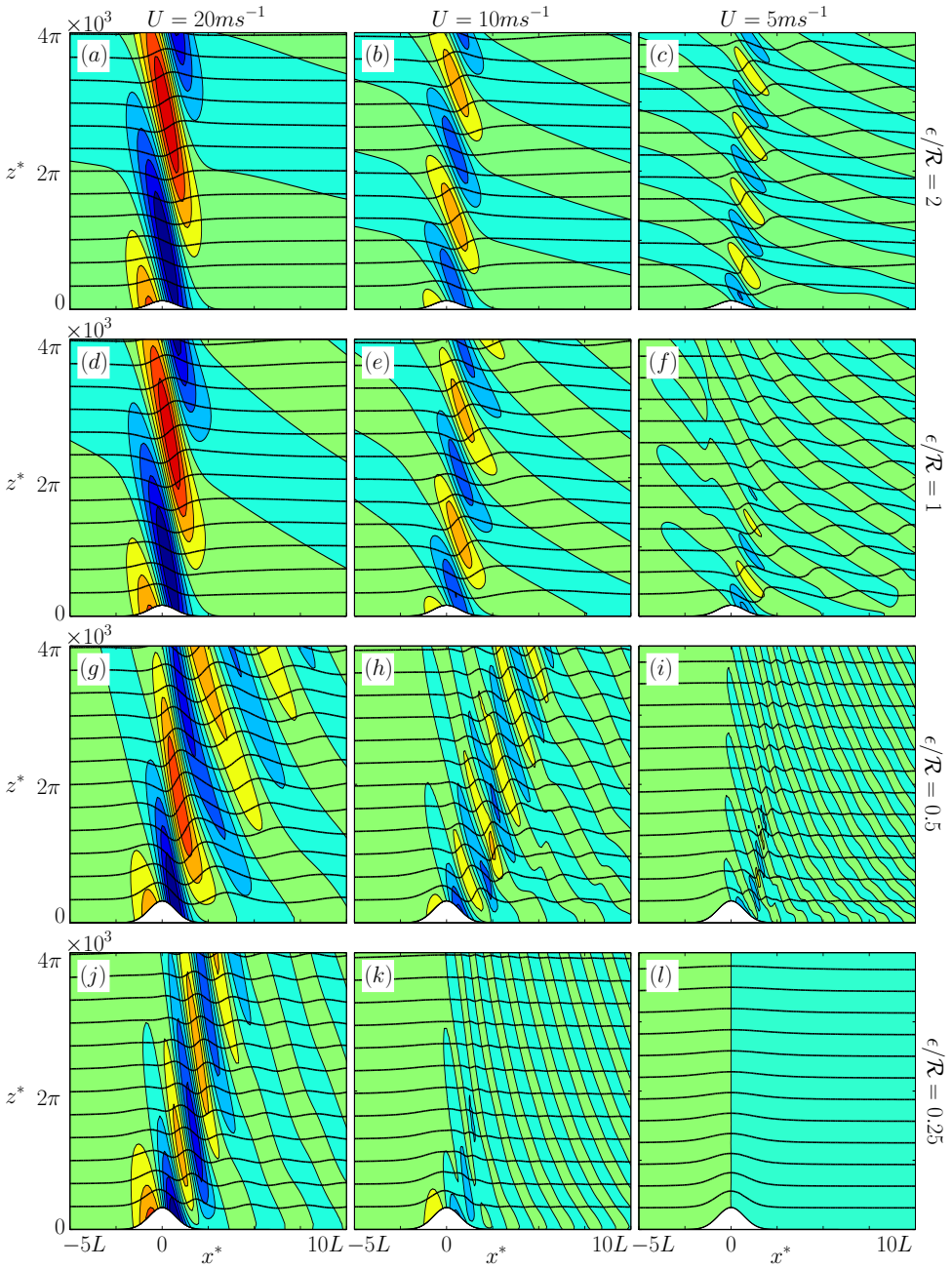

Fig. 22. Vertical velocity and isentropes at various locations in physical parameter space. The background velocity U varies as $U = 20, 10, 5ms^{-1}$ for Columns 1–3, respectively, while the ratio $\epsilon/\mathcal{R}$ varies as $\epsilon/\mathcal{R} = 2, 1, 0.5, 0.25$ for Rows 1–4, repsectively. The contour interval is set by the leftmost panel in each row and scales with $1/L$, where L is found in Table III. The zero contour is marked by a transition from green to blue.

value of U.

Row 1 shows the case with $\epsilon/\mathcal{R} = 2$, which is restricted to small values of $\mathcal{R}$. The largest amplitude vertical velocity is found for the case with $U = 20ms^{-1}$ and decreases with decreasing U. However, analysis of the isentropes shows that while the vertical scale and amplitude of the waves is contracting, the wave steepness is increasing to the point of overturning by $U = 5ms^{-1}$ as seen in Figure 22c.

Rows 2 and 3 show the cases with $\epsilon/\mathcal{R} = 1, 0.5$, respectively. Once again the largest amplitudes are found for $U = 20ms^{-1}$ and decrease with decreasing U. The increased steepening of the insentropes with decreasing U also continues. These cases highlight the fact that changing the background U field does not just change the amplitude or wave steepness, it changes the regime completely. As U is decreased the effects of rotation are enhanced, causing the waves to become increasingly dispersive and decreasing the vertical velocity. Also notice that horizontal scale of the nonlinear waves is severely contracted when rotational effects are large, as seen in Figures 22h,i.

Row 4 shows the case with $\epsilon/\mathcal{R} = 0.25$, which spans much of the rotational parameter space. The waves here transition from the weakly nonlinear regime seen for $U = 20ms^{-1}$ in Figure 22j to the linear regime where the solution is approximately quasi-geostrophic for $U = 5ms^{-1}$ as seen in Figure 22l.

E. Vertically-varying background states

In order to include vertical variations in U and N a nonzero background state must be developed as an input to the initial linear solve. The background state will define the variations in U and N using vertical profiles in ψ and ϕ and will be denoted by

$$\mathbf{s}^{(0)} = \{\psi^{(0)}, \phi^{(0)}, v^{(0)}, \eta^{(0)} = \psi^{(0)}{}_{qq}(q_z)^2, \xi^{(0)}\} \tag{4.35}$$

where it is assumed that the background is uniform in x and, thus, $\xi^{(0)} = v^{(0)} = 0$.

The startup and Newton iterations will now solve for the disturbance to this new background state. As such, the sponge layers and spatial filter must be modified as

$$\alpha(\mathbf{s} - \mathbf{s}^{(0)}) \quad \text{and} \quad S[\mathbf{s} - \mathbf{s}^{(0)}] \tag{4.36}$$

to damp only the disturbance part of the solution. Note that this only affects the right hand side of the equations since these terms already apply to the disturbance in the linearized equations. In a similar manner the lateral boundary conditions on the total fields would change to

$$\boldsymbol{\nabla}\psi = \boldsymbol{\nabla}\psi^{(0)}; \quad v = v^{(0)}; \quad \phi = \phi^{(0)}; \quad \eta = \eta^{(0)}; \tag{4.37}$$

but the current disturbance lateral boundary conditions remain valid.

The lower boundary conditions on both ψ and ϕ must be modified to include the new background state. The total conditions on Ψ and Φ for the quasi-linear solve become

$$\Psi = z + \psi = z + \psi^{(0)} + \delta\psi \tag{4.38}$$

and

$$\Phi = z + \phi = z + \phi^{(0)} + \delta\phi \tag{4.39}$$

such that the disturbance lower boundary conditions must be

$$\delta\psi(q = 0) = -\epsilon h - \psi^{(0)} \tag{4.40}$$

and

$$\delta\phi(q = 0) = -\epsilon h - \phi^{(0)} \tag{4.41}$$

in order for the lower boundary to remain both a streamline and isentropic surface. Subsequent Newton solves still use $\delta\psi = 0$ and $\delta\phi = 0$.

The addition of a sheared background U necessitates the addition of latitudinally varying pressure gradient and buoyancy terms in order to maintain geostrophic and thermal wind balance. Dimensionally, the appropriate geostrophic balance is

$$P^{*(0)}{}_{y^*} = -f\psi^{*(0)}{}_{z^*} \tag{4.42}$$

where P^* is the pressure and $U = \psi^{*(0)}{}_{z^*}$. This requires a new term on the left-hand side of the meridional wind equation (4.11). After nondimensionalization and terrain transformation the new term is

$$-\psi^{(0)}{}_{q} q_z \tag{4.43}$$

which is a constant with respect to the disturbance variables and, thus, only shows up on the right hand side of the linearized equation (4.21). In line with the geostrophic balance, the appropriate thermal wind balance is

$$P^{*(0)}{}_{y^*z^*} = b^{*(0)}{}_{y^*} = -f\psi^{*(0)}{}_{z^*z^*} = -f\eta^{*(0)} \tag{4.44}$$

which leads to a new latitudinal advection term on the left hand side of the ϕ equation (4.10). After nondimensionalization and terrain transformation the new term is

$$-\mathcal{R}^2\eta^{(0)}v \tag{4.45}$$

However, in this case the term is not constant with respect to the disturbance variables and requires an extra term

$$-\mathcal{R}^2\eta^{(0)}\delta v \tag{4.46}$$

on the left hand side of the linearized equation (4.20). Lastly, for consistency with

the the new term in the v equation (4.43), a constant baroclinic term

$$\eta^{(0)} \tag{4.47}$$

must be added to the left hand side of the ξ equation (4.25), but it does not affect the left hand side of the linearized equation (4.27).

The radiation condition along the uppper boundary must also be modified to account for the varying background state by modifying the dimensional vertical wavenumber m wherever N and U appear. Nondimensionally, the changes follow according to

$$m^2 = \frac{i(1+\phi^{(0)}{}_q q_z)^{1/2} k (i(1+\phi^{(0)}{}_q q_z)^{1/2} k + \alpha')}{(i(1+\psi^{(0)}{}_q q_z)k + \alpha')^2 + \mathcal{R}^2}, \tag{4.48}$$

compare with (4.53).

F. Summary

A Newton solver is developed for the problem of steady, 2D flow past finite-amplitude topography on an f-plane. The solver is valid for arbitrary Rossby number as well as for problems with vertically varying background states. In this respect, the calculations effectively extend Long's nonrotating solution to both the rotating problem and to nonconstant background flows.

Calculations were presented for the problem of flow with constant background wind and stability. The nondimensional parameter space is then governed by two parameters: the nondimensional mountain height $\epsilon = Nh_0/U$ and the inverse Rossby number $\mathcal{R} = fL/U$. The critical height ϵ_{cr} at which wave overturning occurs was mapped as a function of $\mathcal{R}$, and surface drags were computed as a function of $\mathcal{R}$ and ϵ. Example flows were computed showing the variations in the wave field as ϵ and $\mathcal{R}$ are varied.

Mapping of the parameter space reveals that the wave fields steepen with increasing ϵ, while increasing $\mathcal{R}$ leads to greater dispersion, which decreases steepening for a given ϵ. The result is that the critical height for overturning generally increases as $\mathcal{R}$ increases. An exception occurs at intermediate $\mathcal{R}$ (specifically $\mathcal{R} \sim 0.5$) where ϵ_{cr} decreases, coinciding with the maximum surface drag and winds. Note that even at large $\mathcal{R}$ wave overturning occurs if ϵ is sufficiently large.

Examination of the wave fields near overturning reveals the onset of surface cusping at intermediate values of $\mathcal{R}$. Analysis of the wave fields shows that the cusping results from nonlinear asymmetries in the surface vorticity field, which increase the surface convergence as ϵ increases. Maximum steepening of the waves is still found to occur aloft, although cusping at the surface may play an indirect role in helping to steepen the waves.

Example calculations were presented to explore the changes in the dimensional wave fields as the background wind U is decreased. The variations are shown to depend on the parameter combination $\epsilon/\mathcal{R} = Nh_0/fL$. For large $\epsilon/\mathcal{R}$ the waves steepen with minimal dispersion, while for small $\epsilon/\mathcal{R}$ the waves pass through dispersive states with minimal steepening before reaching the quasi-geostrophic regime. For intermediate $\epsilon/\mathcal{R}$ the waves both steepen and disperse before eventually reaching overturning. Nonlinear waves are found even at large $\mathcal{R}$ when ϵ is sufficiently large, but the horizontal and vertical scales of the waves are significantly contracted. In all cases the dimensional vertical velocities are largest for large U.

For the analysis of steady wave fields, the solver was found to have a number of advantages over time integrations to steady state. In particular:

- The solver is found to be 10-50 times faster than a time integration for much of the parameter space

- The solver applies a radiation condition to the upper boundary which is valid even for flows with rotation; allowing for the use of smaller domains and an accurate representation of the quasi-geostrophic regime
- The solver is found to be robust across the parameter space and easily adapted to allow for stability analyses of the resulting steady solutions

The ability to perform stability analyses of the steady solutions is of particular interest for the companion study which will be presented in chapter V.

G. Appendix: Differencing the ψ_{qqq} terms at the boundary

A complication of the current solver formulation is that the ψ_{qqq} and $\delta\psi_{qqq}$ terms in (4.9) and (4.19) cannot be accurately evaluated at $k = 2$. The problem ultimately stems from the fact that ψ_{qq} cannot be evaluated at $k = 1$, implying that ψ_{qqq} is problematic one level up. As described in section 4, the solution to this problem is to add the equations (4.24)–(4.27) to solve for η and ξ at the boundary. The idea is that ψ_{qq} is obtained at $k = 1$ not by differencing ψ, but rather by solving the η equation (4.24). Once η at $k = 1$ is known, the ψ_{qqq} term at $k = 2$ can be evaluated as (cf. Fig. 23)

$$\left.\frac{\partial^3\psi}{\partial q^3}\right|_{i,2} = \frac{\psi_{i,4} - 2\psi_{i,3} + \psi_{i,2}}{2(\Delta q)^3} - \frac{\eta_{i,1}(q_z)^{-2}}{2\Delta q} + O((\Delta q)^2)$$

and similarly for $\delta\psi_{qqq}$. Further, if the η_q term in (4.24) is differenced as

$$\left.\frac{\partial\eta}{\partial q}\right|_{i,1} = \frac{-\psi_{i,4} + 6\psi_{i,3} - 9\psi_{i,2} + 4\psi_{i,1}}{2(\Delta q)^3}(q_z)^2 - \frac{3\eta_{i,1}}{2\Delta q} + O((\Delta q)^2)$$

then (4.24) can be implemented without any reference to η in the interior, implying that η and $\delta\eta$ need only be implemented at $k = 1$.

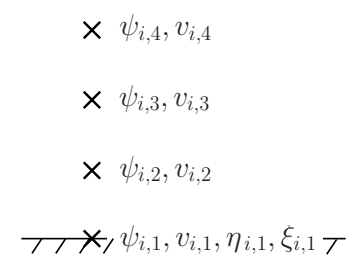

Fig. 23. Configuration of the ψ, v, η and ξ points near the boundary.

The need for (4.25) and (4.27) at the boundary stems from the planetary vorticity term in the η equation, which in principle depends on v_q. Differencing (4.11) shows that v_q in turn depends on ψ_{qq}, which makes v_q at the boundary problematic. Again, the solution is to obtain v_q not by differencing the v field, but rather by solving (4.25) at the boundary to obtain ξ. And as with (4.24), the ξ equation can be solved without referencing ξ in the interior. Including ξ in the system also allows the v_q term in (4.11) to be evaluated at $k = 1$ (although this term is needed only during initialization—see section B5).

H. Appendix: The radiation condition

To implement the radiation condition, a series of horizontal Fourier transforms and inverses must be embedded into the operator $\mathbf{A}$ in (4.28). Consider the discretized variable $\delta\psi_{n,k}$ on the grid and let the horizontal array of points to be transformed at vertical grid level k be denoted by $\delta\boldsymbol{\psi}_k$. Let the corresponding array of discrete Fourier transforms for $\delta\boldsymbol{\psi}_k$ be $\delta\hat{\boldsymbol{\psi}}_k$. Suppose the number of points to be transformed is M and let the j^{th} wavenumber on the grid be denoted by κ_j, with $1 \le j \le M$. The discrete transform of $\delta\boldsymbol{\psi}_k$ can then be written in matrix form as

$$\delta\hat{\boldsymbol{\psi}}_k = \boldsymbol{\chi}\,\delta\boldsymbol{\psi}_k \tag{4.49}$$

where $\boldsymbol{\chi}$ is the $M \times M$ matrix operator with elements

$$\chi_{j,n} = \exp(-i\kappa_j(n-1)\Delta x) \tag{4.50}$$

implying that the j^{th} row of (4.49) is the transform of $\delta\boldsymbol{\psi}_k$ for wavenumber κ_j.

Given the Fourier transforms, the radiation condition is expressed using trapezoidal vertical differencing as

$$\delta\hat{\psi}_{j,nq} \;=\; \frac{q_z + im\Delta q/2}{q_z - im\Delta q/2}\,\delta\hat{\psi}_{j,nq-1} \;=\; \lambda_j\,\delta\hat{\psi}_{j,nq-1} \tag{4.51}$$

where the vertical wavenumber m is a function of κ_j and is chosen to give either upward energy propagation (for $|\,\kappa_j\,| > \mathcal{R}$) or else vertical decay ($|\,\kappa_j\,| \le \mathcal{R}$) in the linear limit (see below). The condition is imposed in matrix form by defining the diagonal matrix $\boldsymbol{\Lambda}$ to be

$$\Lambda_{j,n} = \lambda_j\,\delta_{jn}$$

where δ_{jn} is the Kronecker delta, so that $\delta\hat{\boldsymbol{\psi}}_{nq} = \boldsymbol{\Lambda}\,\delta\hat{\boldsymbol{\psi}}_{nq-1}$. With these definitions, the full forward transform (4.49), radiation condition (4.51), and inverse transform steps can then be written as a single matrix operation as

$$\delta\boldsymbol{\psi}_{nq} = \frac{1}{M}\,\boldsymbol{\chi}^*\boldsymbol{\Lambda}\boldsymbol{\chi}\;\delta\boldsymbol{\psi}_{nq-1} \tag{4.52}$$

where the discrete inverse transform operator $\boldsymbol{\chi}^*$ is the conjugate transpose of (4.50).

The n^{th} row of (4.52) shows that under the radiation condition, the value of $\delta\psi_{n,nq}$ at a given point on the upper boundary is simply a linear combination of the values one level below (and similarly for $\delta\phi$ and δv). The condition is then imposed in (4.28) by simply embedding the n^{th} row of the matrix operator $(1/M)\,\boldsymbol{\chi}^*\boldsymbol{\Lambda}\boldsymbol{\chi}$ in (4.52) into the appropriate row of $\mathbf{A}$ in (4.28).

In the present study the wavenumber m used in (4.51) is modified to include the

upper sponge layer and horizontal filter. The relevant dispersion relation is then

$$m^2 = \frac{i\kappa\,(i\kappa + \alpha')}{(i\kappa + \alpha')^2 + \mathcal{R}^2} \tag{4.53}$$

where $\alpha' = \alpha + \gamma\kappa^4$, with α being the sponge coefficient and γ the filter coefficient. The branch of the square root is chosen so that $\mathrm{Im}(m) > 0$, thus guaranteeing vertical decay. The limit of small α' shows that this branch choice matches the standard choice when m^2 is real. As in [59], somewhat better results are achieved at short wavelengths by replacing κ in (4.53) by its discretized counterpart for centered differencing.

Finally, as discussed in section 4, the vertical differencing at grid level $k = nq - 1$ relies on η at the upper boundary in addition to ψ, ϕ and v. Under the radiation condition, η is obtained spectrally from ψ using

$$\delta\hat{\eta}_{j,nq} = -m^2\,\delta\hat{\psi}_{j,nq}$$

with the forward and inverse transforms then embedded in the matrix $\boldsymbol{A}$ as described above.

I. Appendix: Diagnostic surface pressure drag

Calculation of the surface pressure drag requires a diagnostic calculation of the surface pressure. This is derived from the hydrostatic pressure-velocity system

$$(U + u^*){u^*}_{x^*} + w^*{u^*}_{z^*} = -{p^*}_{x^*} + fv^* \tag{4.54}$$

$$(U + u^*){v^*}_{x^*} + w^*{v^*}_{z^*} = -f(u^* - {u^{*(0)}}) \tag{4.55}$$

$${p^*}_{z^*} = b^* \tag{4.56}$$

$$(U + u^*){b^*}_{x^*} + w^*{b^*}_{z^*} - f{u^{*(0)}}_{z^*}v^* + N^2w^* = 0 \tag{4.57}$$

$${u^*}_{x^*} + {w^*}_{z^*} = 0 \tag{4.58}$$

where the background state is indicated by the superscript (0) and is balanced according to

$$p^{*(0)}{}_{y^*} = -fu^{*(0)}; \quad p^{*(0)}{}_{z^*} = b^{*(0)}; \quad b^{*(0)}{}_{y^*} = -fu^{*(0)}{}_{z^*} \tag{4.59}$$

Combining (4.54) and (4.56), and noting that the disturbance pressure scales according to $p^* = U^2 P$ leads to the nondimensional equation

$$\left[(1+\psi_z)\frac{\partial}{\partial x} - \psi_x \frac{\partial}{\partial z}\right]\left(\frac{(1+\psi_z)^2}{2} + P\right) = \mathcal{R}^2 v(1+\psi_z) - \psi_x(\phi - \phi^{(0)}) \tag{4.60}$$

Transforming to terrain following coordinates and working out the analytic derivatives using the known value of ψ at the lower boundary leads to

$$\frac{\partial}{\partial X}\left(\frac{(1+\psi_q q_z)^2}{2} + P\right) = \mathcal{R}^2 v + \epsilon h_x(\phi - \phi^{(0)}) \tag{4.61}$$

Lastly, the disturbance pressure decays to zero for $|\,x\,| \to \infty$ which allows for integration to obtain the final surface pressure equation

$$P = \frac{(1+\psi_q{}^{(0)} q_z)^2}{2} - \frac{(1+\psi_q q_z)^2}{2} + \int_{-\infty}^{X} \mathcal{R}^2 v + \epsilon h_x(\phi - \phi^{(0)}) dX' \tag{4.62}$$

The surface pressure drag is then given by

$$D = \int_{-\infty}^{\infty} P h_x dx \tag{4.63}$$

In practice both the surface pressure and drag are integrated using trapezoidal differencing. All drag values are normalized by the predicted linear nonrotating drag value and scaled by ϵ according to

$$D_N = \frac{D}{(\frac{\epsilon}{\epsilon_l} D_l)} \tag{4.64}$$

where the subscripts N and l indicate *Normalized* and *linear*, respectively. The absolute maximum surface winds u and v are normalized in a similar manner.

CHAPTER V

RESONANT WAVE-WAVE INSTABILITY IN ROTATING MOUNTAIN WAVES

A. Resonant triad instability in hydrostatic nonrotating mountain waves

The study of resonant instability in mountain waves has been, thus far, limited to a single study by Lee et. al. [13]. Steady solutions for hydrostatic nonrotating flow over two Gaussian peaks were found using Long's solution. A linear stability analysis was then performed based on disturbances about the steady solution to identify any unstable modes. Groups of unstable modes were found; each with a cellular structure focused over and between the peaks and near planar waves in the far field as seen in Figure 24. The onset of the instability was found to occur at mountain heights ($\epsilon = Nh_0/U$) much less than those required for steady wave overturning, with growth rates increasing with ϵ.

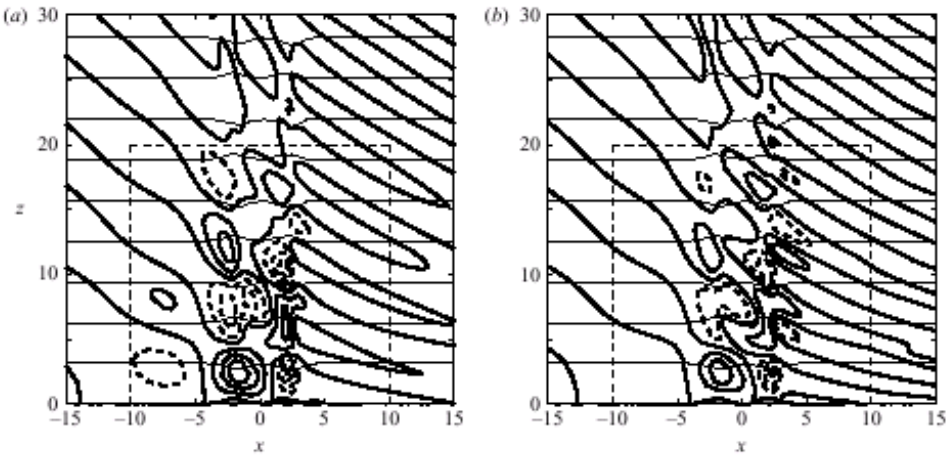

Fig. 24. Streamfunction (a) and buoyancy (b) fields of the most unstable mode and streamlines of the steady-state solution for hydrostatic nonrotating ($\mathcal{R} = 0$) flow over a two-peak terrain profile with $\epsilon = 0.5$. The contour interval is 0.06.

The causality of the spatial structure was investigated through a Fourier decom-

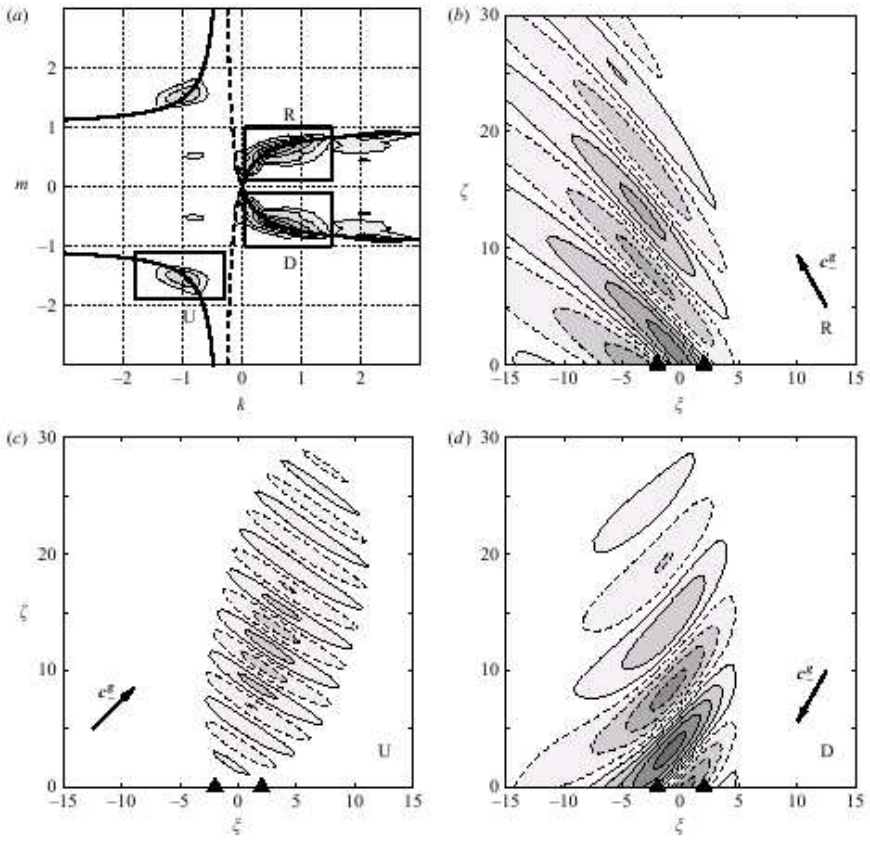

Fig. 25. Fourier decomposition of the streamfunction of the most unstable wave mode. The Fourier spectrum is shown in (a) with darker shading indicating larger amplitudes. The solid (dashed) lines are the dispersion curves for slow (fast) waves with frequency matching that of the unstable mode. (b)–(d) highlight the upward, downward, and reflected wave modes which compose the unstable structure.

position of the disturbance streamfunction of the most unstable wave mode. This, along with the dispersion relation for linear gravity waves in the system, allowed for identification of three gravity wave modes which compose the majority of the unstable mode, as seen in Figure 25. The unstable mode was found to be a combination of a gravity mode which propagates energy upward and one which propagates energy downward coupled with its upward reflection off the surface. The summation of the downward propagating mode and its reflection is sufficient to explain the cellular interference pattern over the terrain in the unstable mode structure.

Finally, to identify the energy source of the upward and downward propagating gravity modes, a Fourier decomposition of the steady u and w fields was performed. Figure 26a shows the spectral peaks of the steady solution; the highest amplitude spectral peak of w is used to identify the steady wavenumber vector. Figure 26b shows the Fourier spectrum of the unstable mode overlayed with wavenumber vectors of the steady solution and upward and downward propagating wave modes. The wavenumber vectors are shown to form a resonant triad according to

$$\mathbf{k}^U + \mathbf{k}^S = \mathbf{k}^D \quad \omega(\mathbf{k}^U) + \omega(\mathbf{k}^S) = \omega(\mathbf{k}^D) \tag{5.1}$$

where k is the wavenumber vector, ω is the frequency, and the superscripts U, S, D represent Up, $Steady$, and $Down$, respectively. Thus, when an upward propagating mode is excited in the steady flow the fourier modes will be multiplied and the wavenumber vectors will be summed to introduce a downward propagating mode, which will then interact with the steady flow to reinforce the upward mode. It is suspected that the aformentioned reflected mode acts as a large energy sink from the system and limits the growth rates of the instability.

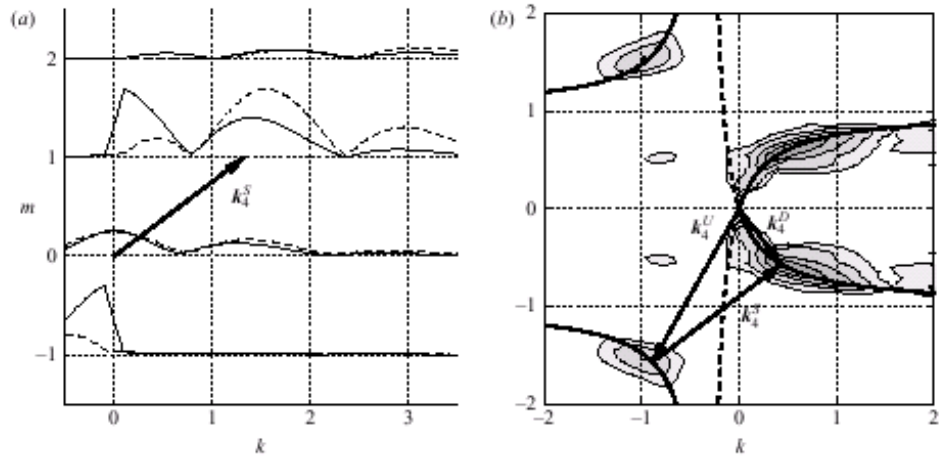

Fig. 26. Fourier decomposition of the steady u and w fields and identification of a resonant triad. The Fourier spectrum of the steady u (solid) and w (dashed) fields is used to identify the steady wavenumber vector in (a). The vector is added to the Fourier spectrum of the unstable mode to identify the resonant triad with the upward and downward propagating modes in (b).

B. Computational methods

Once steady solutions have been found, a linear stability analysis can be performed based on disturbances about the steady state. To be specific, the steady solutions are used to create the functional derivative $\mathbf{J_F(s)}$. The operator must use the solution vector $\mathbf{s} = \{\psi, \phi, v\}$ even in cases with constant background N and U where $\psi = \phi$ for the steady solution (see chapter IV section B6) since the stability analysis examines a disturbance to these variables which would render them unequal. It is also important to note here that while the relevant disturbance variable being solved is ψ, the equation being used to develop the $\mathbf{J_F(s)}$ operator is that for η. This means that the linear stability analysis will have to be formulated in terms of η, i.e., a disturbance $\mathbf{s}'$ is propagated forward in time according to

$$\mathbf{K}\frac{\partial \mathbf{s}'}{\partial t} + \mathbf{J_F(s)}\mathbf{s}' = 0, \tag{5.2}$$

where t represents time and where

$$\mathbf{K} = \begin{bmatrix} (q_z)^2 \frac{\partial^2}{\partial q^2} & 0 & 0 \\ 0 & I & 0 \\ 0 & 0 & I \end{bmatrix} \tag{5.3}$$

is an operator which transforms ψ to η. Assuming a normal mode solution in time of the form $\mathbf{s}' = \hat{\mathbf{s}}' \exp(\lambda t)$ allows (5.2) to be written as an equivalent generalized eigenvalue problem

$$\lambda \mathbf{K} \hat{\mathbf{s}}' + \mathbf{J_F}(\mathbf{s}) \hat{\mathbf{s}}' = 0 \tag{5.4}$$

which can be solved using a shifted-inverse power method as implemented in matlab. The method finds a specified number of eigenvalues closest to an input target value λ_T.

C. Results

1. Experimental design

Available memory applies major constraints on domain size with regards to direct eigenvalue solves, even moreso than for the steady solves presented in chapter IV. As such, the steady state results used for the instability calculations here were performed on the same domain size and with the same parameters as those in chapter IV (see section C1), but for a resolution of $\Delta x = \Delta q = \pi/16$. The change is justified by comparisons of eigenvalues and spatial structures of unstable modes versus time integrations at higher resolution (not shown) for a select number of cases.

As there may be more than one unstable mode present in the system, a search method must be used to find the largest growing mode. The present study searches by assuming a target eigenvalue with a growth rate larger than any likely to be seen

and varying the frequency within the expected range. This is done according to

$$\lambda_T = \lambda_r + i\lambda_i = 0.20 + i(0.15 + 0.05j)$$

where the subscripts r and i represent *real* and *imaginary*, respectively, and where $1 \leq j \leq 6$. An eigenvalue solve is then performed for each target value. The lower resolution steady solutions and growth rates of the most unstable mode are mapped for $0 < \epsilon < \epsilon_{cr}$ in increments of 0.02 and for $0 \leq \mathcal{R} \leq 1$ in increments of 0.05.

2. Verification

Figure 27 shows a comparison of the buoyancy field of the most unstable mode for hydrostatic nonrotating flow over a two-peak terrain profile with $\epsilon = 0.5$ as computed using methods in the current study versus that computed in [13]. The eigenvalue of the unstable mode is the same in each case, $0.060 + 0.320i$.

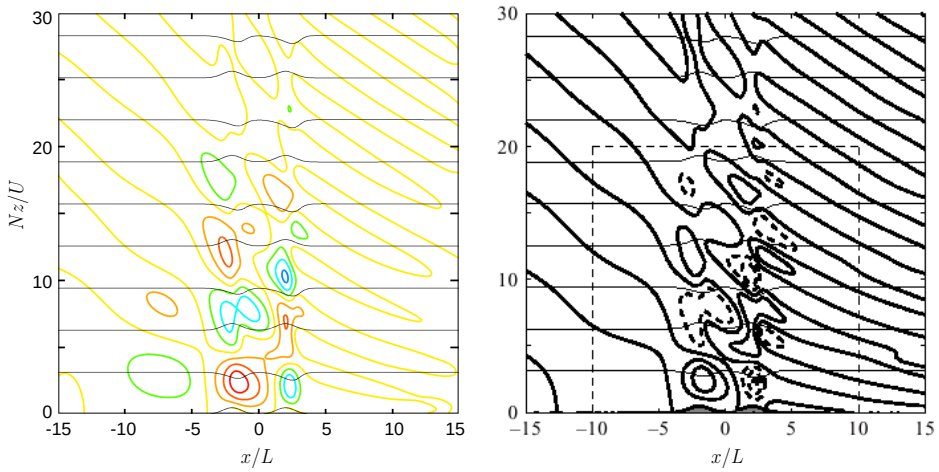

Fig. 27. Buoyancy field of the most unstable mode and isentropes of the steady-state solution for hydrostatic nonrotating ($\mathcal{R} = 0$) flow over a two-peak terrain profile with $\epsilon = 0.5$ using a direct eigenvalue solve coupled with the steady solution from: (a) the Newton solver and (b) Long's solution.

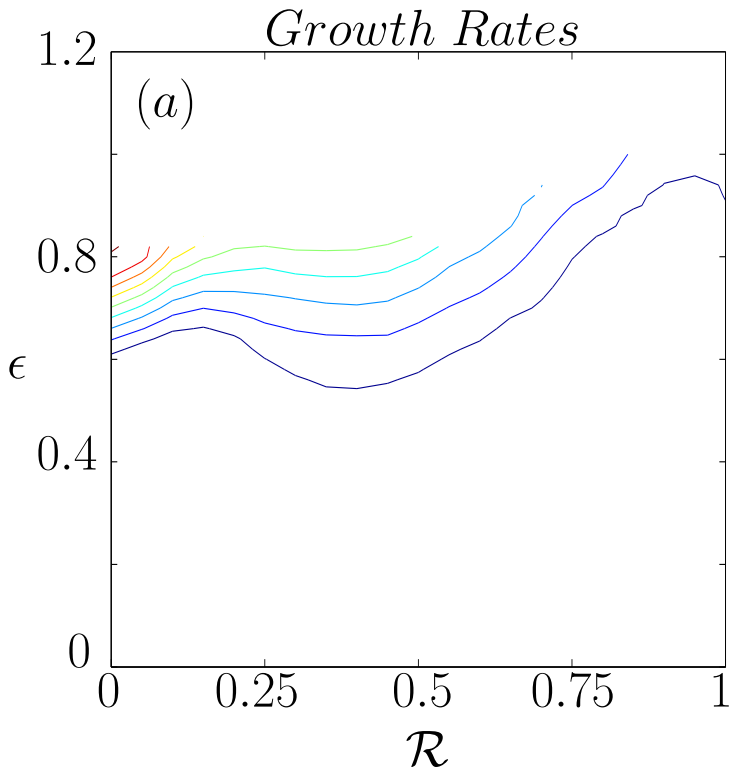

Fig. 28. Instability parameter space for flow over a single Gaussian peak. Growth rates are shown as a function of ϵ and $\mathcal{R}$ with a contour interval of 0.02. The lowest contour in ϵ has a value $\lambda_r = 0$. The upper bound of the contours in ϵ marks the steady overturning curve.

Figure 28 shows growth rates of the most unstable modes for flow over a single Gaussian ridge as functions of ϵ and $\mathcal{R}$. The upper boundary of the contours in ϵ marks the critical overturning curve as a function of $\mathcal{R}$. The lowest contour in ϵ marks the threshold instability value where $\lambda_r = 0$. The contour interval of the growth rates is 0.02. The growth rates increase with increasing values of ϵ and are strongest for the nonrotating case, with values reaching $\lambda_r = 0.164$ at $\epsilon = 0.82$. As $\mathcal{R}$ increases the range of unstable mountain heights begins to narrow and the growth rates decrease at a given value of ϵ. However, the trend reverses near $\mathcal{R} = 0.15$, and the growth rates

begin to increase. The widest range of unstable mountain heights is then found for $\mathcal{R} = 0.4$ with a threshold value at $\epsilon = 0.55$, well below the critical overturning value at $\epsilon_{cr} = 0.862$. Thereafter the growth rates and range of unstable mountain heights decreases with increasing $\mathcal{R}$. There is another increase at $\mathcal{R} = 1$ which may indicate a second branch of the instability for larger $\mathcal{R}$, but this remains to be explored.

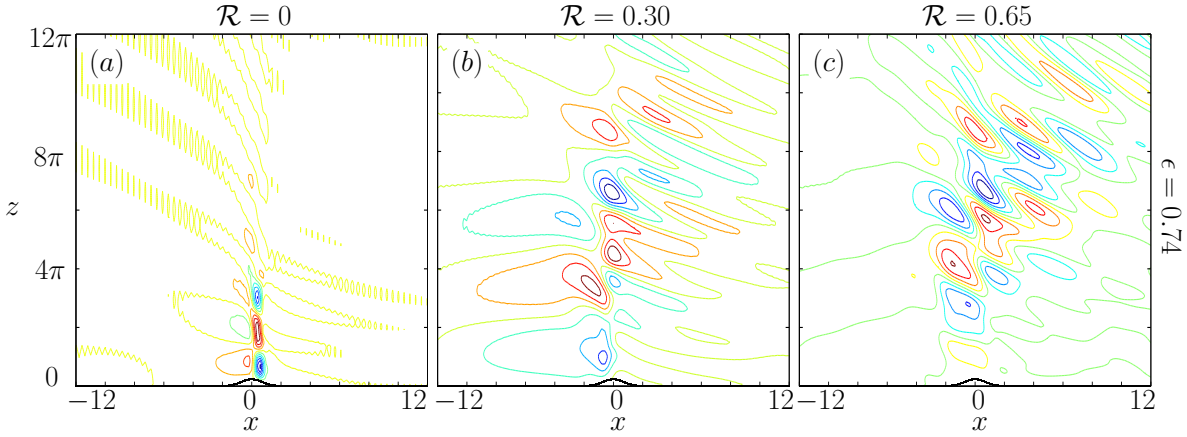

Fig. 29. Examples of instability spatial structure. The buoyancy field of the most unstable wave mode is shown for $\epsilon = 0.74$ while $\mathcal{R}$ is varied as $0, 0.3, 0.65$ in (a)–(c), respectively.

The buoyancy field of the most unstable mode is shown Figure 29 for $\epsilon = 0.74$ for varied values of $\mathcal{R}$. The nonrotating case in Figure 29a shows a cellular structure similar to that in Figure 24 as seen in [13] for two peaks. The instability mode is confined above the peak and decays rapidly with height. As the rotation is increased to $\mathcal{R} = 0.3$ the structure of the unstable mode changes dramatically as seen in Figure 29b and the growth rate has been cut from $\lambda_r = 0.119$ to $\lambda_r = 0.049$. The vertical scale of the unstable mode is greatly increased and the largest amplitude portion of the disturbance has ascended from the peak. The mode is also dispersive downstream, much like in the steady solutions. Figure 29c shows a weakly unstable case at $\mathcal{R} = 0.65$ with $\lambda_r = 0.014$. The dispersion downstream is once again increased

and ascent of the highest amplitude portion of the wave field continues.

D. Summary

Growth rates of a resonant wave-wave instability in flow over a single Gaussian peak are mapped through a parameter space spanned by the mountain height ϵ and the inverse Rossby number $\mathcal{R}$. The instability is strongest for nonrotating flow, but the widest range of unstable mountain heights is found at intermediate values of $\mathcal{R}$, with the instability threshold being well below the critical overturning height for steady mountain waves.

The spatial structure of the instability for nonrotating flow over a single peak is similar to that seen for flow over two peaks by [13] and implies the same mechanism. The addition of rotation to the system leads to much deeper wave modes which are dispersive and have a cellular structure which is elevated from the peak.

CHAPTER VI

SUMMARY

A. Time-splitting summary

The stability and accuracy of Klemp-Wilhelmson time-splitting schemes were examined in terms of their application to large-scale flows. Two splittings, those from Klemp and Wilhelmson [2, KW78] and Skamarock and Klemp [3, SK92], were investigated for the problems of Rossby- and Eady-wave propagation. A von Neumann eigenvalue analysis was carried out and the errors were quantified by comparing to the analytic solutions.

Results show that the original KW78 scheme is unable to maintain hydrostatic balance at large scales due to the split integration of the buoyancy and vertical pressure gradient terms. This introduces phase errors greater than 10% accross much of the relevant parameter space for both the Rossby and Eady modes. Additionally, there is an acoustic mode instability which arises through aliasing of the modes onto the large time step and coupling with buoyancy. The simultaneous integration of the buoyancy and pressure gradient terms on the small time step as in the modified scheme of SK92 addresses both these problems, allowing for stable and accurate integration of large-scale wave modes. More detailed results can be found in chapter II section C.

Fortunately, most newer mesoscale models already utilize the SK92 scheme for reasons separate from those presented in the current study. However, a few of the older KW78 models remain in relatively widespread use (at least for the moment). In general, the errors and instabilities discussed here highlight some of the issues that need to be considered when designing new time-split schemes. In particular, the

results caution against the splitting of balanced terms. For example, the splitting of the geostrophic balance in the simulation of highly balanced planetary atmospheres could potentially be problematic.

B. Newton solver and resonant instability summary

A Newton solver was developed in order to generalize Long's nonlinear solution for steady flow past 2D topography to the case of rotating flows with nonconstant background states. The solver is found to be robust throughout the parameter space and significantly faster than a time integration to steady state. The solver is also easily adapted to perform linear stability analyses about the steady-state wave solutions.

The steady solutions were mapped as a function of the nondimensional terrain height $\epsilon = Nh/U$ and inverse Rossby number $\mathcal{R} = fL/U$ for the case of constant N and U flow past an isolated peak. Surface drags were mapped throughout the parameter space and the critical ϵ for wave overturning was computed as a function of $\mathcal{R}$. Example calculations were presented to demonstrate the changes in the wave field with decreasing U for various values of $\epsilon/\mathcal{R}$. Further details of the steady solver results can be found in chapter IV section D.

Linear stability analysis of the steady solutions shows that the wave field for an isolated peak is unstable once ϵ becomes sufficiently large. The growth rate of the most unstable mode is largest for nonrotating flow, while the widest range of unstable ϵ occurs at intermediate values of $\mathcal{R}$. Further details of the resonant instability results can be found in chapter V section C.

In the present study only flow over a single peak was considered in order to reduce analysis to two parameters and to focus on the ϵ and $\mathcal{R}$ dependence. The resulting growth rates of the instability are relatively small when dimensionalized,

moreso with increasing $\mathcal{R}$ (since dimensional time scales as L/U). However, flow over more complex terrain was shown by [13] to lead to increased growth rates. The shorter dimensional time scale of nonhydrostatic flows would have a similar effect. As such, it seems most likely that any significant impacts of this instability in terms of wave steepening and breaking would occur for nonhydrostatic flow over complex terrain.

REFERENCES

[1] E. Kalnay, *Atmospheric Modeling, Data Assimilation and Predictability*, Cambridge, U.K.: Cambridge University Press, 2003.

[2] J. B. Klemp and R. B. Wilhelmson, "The simulation of three-dimensional convective storm dynamics," *J. Atmos. Sci.*, vol. 35, pp. 1070–1096, 1978.

[3] W. C. Skamarock and J. B. Klemp, "The stability of time-split numerical methods for the hydrostatic and the nonhydrostatic elastic equations," *Mon. Wea. Rev.*, vol. 120, pp. 2109–2127, 1992.

[4] G. I. Marchuk, *Numerical Methods in Weather Prediction*, New York: Academic Press, 1974.

[5] G. Strang, "On the construction and comparison of difference schemes," *SIAM J. Numer. Anal.*, vol. 5, pp. 506–517, 1968.

[6] J. Dudhia and F. Bresch, "A global version of the PSU-NCAR mesoscale model," *Mon. Wea. Rev.*, vol. 130, pp. 2989–3007, 2002.

[7] L.-R. Leung, Y. Qian, and X. Bian, "Hydroclimate of the western United States based on observations and regional climate simulation of 1981–2000. Part I: Seasonal statistics," *J. Climate*, vol. 16, pp. 1892–1911, 2003.

[8] P. B. Duffy, R. W. Arritt, J. Coquard, W. Gutowski, J. Han, J. Iorio, J. Kim, L.-R. Leung, J. Roads, and E. Zeledon, "Simulations of present and future climates in the western United States with four nested regional climate models," *J. Climate*, vol. 19, pp. 873–895, 2006.

[9] R. R. Long, "Some aspects of the flow of stratified fluids," *Tellus*, vol. 5, pp. 42–58, 1953.

[10] O. M. Phillips, "On the dynamics of unsteady gravity waves of finite amplitude," *J. Fluid Mech.*, vol. 9, pp. 193–217, 1960.

[11] T. B. Benjamin and J. E. Feir, "The disintegration of wave trains on deep water," *J. Fluid Mech.*, pp. 417–430, 1967.

[12] K. Hasselmann, "A criterion for nonlinear wave stability," *J. Fluid Mech.*, vol. 30, pp. 737–739, 1967.

[13] Y. Lee, D. J. Muraki, and D. E. Alexander, "A resonant instability of steady mountain waves," *J. Fluid Mech.*, vol. 568, pp. 303–327, 2006.

[14] K. C. Viner and C. C. Epifanio, "An analysis of Klemp-Wilhelmson schemes as applied to large-scale wave modes," *Mon. Wea. Rev.*, vol. 136, pp. 4730–4745, 2008.

[15] D. R. Durran, *Numerical Methods for Wave Equations in Geophysical Fluid Dynamics*, New York: Springer-Verlag, 1999.

[16] J. Dudhia, "A nonhydrostatic version of the Penn State–NCAR mesoscale model: Validation tests and simulation of an Atlantic cyclone and cold front," *Mon. Wea. Rev.*, vol. 121, pp. 1493–1513, 1993.

[17] R. A. Pielke, W. R. Cotton, R. L. Walko, C. J. Tremback, W. A. Lyons, L. D. Grasso, M. E. Nicholls, M. D. Moran, D. A. Wesley, T. J. Lee, and J. H. Copeland, "A comprehensive meteorological modeling system – RAMS," *Meteorol. Atmos. Phy.*, vol. 49, pp. 69–91, 1992.

[18] J. B. Klemp, W. C. Skamarock, and J. Dudhia, "Conservative split-explicit time integration methods for the compressible nonhydrostatic equations," *Mon. Wea. Rev.*, vol. 135, pp. 2897–2913, 2007.

[19] M. Xue, K. K. Droegemeier, and V. Wong, "The Advanced Regional Prediction System (ARPS) – A multi-scale nonhydrostatic atmospheric simulation and prediction model. Part I: Model dynamics and verification," *Meteorol. Atmos. Phy.*, vol. 75, pp. 161–193, 2000.

[20] L. J. Wicker and W. C. Skamarock, "Time-splitting methods for elastic models using forward time schemes," *Mon. Wea. Rev.*, vol. 130, pp. 2088–2097, 2002.

[21] D. R. Durran and J. B. Klemp, "A compressible model for the simulation of moist mountain waves," *Mon. Wea. Rev.*, vol. 111, pp. 2341–2361, 1983.

[22] L. J. Wicker and W. C. Skamarock, "A time-splitting scheme for the elastic equations incorporating second-order Runge-Kutta time differencing," *Mon. Wea. Rev.*, vol. 126, pp. 1992–1999, 1998.

[23] J. R. Holton, *An Introduction to Dynamic Meteorology*, Burlington, MA: Elsevier Academic Press, 4^{th} ed., 2004.

[24] D. R. Durran, "On a physical mechanism for Rossby wave propagation," *J. Atmos. Sci.*, vol. 45, pp. 4020–4022, 1988.

[25] A. E. Gill, *Atmosphere-Ocean Dynamics*, San Diego, CA: Academic Press, 1982.

[26] C.-C. Chen, D. R. Durran, and G. J. Hakim, "Mountain-wave momentum flux in an evolving synoptic-scale flow," *J. Atmos. Sci.*, vol. 62, pp. 3213–3231, 2005.

[27] C. C. Epifanio and R. Rotunno, "The dynamics of orographic wake formation in flows with upstream blocking," *J. Atmos. Sci.*, vol. 62, pp. 3127–3150, 2005.

[28] P. Queney, "The problem of air flow over mountains: A summary of theoretical results," *Bull. AMS*, vol. 29, pp. 16–26, 1948.

[29] R. S. Scorer, "Theory of waves in the lee of mountains," *Quart. J. Roy. Meteor. Soc.*, vol. 75, pp. 41–56, 1949.

[30] S.T. Garner, "Blocking and frontogenesis by two-dimensional terrain in baroclinic flow. Part I: numerical experiments," *J. Atmos. Sci.*, vol. 56, pp. 1495–1508, 1999.

[31] R. T. Pierrehumbert, "Linear results on the barrier effects of mesoscale mountains," *J. Atmos. Sci.*, vol. 41, pp. 1356–1367, 1984.

[32] R. R. Long, "Some aspects of the flow of stratified fluids: III. Continuous density gradients.," *Tellus*, vol. 7, pp. 341–357, 1955.

[33] R. B. Smith, "The steepening of hydrostatic mountain waves," *J. Atmos. Sci.*, vol. 34, pp. 1634–1654, 1977.

[34] P. G. Baines, *Topographic Effects in Stratified Flows*, Cambridge, U.K.: Cambridge University Press, 1995.

[35] D. R. Durran and J. B. Klemp, "Another look at downslope winds. Part II: Nonlinear amplification beneath wave-overturning layers," *J. Atmos. Sci.*, vol. 44, pp. 3402–3412, 1987.

[36] R. B. Smith, "On severe downslope winds," *J. Atmos. Sci.*, vol. 42, pp. 2597–2603, 1985.

[37] R. B. Smith and S. Grønås, "Stagnation points and bifurcation in 3-D mountain airflow," *Tellus*, vol. 45A, pp. 28–43, 1993.

[38] R. B. Smith, "Hydrostatic airflow over mountains," *Advances in Geophysics*, vol. 31, pp. 1–41, 1989.

[39] C. Schär and D. R. Durran, "Vortex formation and vortex shedding in continously stratified flows past isolated topography," *J. Atmos. Sci.*, vol. 54, pp. 534–554, 1997.

[40] C. C. Epifanio and T. Qian, "Wave-turbulence interactions in a breaking mountain wave," *J. Atmos. Sci.*, vol. 65, pp. 3139–3158, 2008.

[41] J. R. Holton, "The role of gravity wave induced drag and diffusion in the momentum budget of the mesosphere," *J. Atmos. Sci.*, vol. 39, pp. 791–799, 1982.

[42] D. K. Lilly and E. J. Zipser, "The Front Range windstorm of 11 January 1972: A meteorological narrative," *Weatherwise*, vol. 25, pp. 56–63, 1972.

[43] D. K. Lilly, "A severe downslope windstorm and aircraft turbulence event induced by a mountain wave," *J. Atmos. Sci.*, vol. 35, pp. 59–77, 1978.

[44] Q. Jiang and J. D. Doyle, "Gravity wave breaking over the central Alps: role of complex terrain," *J. Atmos. Sci.*, vol. 61, pp. 2249–2266, 2004.

[45] J. D. Doyle, M. A. Shapiro, Q. Jiang, and D. L. Bartels, "Large-amplitude mountain wave breaking over Greenland," *J. Atmos. Sci.*, vol. 62, pp. 3106–3126, 2005.

[46] R. T. Pierrehumbert and B. Wyman, "Upstream effects of mesoscale mountains," *J. Atmos. Sci.*, vol. 42, pp. 977–1003, 1985.

[47] J. Trüb and H. C. Davies, "Flow over a mesoscale ridge: pathways to regime transition," *Tellus*, vol. 47A, pp. 502–524, 1995.

[48] S.A. Braun, R. Rotunno, and J.B. Klemp, "Effects of coastal orography on landfalling cold fronts. part I: dry, inviscid dynamics," *J. Atmos. Sci.*, vol. 56, pp. 517–533, 1998.

[49] S.A. Braun, R. Rotunno, and J.B. Klemp, "Effects of coastal orography on landfalling cold fronts. part II: effects of surface friction," *J. Atmos. Sci.*, vol. 56, pp. 3366–3384, 1998.

[50] S.T. Garner, "Blocking and frontogenesis by two-dimensional terrain in baroclinic flow. Part II: analysis of flow stagnation mechanisms," *J. Atmos. Sci.*, vol. 56, pp. 1509–1523, 1999.

[51] O. M. Phillips, "The interaction trapping of internal gravity waves," *J. Fluid Mech.*, vol. 34, pp. 407–416, 1968.

[52] O. M. Phillips, "Wave interactions – the evolution of an idea," *J. Fluid Mech.*, vol. 106, pp. 215–227, 1981.

[53] C. Staquet and J. Sommeria, "Internal gravity waves: from instabilities to turbulence," *Annu. Rev. Fluid Mech.*, vol. 34, pp. 559–593, 2002.

[54] P. G. Drazin and W. H. Reid, *Hydrodynamic Stability*, Cambridge, U.K.: Cambridge University Press, 2nd ed., 2004.

[55] J. B. Klemp and D. K. Lilly, "Numerical simulation of hydrostatic mountain waves," *J. Atmos. Sci.*, vol. 35, pp. 78–107, 1978.

[56] T. Gal-Chen and R. Somerville, "On the use of a coordinate transformation for the solution of the Navier-Stokes equations," *J. Comput. Phys.*, vol. 17, pp. 209–228, 1975.

[57] L. Armijo, "Minimization of functions having Lipschitz-continuous first partial derivatives," *Pacific Journal of Mathematics*, vol. 16, pp. 1–3, 1966.

[58] C. C. Epifanio and D. R. Durran, "Three-dimensional effects in high-drag-state flows over long ridges," *J. Atmos. Sci.*, vol. 58, pp. 1051–1065, 2001.

[59] J. B. Klemp and D. R. Durran, "An upper boundary condition permitting internal gravity wave radiation in numerical mesoscale models," *Mon. Wea. Rev.*, vol. 111, pp. 430–444, 1983.

VITA

My name is Kevin Carl Viner. I received my B.S. and M.S. in atmospheric sciences from Purdue University in 2002 and 2004, respectively. I received my Ph.D. in atmospheric sciences from Texas A&M University in December 2009. I can be reached through the Department of Atmospheric Sciences at the following address: 1204 Eller O&M, College Station, TX 77840. My email address is kcvphd@gmail.com.

The typist for this thesis was Kevin Carl Viner.